学位論文

Study on turbulent magnetic reconnection by Reynolds-averaged MHD model and kinetic viewpoint

(レイノルズ平均 MHD モデルと運動論的視点による乱流磁気リコネクション研究)

平成 26 年 12 月 博士 (理学) 申請

東京大学大学院 理学系研究科
地球惑星科学専攻

東森 一晃

SUPERVISOR MASAHIRO HOSHINO[1]
COLLABORATORS MASAHIRO HOSHINO[1] AND NOBUMITSU YOKOI[2]

[1]Department of Earth and Planetary Science, University of Tokyo
[2]Institute of Industrial Science, University of Tokyo

Thesis advisor: Masahiro Hoshino Author: Katsuaki Higashimori

Study on turbulent magnetic reconnection by Reynolds-averaged MHD model and kinetic viewpoint

ABSTRACT

For many active phenomena in space plasmas, such as the substorm in the Earth's magnetosphere, the solar flare, and the dynamics in pulsar magnetosphere, it has been suggested that "*magnetic reconnection*" often plays an important role in their energy release. In general consensus of magnetic reconnection, the topological change of magnetic field lines leads to the release of magnetic field energy and results in the dynamical plasma processes. From previous theoretical and observational studies, it is suggested that the mechanism of magnetic reconnection may not be understood by only a single solution and highly depends on the scale and the plasma behavior on which we are focusing. For this reason, the dynamics has been studied by both the collisionless kinetic and the magneto-hydro-dynamic (MHD) approaches, so far. In either cases, reconnection dynamics has been mainly studied in a laminar equilibrium, and the efficient mechanism to convert the magnetic field energy into kinetic and internal energy of plasmas has been suggested. On the other hand, the effect of turbulence, which seems to be natural and essential in high magnetic Reynolds number plasmas, has not been established yet. This dissertation aims to address some suggestions on the relationship between turbulence and reconnection dynamics from collisionless kinetic and MHD reconnections with different viewpoints.

As for the collisionless kinetic reconnection, we consider the reconnection as the source of turbulence. In the kinetic scale, there exists plenty of free energies, such as non-uniformity and the pressure anisotropy, and we may expect a lot of plasma instabilities compared to the MHD system. Along with such a way of thinking, Chapter 2–3 focused on the self-generated fluctuations in magnetic reconnection. In Chapter 2, we considered the condition when magnetic reconnection becomes turbulent based on the nonlinear kinetic simulations and the local linear analysis. The results showed that whether the reconnection exhausts become turbulent or not strongly depends on the ion plasma beta in the initial inflow regions, β_{i0}: the reconnection jet becomes turbulent in the low beta condition, $\beta_{i0} < 0.1$–0.2. On this issue, the excitation and suppression of Alfvénic modes in the plasma sheet boundary layer (PSBL) is discussed. The local analysis for the PSBL suggests that as the ion beta increases, the damping rate of ion-scale Alfvén waves becomes larger and suppresses the ion-scale fluctuations. In addition to the PSBL dynamics, we tried to explain global unstable mode observed in reconnection jets. This unstable mode appears across the current sheet and cannot be explained by only the PSBL dynamics shown in Chapter 2. Then, in Chapter 3, in order to discuss the nature of the global mode in jets, we presented a linear eigenmode analysis including both non-uniformity and pressure anisotropy effects. The analysis suggests that the global mode observed in the reconnection jet is the slow Alfvén type mode, where the globally-appearing magnetic pressure gradient force weakens the magnetic tension force, and is very sensitive to the pressure anisotropy. As a result, the mode has efficient growth rate and could con-

tribute to the generation of fluctuations in the anisotropic ion-scale reconnection jet.

In Chapter 4, the macroscopic MHD reconnection dynamics is focused. We considered the effect of pre-existing turbulence in the MHD scale current sheet, and how turbulence affects the current sheet dynamics is investigated using a Reynolds-averaged MHD model. In the model, equations of time evolution for turbulent quantities (such as cross-helicity and turbulent energy) are solved in addition to the mean MHD equations, and the coarse-grained effect was considered. Namely, the effect is included in Ohm's law as a turbulent electromotive force term, and mean and fluctuating field quantities develop with interacting each other through it. The results suggest that the initial current sheet develops in three ways, depending on the strength of turbulence: slow laminar reconnection, turbulent reconnection, and turbulent diffusion without magnetic reconnection. In the second turbulent-mediated reconnection case, the turbulent energy and cross-helicity develop near the magnetic neutral point through the interaction between mean and the fluctuating field, and the localized turbulent diffusion leads the fast magnetic reconnection. Because turbulence takes the central role in magnetic field diffusion instead of the kinetic-originated resistivity, the current sheet may not necessarily be as thin as the kinetic scale.

Contents

List of Tables

List of Figures

ACKNOWLEDGMENTS

I am deeply grateful to Hoshino sensei. I learned a lot of things and ways of thinking from him. I would like to give a special thanks to Yokoi sensei, too. He not only led me with enthusiasm but also encouraged me when I met an obstacle. I am really grateful to professor Masaki Fujimoto, associated professor Takaaki Yokoyama, professor Ryoji Matsumoto, professor Fujihiro Hamba, associated professor Yoshifumi Saito for many valuable and useful comments to improve this dissertation. I also owe an important debt to assistant professor Takanobu Amano, assistant professor Hiroshi Hasegawa, Izutsu-san, Yoshitake-san, Hirai-san, Shirasawa-san, Saito-san, and Hirabayashi-san for useful discussions. Finally, I would like to express my greatest gratitude to my family for their warmest encouragement.

CHAPTER 1
General Introduction

This study focuses on the relationship between turbulence and magnetic reconnection. Because magnetic reconnection is a multiscale phenomenon ranging from magneto-hydro-dynamic (MHD) to electron-scale, both microscopic and macroscopic viewpoints would be needed, depending on the situation or the scale on which we focus. We focused on magnetic reconnection in high magnetic Reynolds number plasmas, where non-linearity becomes important. In particular, magnetic reconnection in two different scales (MHD and ion-scales) are considered, and for each cases the relation to turbulence is discussed. This Chapter briefly introduces basic signatures and problems in macro and micro-scale magnetic reconnection. Then, we refer to two different viewpoints on the relationship between turbulence and magnetic reconnection presented in this dissertation.

§ 1.1 An introduction to magnetic reconnection and the relation to turbulence

In geophysical, astrophysical, and experimental phenomena, we often encounter the situations where topological change and rapid diffusion of magnetic field are indispensable to account for them. The important idea, which could satisfy the above requirements, are known to be "*magnetic reconnection*". Basically, magnetic reconnection changes the topology of magnetic field and rapidly converts energy of magnetic field into that of plasmas, when the anti-parallel magnetic fields are closely lying with each other. The concept of magnetic reconnection originates from 1940s [31], and the importance has been widely-recognized to explain many active phenomena such as the solar flare [70] and magnetospheric dynamics [21], where the explosive energy release is indispensable to account for them. The reconnection dynamics strongly depends on the scale and the plasma condition such as the magnetic Reynolds number, R_m. Then, magnetic reconnection has been observed in both magneto-hydro-dynamic (MHD) and small kinetic scales by both remote and in-situ observations, suggesting multi-scale phenomena. So far, many studies have discussed the role of magnetic reconnection in various phenomena, and they are recently classified according to the characteristic spatial scale of magnetic reconnection and the magnetic Reynolds number [48]. Fig. 1.1 shows various phenomena where magnetic reconnection is considered to play the key role, and they are classified depending on the characteristic spatial scale of reconnection and the magnetic Reynolds number. This diagram is adapted from [48] and drawn by using the data listed in Table I of their paper. The horizontal axis is the ratio of the reconnection size, L_R, to the ion inertial length, $\lambda_i = \omega_{pi}/c$ (where ω_{pi} is the ion plasma frequency), and the vertical axis is the magnetic Reynolds number. For example, the system approaches the MHD approximation in large L_R/λ_i, while it should be discussed by the kinetic treatment in small L_R/λ_i. On the other hand, as R_m increases, the non-linear nature becomes very important. In this way, the viewpoint and the approach to under-

stand reconnection dynamics would differ, depending on the scale or the situation on which we are now focusing.

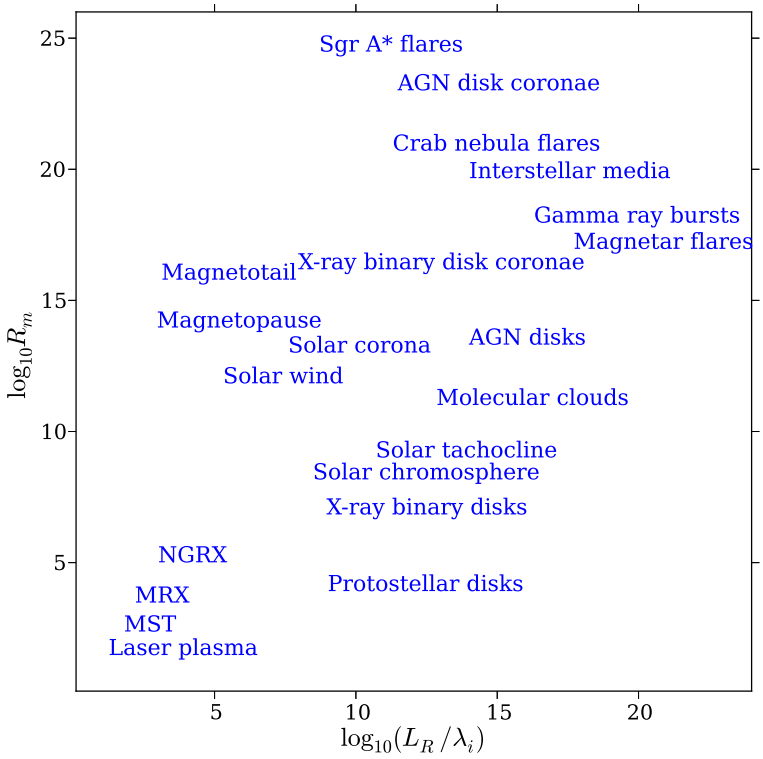

Figure 1.1: Various phenomena where magnetic reconnection are considered to take place are shown in $\log_{10}(R_m)$–$\log_{10}(L_R/\lambda_i)$ space (the data were adapted from Table I in [48]).

The present study focuses on magnetic reconnection in high R_m situations, which is expected in many astrophysical phenomena. For the dynamics in high R_m plasmas, the system is generally expected to develop into turbulence through non-linear couplings, and understanding the relation to turbulence would be an important issue. In particular, we consider the relationship from both the macro-scale (MHD) and micro-scale (kinetic) viewpoints separately, and aim to address new insights to the turbulent magnetic reconnection study. In what follows, ba-

sic issues (problems) on MHD and kinetic scale reconnections are introduced, respectively. Then, how turbulence plays a part in each of them is considered.

Macroscale magnetic reconnection

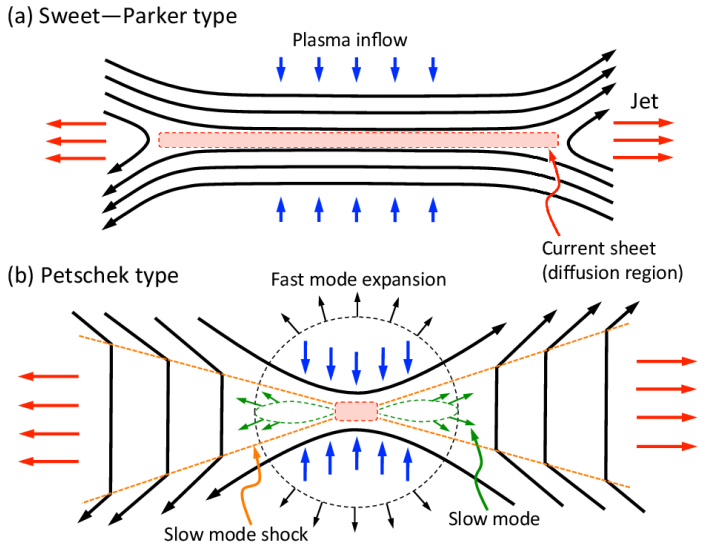

Figure 1.2: Schematic views of (a) Sweet–Parker and (b) Petschek reconnection models.

First, let us begin with an MHD scale current sheet without pre-existing turbulence. Imagine the current sheet, whose width is much larger than the ion inertial length. For the laminar MHD approximation, the basic reconnection nature was first modeled by Sweet and Parker [87, 71]. The schematic view is shown in Fig. 1.2(a). The model assumes a finite collisional resistivity everywhere in the current sheet between the anti-parallel magnetic field. The Ohmic diffusion slowly converts magnetic field energy to the thermal energy of plasmas everywhere in the elongated current sheet and, at the same time, leads the topological change of the magnetic field. Then, the thermal pressure gradient force and the Lorentz force by the reconnected magnetic field accelerate plasmas. This energy conversion rate

(usually called as "*reconnection rate*") is shown to be proportional to $R_m^{-1/2}$ (R_m is the magnetic Reynolds number) by considering a simple law of conservation of mass. Since the magnetic Reynolds number is extremely high in space plasmas ($R_m \sim 10^{12}$ in solar corona), the Sweet-Parker reconnection rate is known to be much smaller than that of observations [103]. Subsequently, Petschek solved this problem by introducing slow-mode shocks [72] (see Fig.1.2(b)). This model assumed a localized diffusion region near the reconnection point, and it was suggested that two pairs of slow-mode shocks attached to the diffusion region accelerate plasmas. The reconnection rate can be expressed as a function of $\propto 1/\ln R_m$ and explains the realistic energy conversion rate well, even in a high magnetic Reynolds number plasma. This model has been also realized by nonlinear MHD simulations [91, 77]. If the localized resistivity (often called as "*anomalous resistivity*") is assumed in the current sheet, the magnetic field energy is locally changed into the internal energy of plasmas and the magneto-sonic waves expand from the diffusion region. Since the phase speed of slow magneto-sonic waves oblique to the ambient magnetic field is much smaller than that of fast magneto-sonic waves, the inflowing speed becomes super-sonic only to slow-mode waves and slow-mode shocks form outside the diffusion region. Also, the existence of slow-mode shocks has been observed by in-situ observations [76]. In this way, the Petschek model has been one of major candidates for the fast reconnection in high R_m plasmas, and seems to resolve both theoretical and observational requirements, however, it masked the important physics: where does the localized resistivity (diffusion region) come from?

Without turbulence, it has been considered that the origin of anomalous resistivity is due to the smallest electron scale physics. In the electron scale, in addition to the collisional resistivity, other physical resistivity may be allowed in the generalized Ohm's law:

$$\boldsymbol{E} = \underbrace{\eta_{\text{collision}}\boldsymbol{J}}_{\text{MHD resistive}} \underbrace{+\frac{m_\text{e}}{e}\frac{d\boldsymbol{V}_\text{e}}{dt} - \frac{1}{en_\text{e}}\boldsymbol{\nabla}\cdot\overleftrightarrow{\boldsymbol{P}_\text{e}}}_{\text{kinetic scale, resistive}} \underbrace{-\boldsymbol{V}_\text{e}\times\boldsymbol{B}}_{\text{non-resistive}}, \tag{1.1}$$

where $\boldsymbol{V}_e$ is the electron bulk velocity, $d/dt = \partial/\partial t + \boldsymbol{V}_\mathrm{e} \cdot \boldsymbol{\nabla}$, and $\overleftrightarrow{\boldsymbol{P}}_\mathrm{e}$ is the electron pressure tensor arising from the non-gyro motion of electrons near the magnetic neutral point ($B \sim 0$). In collisionless system, the second electron inertial resistivity and the third electron non-diagonal pressure term dominate, when the thickness of the current sheet approaches ion to electron inertial length [94, 39]. However, in the MHD scale current sheet, such kinetic resistivity is absent, because the current sheet is much thicker than the ion inertial length and the electron inertial length. Also, in a high magnetic Reynolds number region, the collisional resistivity is ignorable and there seems to be no resistivity in the MHD current sheet to trigger the fast magnetic reconnection. In this way, the Petcheck model has an ambiguous point that should be clarified, even though it has been still considered to be an important candidate for the fast reconnection in high R_m plasmas.

Recently, one of important possibilities resolving the above issue, the idea so called as "plasmoid instability" attracts much attention [82, 60, 93]. Generally by the collisional resistivity, magnetic reconnection develops into relatively slow Sweet-Parker type in low magnetic Reynolds number, $R_m < \mathcal{O}(10^3)$. However as R_m increases, the secondary (thirdly, fourth, ...) tearing instability takes place in the elongated Sweet-Parker current sheet and reconnection becomes even faster. The threshold from Sweet-Parker to the plasmoid instability is suggested to be $R_m \sim \mathcal{O}(10^4)$, and beyond the reconnection rate ceases to depend on the magnetic Reynolds number [5]. This would be one of important ideas for the fast magnetic reconnection without assuming any resistive model in the MHD scale.

In this study, we consider an alternative way, turbulence, to account for the efficient energy conversion rate in macroscale magnetic reconnection. The above plasmoid instability assumes an elongated initial current sheet with low level fluctuations so as not to disturb the growth of the tearing mode instability [26]. Certainly such a situation would be possible, but it may be just a fraction of possible situations in high R_m plasmas, where many non-linear effects could participate in the dynamics. Then, let us begin with the assumption that turbulence

is pre-existing in the background of the initial current sheet. It seems to be more natural way of thinking for us to assume pre-existing turbulence in thick MHD scale current sheet in a high magnetic Reynolds number space, because the scale gap between injection and dissipation scales is enough large for waves to interact with each other without strong dissipation. For example, many in-situ observations suggest that the region where reconnection takes place is often in the turbulent state (such as solar wind [64, 75], magnetopause [35], magnetotail [45], etc.). Such a role of turbulence was first discussed by [65]. They simulated a current sheet with weak background fluctuations under the incompressible MHD approximation, and it was reported that small scale fluctuations developed in the reconnection point and enhanced viscous and resistive dissipation. Another study theoretically suggested that, in the strong Alfvénic turbulence, the reconnection rate does not depend on electric resistivity but rather on the property of turbulence (such as the characteristic scale length and power of the fluctuation) [54]. That scenario has been examined in MHD simulations, where external turbulence is continuously forced in a current sheet [51]. The effect of turbulence on the macroscopic reconnection rate has also been investigated in large-scale (high magnetic Reynolds number) two-dimensional simulations. By such high magnetic Reynolds number simulations, we see that there exist a critical Reynolds number and turbulent power above which turbulence greatly affects reconnection, and the reconnection rate has weaker dependence on electric resistivity than does Sweet-Parker reconnection [61]. Recently, another viewpoint on the relationship between turbulence and reconnection has been presented according to the theory of MHD turbulence [101]. In that study, it is suggested that the generation of cross-helicity $\mathcal{W} \equiv \langle \boldsymbol{v}' \cdot \boldsymbol{b}' \rangle$ (where $\boldsymbol{v}'$ and $\boldsymbol{b}'$ are respectively the characteristic velocity and magnetic field of turbulent motion, and the brackets represent ensemble average) would enhance the rate of reconnection. In the current understanding, there is no consensus about what turbulent mechanism accelerate macro-scale reconnection in high R_m plasmas. Also, the previous numerical studies continuously force turbulence throughout the simulations, and it is difficult to evaluate the recon-

nection rate. At least, to understand where turbulent energy comes from, how it is sustained in reconnection system, and what turbulent mechanism enhance the reconnection rate is important in the present macro-scale turbulent reconnection study.

Microscale magnetic reconnection

Another interest of this study is microscale reconnection dynamics. Imagine a current sheet whose thickness is about an ion inertial length and the scale gap is $L_R/\lambda_i \sim 10^2$. Because the electron diffusion region is shown to be seamlessly connected to ion scale by previous kinetic simulations [20, 58] (at the minimum, two-dimensional anti-parallel magnetic field configuration discussed in the present study), this study focus on a relatively large ion scale beyond electron scale. [1] First of all, let us introduce the basic understanding of ion-scale collisionless magnetic reconnection. In the ion-scale, there are several effects in addition to MHD dynamics:

a) Hall effects,

b) Electron pressure effects,

c) Ion kinetic effects.

First two effects can be simply understood by the two-fluid model. By the fluid equation of motion of electrons and the charge neutral condition $en_e = q_i n_i$,

[1] As for the electron diffusion region physics, for example, see [38]. In addition to inertial and non-diagonal electron pressure resistivity, importance of small scale turbulence for the diffusion process is recently a hot topic. (For example, in the strong guide-field reconnection, it is shown that electron scale turbulence is enhanced in the electron diffusion region, and not only electron inertia and non-diagonal pressure effects but also turbulent transport could facilitate magnetic field annihilation [19, 12]. In the case of anti-parallel field reconnection, it is suggested that the electromagnetic turbulence is intermittently enhanced and the turbulent transport also facilitates anomalous resistivity [25]. Another study suggest that the saturation level of the lower hybrid mode around the current sheet becomes larger by the coupling with the Kelvin-Helmholtz instability, and it could enable further magnetic field dissipation [84].)

one obtains the following generalized Ohm's law:

$$\boldsymbol{E} = \eta_{\text{collision}}\boldsymbol{J} - \frac{\boldsymbol{V}_i \times \boldsymbol{B}}{c} + \frac{1}{4\pi e n_e}\boldsymbol{J} \times \boldsymbol{B} - \frac{1}{e n_e}\boldsymbol{\nabla} \cdot \overleftrightarrow{\boldsymbol{P}}_{\text{e}} - \frac{m_e}{e}\frac{d\boldsymbol{V}_e}{dt}. \tag{1.2}$$

Normalizing this equation using Alfvén velocity $V_A \equiv B_0/\sqrt{4\pi m_i n_i}$, characteristic spatial scale L, and time scale $T = L/V_A$ gives

$$\begin{aligned}\hat{\boldsymbol{E}} = &\underbrace{\hat{\eta}_{\text{collision}}\hat{\boldsymbol{J}} - \hat{\boldsymbol{V}}_i \times \hat{\boldsymbol{B}}}_{\text{MHD scale}} \\ &\underbrace{+\left(\frac{\lambda_i}{L}\right)\hat{\boldsymbol{J}} \times \hat{\boldsymbol{B}} - \left(\frac{\lambda_i}{L}\right)\hat{\boldsymbol{\nabla}} \cdot \overleftrightarrow{\hat{\boldsymbol{P}}}_{\text{e}}}_{\text{ion scale}} \underbrace{- \left(\frac{\lambda_e}{L}\right)\left(\frac{m_e}{m_i}\right)^{1/2}\frac{d\hat{\boldsymbol{V}}_e}{d\hat{t}}}_{\text{electron scale}},\end{aligned} \tag{1.3}$$

where λ_i and λ_e are respectively ion and electron inertial lengths. (The hat $\hat{}$ stands for normalized quantities, e.g., $\hat{\boldsymbol{E}} = c\boldsymbol{E}/(B_* V_{A*})$, where B_* and V_{A*} is magnetic field and Alfvén velocity used for the normalization.) When the characteristic spatial scale length gets close to the ion inertial length, the third Hall term and the fourth electron pressure term of Rhs of Eq.(1.3) contribute to the dynamics. In the reconnection literature, the importance of Hall effects are often discussed in terms of fast reconnection. For example, enhancement of the linear growth rate [89] and the non-linear reconnection rate [80] by the Hall effect is suggested. Also the comparison of reconnection rates among MHD, Hall-MHD, hybrid (where ions are treated as particles and electrons as a fluid), and full-particle simulations suggests that reconnection rate may be controlled by Hall physics [7]. [2] As for the electron pressure effect is often discussed in terms of diffusion region physics as mentioned above [94, 39].

The third ion kinetic effects c) cannot be explained simply by the above Ohm's law Eq.(1.3), but play an important role in ion-scale reconnection outflow jets. To

[2] Certainly many works addressed the importance of Hall effects on the reconnection rate, but it is still under discussion whether only Hall effects control reconnection. It is because, for example, pair-plasma simulations, where the Hall term is absent, usually show efficient reconnection rate, too [4, 88].

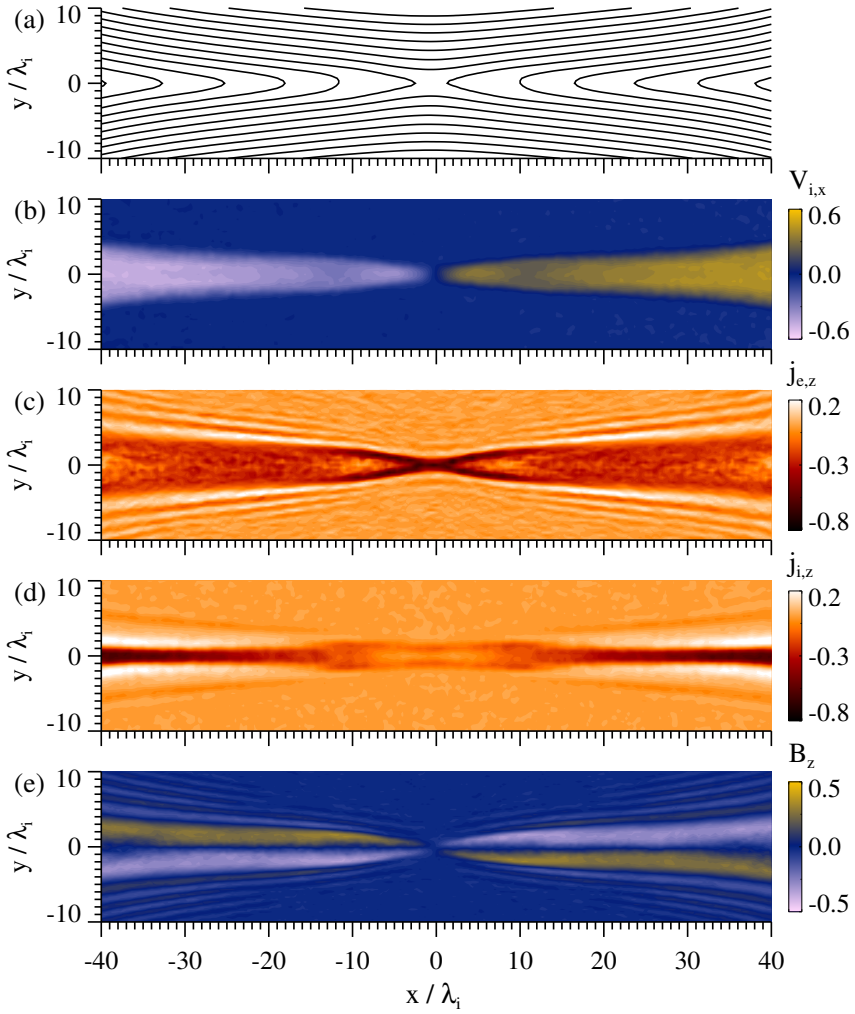

Figure 1.3: From the top to the bottom (a) magnetic field lines, (b) ion bulk velocity $V_{i,x}$, (c) electron current density $j_{e,z}$, (d) ion current density $j_{i,z}$, and (e) out of plane (Hall) magnetic field B_z are shown. The spatial scale is normalized by the ion inertial length.

explain this, Fig.1.3 shows reconnection exhausts obtained by the hybrid simulation. (Note that preceding studies have already shown these basic structures [59, 81]. See also Chapter 2) From top to bottom, (a) magnetic field lines, (b) x-component of ion bulk velocity, (c) out-of-plane electron current, (d) out-of-plane ion current, and (e) the out-of-plane (Hall) magnetic field are shown. Magnetic field lines reconnect with each other at $(x, y) = (0, 0)$, and reconnection exhausts with wide flare-angle are observed. Also in Fig.1.3(e), quadrupole out of plane Hall magnetic field forms. Such signatures (opened jets and hall fields) can be observed in Hall-MHD simulations [63]. One of notable differences between Hall-MHD (MHD) and particle simulations is the current profile in reconnection outflows. In the case of Hall-MHD reconnection, a bifurcated current structure forms in opened reconnection exhausts as MHD simulations. On the other hand, if ion kinetic effects are taken into account, a single current sheet, whose width is about ion-gyro radius, forms as shown in Fig.1.3(d). Subsequently, in the latter half of the '90s, it began to be reported that this current sheet at the center of the reconnection jet becomes unstable and may contribute to generation of turbulence. So far, there is no clear consensus on the mechanism to destabilize the current sheet in the scale $L_R/\lambda_i \sim \mathcal{O}(10^{1-2})$. But the relationship between turbulence and kinetic scale magnetic reconnection has been also pointed out by in-situ observations, where kinetic effects would become important. For example, in the Earth's magnetotail, the property of current sheets was extensively investigated by the Geotail satellite [68], and a power-law magnetic field spectrum was observed [45]. The spectrum has a unique "kink" structure near the ion cyclotron frequency, suggesting a multiscale phenomenon with Alfvénic turbulence. In addition, the Cluster satellite provided multi-spacecraft data of turbulence accompanying magnetic reconnection, and the properties of turbulence, such as wave dispersion, have been discussed [22].

§ 1.2 Objective and organization of this dissertation

We refer to our viewpoints on the relationship between turbulence and magnetic reconnection in the reconnection studies. Fig. 1.4 briefly summarized the above introduction. First of all, our main target is fast magnetic reconnection in high R_m plasmas whose importance is widely accepted in many explosive geophysical and astrophysical phenomena. So far, we would have four possible ways to get efficient energy conversion rate through magnetic reconnection: Petschek-type reconnection, reconnection induced by pre-existing turbulence, plasmoid instability, and kinetic reconnection. (We classified these four reconnections in the current understanding, but this may not be always robust and they may weave each other.) In particular, we focus on the second "turbulence induced macro-scale reconnection" and the last "self-generation of turbulence in kinetic scale reconnection". (The other two processes are important, but beyond the scope of this dissertation.) Objectives of these two reconnection studies are as follows:

I) When and how do plasma instabilities occur during the ion-scale kinetic magnetic reconnection? (in Chapter 2 and 3)

   In kinetic reconnection, it has already known that the reconnection rate is enough high to explain the realistic phenomena. So, the main interest is not in the reconnection rate. The main objective is to understand the ingredients (plasma instabilities) that break a laminar flow in the well developed reconnection jets. This discussion is applicable to the case where the scale gap between overall reconnection size and kinetic scale is small. The reconnection dynamics is investigated without imposing background turbulence by direct numerical simulations including ion kinetic effects.

Ⅱ) How does the pre-existing fully-developed turbulence affect the macro-scale reconnection dynamics? (in Chapter 4)

   The main objective of this issue is to suggest an idea for the turbulence-mediated fast reconnection process which may lead to an alternative way of

understanding on macroscale fast reconnection problems. Here, we want to understand the macro scale reconnection dynamics, and consider this using a turbulence model.

Issue I is discussed in Chapter 2 and 3. We limit the discussions to the basic anti-parallel magnetic field configuration. Then, wave excitation and suppression in reconnection jets are discussed from the viewpoint of self-generation of turbulence by an electromagnetic hybrid code (where ions are treated as particles while electrons are a mass-less fluid) and a linear analysis. Issue Ⅱ is discussed in Chapter 4. In this case, we consider a thick MHD scale current sheet in the pre-existing background turbulence, and the turbulent effect is discussed using a Reynolds-averaged MHD model. (In the current computational resources, it is quite difficult to solve well-developed turbulence in the inhomogeneous system directly, and the model calculation is needed.) The model deals with turbulent effects, such as the turbulent diffusion and transport, as coarse-grained integrant embedded in the macroscale system. Then, how turbulence changes reconnection dynamics is discussed. Finally, we summarize these two issues and consider their future perspectives in Chapter 5.

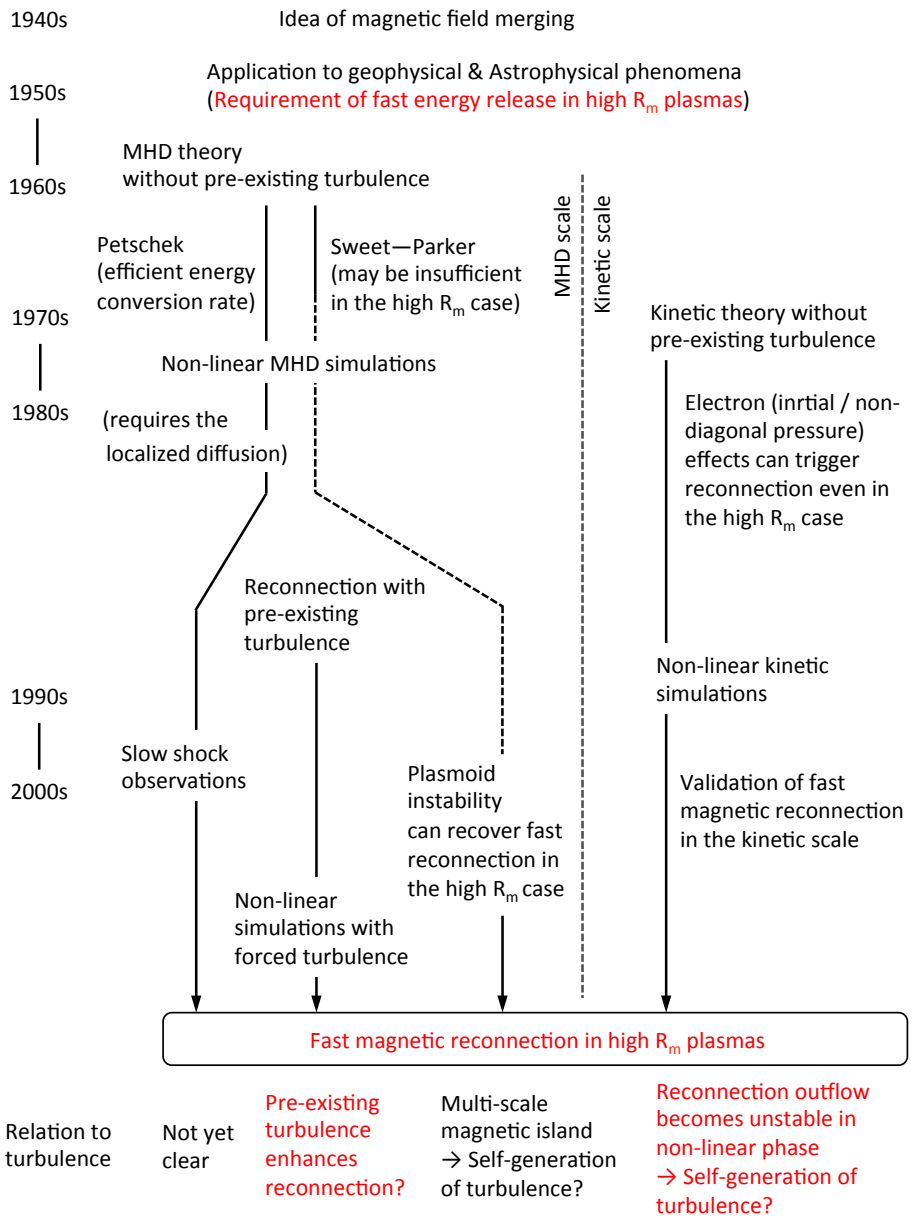

Figure 1.4: The relationship between turbulence and fast magnetic reconnection in high R_m plasmas.

CHAPTER 2

Self-generation of Alfvénic fluctuations in the ion-scale reconnection jets

Self-generated fluctuations in ion-scale collisionless magnetic reconnection is discussed using an electromagnetic hybrid code, where ion kinetic effects are included. This Chapter focuses on the points that when turbulent structures develop in ion-scale reconnection jets without pre-existing background turbulence. It is shown that reconnection jets become turbulent specifically in low beta plasmas, $\beta_{i0} < 0.1$–0.2 (β_{i0} is the ion plasma beta in initial inflow regions), and the reconnection rate slightly exceeds that of high β_{i0} cases. Statistical analysis shows that the fluctuations consist of outgoing Alfvénic fluctuations. As the probable origin of Alfvénic waves, dynamics in the plasma sheet boundary layer (PSBL) and the current sheet are discussed. It is suggested that the PSBL dynamics plays an important role for wave excitation and suppression in reconnection jets. In the PSBL, beam ions, which has been accelerated in jets, could drive Alfvén waves through the non-resonant ion–wave interaction in MHD to ion-scale, $k\lambda_i < 0.5$ (λ_i is ion inertial length), independent of β_{i0}. On the other hand, because the beam ion temperature in the PSBL is strongly correlated with that of inflowing ions, the wave damping rate by the beam ions turned to be controlled by β_{i0}. Local linear analysis suggest that the damping signature changes in β_{i0}, and energy of Alfvén waves is converted into the thermal energy of ions before they cascade down to smaller scales.

§ 2.1 Introduction

This Chapter in particular focuses on the unstable nature in ion-scale reconnection jets including ion kinetic effects. We start with a current sheet without pre-existing background turbulence. Also, we assume the region where the scale gap between overall reconnection scale and the kinetic scale is relatively small, $L_R/\lambda_i \sim 10^{1-2}$. Then, when and how laminar reconnection may fail is discussed using kinetic simulations. Based on the previous studies, the probable agents to drive Alfvénic fluctuations in reconnection jets are briefly introduced. Then, the motivation of this study is mentioned.

2.1.1 Unstable structures observed in ion-scale reconnection jets

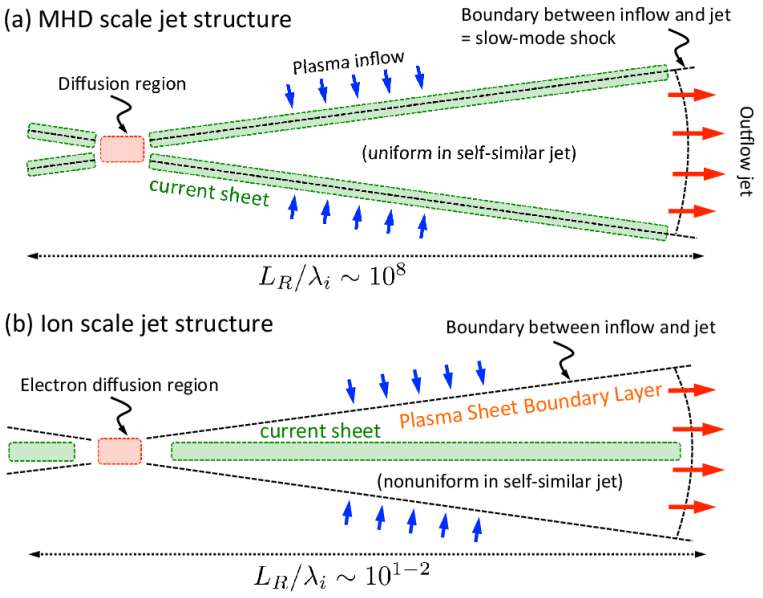

Figure 2.1: Schematic views of (a) MHD (Petschek-type) reconnection and (b) ion-scale reconnection.

As introduced in Chapter 1, the structure of ion-scale reconnection is different from that of MHD reconnection. Because such a difference is important in the following discussions, Fig.2.1 again explains this difference. In the MHD case, due to two pairs of slow mode shocks, bifurcated current sheets form. Then, velocity, density, and magnetic field structures are almost uniform inside the jet. On the other hand, in the ion-scale reconnection, a thin current sheet forms due to the Speiser type motion of ions near the diffusion region, and the magnetic field and density are nonuniform. Basically, the jet structure is decomposed into three regions: the central current sheet and two plasma sheet boundary layers (PSBLs). Such a thin ion current sheet was known to be stable when the system is in several tens of ion inertial lengths, $L/\lambda_i \sim \mathcal{O}(10)$, by kinetic particle simulations. However, as the computational resource increases, it turned out that the current sheet becomes unstable in larger scale reconnection ($L/\lambda_i \sim 10^2$) [59, 50, 2]. The present study pays much attention to this unstable nature in reconnection outflow jets. The characteristic spatial and time scales with which we deal are respectively $L/\lambda_i \sim \mathcal{O}(10^{1-2})$ and $t\Omega_i \sim \mathcal{O}(10^{1-2})$, where λ_i is ion inertial length and Ω_i is ion cyclotron frequency. On this unstable nature of reconnection jets, there have been several competing candidates to generate such unstable reconnection outflow structures: The current driven, the boundary (PSBL) driven, and the global coupling modes.

One of possible clues for the first current driven mode is a Weibel instability. The Weibel instability is driven by either temperature anisotropy $T_\perp/T_\parallel > 1$ [97] (where $T_\perp$ and $T_\parallel$ are respectively temperatures perpendicular and parallel to the local magnetic field) or counter-streaming components [24]. A current sheet is preferable to such an instability, and it has already been introduced for the current disruption mechanism in the Earth's magnetotail [62] (which is called as an ion Weibel instability). In terms of an application to magnetic reconnection, the Weibel instability is recently discussed in pair-plasma simulations. It is reported by the pair-plasma simulations that there are mainly two possible locations where the Weibel instability becomes important: In front of reconnection jets [109] and

inside the reconnection jets [88, 17]. In the pair-plasma case, it is known that the temperature anisotropy, $T_\perp/T_\parallel > 1$, becomes enough large for the Weibel mode to generate fluctuations in the jets [88] but does not affect the global reconnection rate [16]. On the other hand, in the ion-electron system, the role of Weibel mode in the reconnection jet is not yet understood.

Another probable agent which makes such current sheets unstable is ion temperature anisotropy in the boundary between inflow and outflow regions, i.e., in the PSBL. Effects of the ion temperature anisotropy and the heat flux on the reconnection boundary has been widely investigated by Geotail observations [46]. For example, Fig.2.2(a) and (b) show the slow-mode shock observation in the Earth's magnetotail region. In Fig.2.2(a), physical quantities such as magnetic field and plasma flow velocity change consistent with slow-mode shocks across the boundary (UT 15:30). Figure 2.2(b) shows the ion and electron temperature anisotropy, and it has been shown that $T_{i,\parallel}/T_{i,\perp} > 1$ and $T_{e,\parallel}/T_{e,\perp} \sim 1$ in the reconnection jet. It has also been reported by kinetic simulations that the ratio $T_{i,\parallel}/T_{i,\perp}$ becomes larger than unity in the reconnection jet [56, 59, 20]. In such a situation, an anisotropic parameter $\epsilon_{\rm ani} \equiv 1 - 0.5(\beta_{i,\parallel} - \beta_{i,\perp})$ (where $\beta_{i,\parallel}$ is the ion plasma beta parallel to the local magnetic field) often becomes smaller than zero [58, 40]. From the viewpoint of the pressure anisotropic MHD, $\epsilon_{\rm ani} < 0$ is the condition required for the fire-hose instability. For example, Fig.2.3(a)–(c) show the phase velocities of slow, intermediate, and fast modes depending on the anisotropic parameter $\epsilon_{\rm ani}$. As $\epsilon_{\rm ani}$ becomes smaller ($T_{i,\parallel}/T_{i,\perp}$ becomes larger), the intermediate mode ceases to propagate and finally becomes unstable. The possibility of the fire-hose instability in the reconnection outflow region has been discussed in kinetic simulations, and it is shown that such unstable structures are present in anti-parallel configurations but not in the guide-field reconnection because such a fire-hose mode appear in the direction parallel to the magnetic field [50].

On the other hand, from the kinetic viewpoints, it is known by both observations and simulations that the ion temperature anisotropy $T_{i,\parallel}/T_{i,\perp}$ is due from

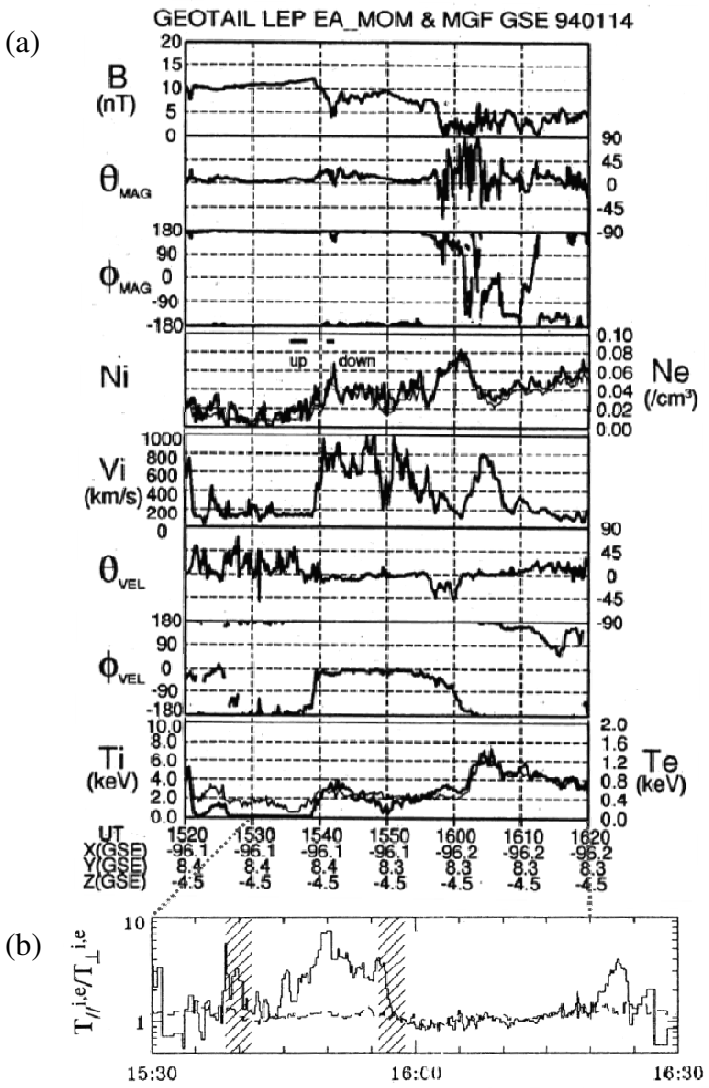

Figure 2.2: A slow shock observed on January 14, 1994 when the Geotail satellite was at $(X_{\rm GSE},\ Y_{\rm GSE},\ Z_{rmGSE}) = (-96.1R_E,\ 8.4R_E,\ -4.5R_E)$ (from [76] and [43]). From top to bottom, (a) magnetic field strength, polar and azimuthal angles in the Geocentric Solar Ecliptic (GSE) coordinate system (where $X_{\rm GSE} =$ earth-sun line, $Z_{\rm GSE} =$ ecliptic north pole, and $Y_{\rm GSE}$ is chosen in such a way that it satisfies the right-handed system), ion and electron densities, the ion bulk flow velocity, and its direction as well as magnetic field, and ion and electron temperatures, and (b) ion and electron pressure anisotropy.

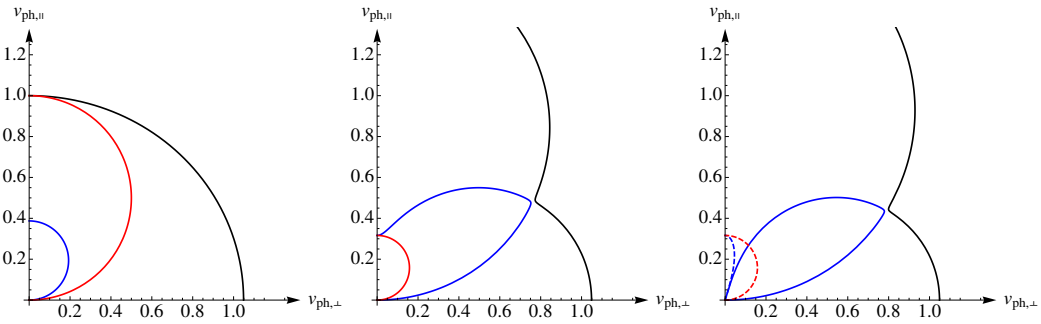

Figure 2.3: Friedrichs diagram with different anisotropic parameters (left $\epsilon_{\rm ani} = 1.0$; center $\epsilon_{\rm ani} = 0.1$; right $\epsilon_{\rm ani} = -0.1$). Black, red, and blue lines respectively stand for fast (black), intermediate (red), and slow (blue) modes. These phase velocities are calculated by the linear analysis of MHD equations with the CGL anisotropic pressure model [15]. (As for main parameters, plasma beta perpendicular to the magnetic field is set to $\beta_\perp = 0.1$, and adiabatic indexes parallel and perpendicular to the magnetic field are respectively set to $\gamma_\parallel = 3$ and $\gamma_\perp = 2$.

the existence of two ion components: One is a field aligned beam component originated from the current sheet in the reconnection jet, and the other is a cold component from the inflow region [44, 59]. Figure 2.4 shows such two ion components obtained by the hybrid simulation. From the top to the bottom, ion velocity distribution function $f_i(v_{i,x}, v_{i,y})$ (log scale), spatial distribution of $T_{i,\parallel}/T_{i,\perp}$, and magnetic field lines are shown. These two beam/inflowing ion components could trigger various kinetic instabilities, and such instabilities have been often discussed in terms of the Earth's bow shocks [29, 73]. These discussions could be also applicable for the instability in the reconnection jet, and the possibility was partially discussed using hybrid simulations [2]. For example, in the direction parallel to the magnetic field, at least four types of electromagnetic unstable modes exist, and their possibilities have already been discussed in association with the dynamics in the PSBL in the Earth's magnetotail [30]. They mainly discussed two types of growing modes: The left-handed polarized (ion-cyclotron) mode driven by the ion temperature anisotropy $T_{i,\parallel}/T_{i,\perp} < 1$ of individual ion

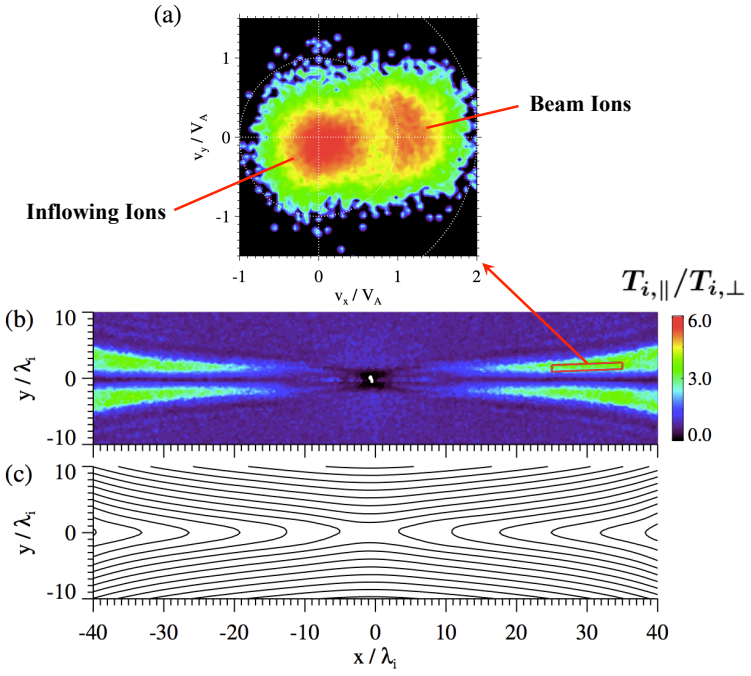

Figure 2.4: (a) The ion velocity distribution function $f_i(v_{i,x}, v_{i,y})$ in the region where $T_{i,\parallel}/T_{i,\perp} > 1$, (b) the spatial distribution of ion temperature anisotropy $T_{i,\parallel}/T_{i,\perp}$, and (c) magnetic field lines in magnetic reconnection. These figures can be obtained by hybrid simulations (almost the same results can be observed by full-particle simulations [20].).

components (the ion cyclotron anisotropy instability [28]), and the right-handed polarized (whistler) modes driven by the relative bulk velocity of two components, which macroscopically appears as ion temperature anisotropy $T_{i,\parallel}/T_{i,\perp} > 1$ (resonant and non-resonant mode instabilities [29, 98]). Here, it should be noted that in the kinetic scale no unstable mode is identical to the collisionless fire-hose mode (non-resonant mode is similar but not the same), because, in reconnection outflow jets, the ions consist of two components not of one anisotropic ion components. Such a discrepancy between MHD and kinetic signatures also makes discussions of these instabilities in magnetic reconnection difficult. The detailed analysis for the instability in PSBL has not been presented by the particle simulations for magnetic reconnection, and we should make clear how the PSBL dynamics contributes to the development of turbulent reconnection jets.

Another studies, which also focused on the ion temperature anisotropy $T_{i,\parallel}/T_{i,\perp}$ in reconnection jets, explained the instability of the thin current sheet as a global coupling mode of fire-hose and Kelvin-Helmholtz instabilities [2, 79]. They used an Alfvénic branch of incompressible MHD, and evaluated the growth rate by connecting different three layers: One anisotropic outflow layer between the other two isotropic inflow layers. They explained both temporal and spatial scales of the current sheet fluctuations by that fluid model and provided good agreement with the result of their ion-kinetic hybrid simulation.

2.1.2 Objective of this study

So far, possible agents of the instability in ion-scale reconnection jets have been suggested, but detailed analysis, such as parameter dependence of the reconnection jets, does not exist. In collisionless plasmas, wave–particle interactions, such as cyclotron resonance (damping) will have a large impact on the dynamics, and such a system is expected to evolve in different ways, depending on the plasma parameters. This Chapter aims to provide an understanding of the complicated signature of reconnection jets, including such aspects. First, we consider the con-

ditions when turbulent reconnection exhausts are observed, and show that current sheets develop into Alfvénic turbulence, particularly for low beta reconnection. Next, keeping the parameter dependence in mind, ingredients to generate Alfvén waves are discussed based on the local linear analysis: the current driven and the PSBL driven modes. (The analysis for the global mode mentioned in the introduction is discussed in Chapter 3, because it needs further analysis and discussions beyond the local analysis.) In Section 2.2, the simulation model and the setup are introduced. We show the results and discuss them in Sections 2.3 and summarize them in Section 2.4.

§ 2.2 Numerical Model and Setup

A two-dimensional (in x-y plane) electromagnetic hybrid code, where ions and electrons are respectively treated as kinetic particles and a mass-less fluid, is adopted to investigate self-generated turbulent structures in ion-scale reconnection outflows. The basic equations that we solve are as follows:

$$m_i \frac{d\boldsymbol{v}_i}{dt} = q_i \left(\boldsymbol{E} + \boldsymbol{v}_i \times \boldsymbol{B} \right), \tag{2.1}$$

$$\frac{d\boldsymbol{x}_i}{dt} = \boldsymbol{v}_i, \tag{2.2}$$

$$\boldsymbol{E} = -\frac{1}{q_i n_i} \boldsymbol{\nabla} \cdot \overleftrightarrow{\boldsymbol{P}_{\rm e}} - \boldsymbol{V}_e \times \boldsymbol{B} + \lambda_r \boldsymbol{\nabla} \times \boldsymbol{B}, \tag{2.3}$$

$$\boldsymbol{V}_e = \boldsymbol{V}_i - \frac{1}{q_i n_i} \boldsymbol{\nabla} \times \boldsymbol{B}, \tag{2.4}$$

$$n_i = \int_{-\infty}^{\infty} f_i(\boldsymbol{x}_i, \boldsymbol{v}_i, t) d\boldsymbol{v}_i, \tag{2.5}$$

$$\boldsymbol{V}_i = \frac{1}{n_i} \int_{-\infty}^{\infty} \boldsymbol{v}_i f_i(\boldsymbol{x}_i, \boldsymbol{v}_i, t) d\boldsymbol{v}_i, \tag{2.6}$$

$$\frac{\partial \boldsymbol{B}}{\partial t} = -\boldsymbol{\nabla} \times \boldsymbol{E}. \tag{2.7}$$

λ_r is the resistive length. In addition to the above set of equations, a charge neutral condition $en_e = q_i n_i$ is assumed, where subscripts e and i respectively stand for electrons and ions, and an ion is assumed to be a proton hereafter. The electron is assumed to be adiabatic gas with isotropic pressure ($\overleftrightarrow{\boldsymbol{P}}_{\rm e} = p_e \overleftrightarrow{\boldsymbol{I}}$ and $p_e \propto n_e^{\gamma_{\rm adi}} = n_i^{\gamma_{\rm adi}}$, where $\gamma_{\rm adi} = 5/3$ is an adiabatic constant). The above quantities are normalized using the proton mass, m_p, the ion cyclotron frequency, $\Omega_{i*} = eB_*/(m_p c)$, and the ion inertial length, $\lambda_{i*} = \Omega_{i*}/V_{A*}$, where $V_{A*} = B_*/\sqrt{4\pi m_p n_{i*}}$ and the subscript $_*$ stands for the quantity in the initial inflow region (see Chapter C). n_{i*} is the ion density. Grid intervals in both x- and y-directions are set to $0.33\ \lambda_{i*}$.

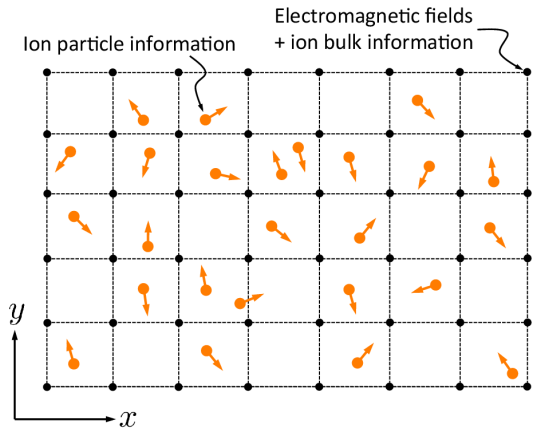

Figure 2.5: A schematic view of hybrid particle simulation domain.

In the hybrid simulation, ions are randomly distributed in the simulation domain, while the electromagnetic fields are located on the grid points (see Fig. 2.5). Each ion moves around by Eqs.(2.1)–(2.2) in the given electromagnetic fields, and the electromagnetic fields develop with the effect of ion bulk quantities, Eqs.(2.5)–(2.6). In this study, the above equations are solved by the algorithm of general predictor-corrector loops, which has been successfully used in collisionless shocks, current sheets, collisionless magnetic reconnection, beam dynamics

and global simulation of the interaction of solar wind with objects[1][98].

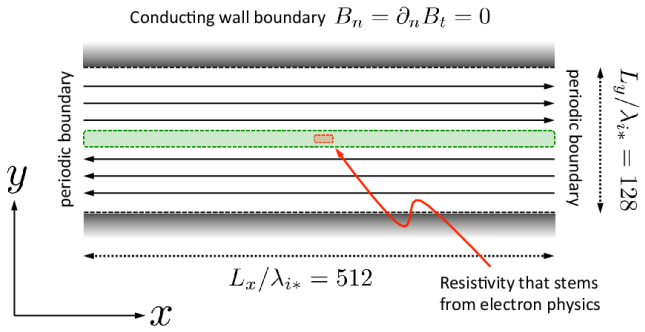

Figure 2.6: Initial configuration for the simulation.

Initially, we assume a Harris current sheet with no guide magnetic field ($B_z = 0$) [37], and the configuration is shown in Fig. 2.6. The magnetic field, density, and velocity profiles are given by

$$\boldsymbol{B} = B_0 \tanh\left(\frac{y}{\delta_c}\right)\boldsymbol{e}_x, \tag{2.8}$$

$$n_i(y) = n_{i0} + n_{ic}\cosh^{-2}\left(\frac{y}{\delta_c}\right), \tag{2.9}$$

$$\boldsymbol{V}_{ib} = \boldsymbol{0}, \tag{2.10}$$

$$\boldsymbol{V}_{ic} = -\frac{2v_{i,th}^2}{\delta_c}\boldsymbol{e}_z \tag{2.11}$$

where Subscripts 0 and c stand for the quantity in the initial inflow region and the

[1] Details of hybrid simulations are described in [57]. Hybrid codes are known to be numerically unstable in low density plasmas, and some authors begin to address its solution [27, 1].

central current sheet, respectively ($B_0 = 1$, $n_{i0} = 1$). δ_c is a half thickness of the initial current sheet and δ_c is set to $1.2\ \lambda_{i*}$. $\boldsymbol{e}_x$ is an unit vector in x-direction, and the initial current is in the z-direction. $v_{i,th} = (T_{ic}/m_i)^{1/2}$ is the thermal velocity in the current sheet, where T_{ic} is the ion temperature in the current sheet. In the current sheet, the ion temperature, T_{ic}, is set to $T_{ic} = 0.125$. The electron temperature is uniformly given, $T_{ec} = T_{e0} = 0.01$. The ion density at the center of the current sheet n_{ic} is determined by the relation, $n_{ic}(T_{ec} + T_{ic}) = B_0^2/(8\pi)$, which stems from the total pressure balance in the y-direction between the current sheet and the lobe regions. The simulation box is in the range of $-256 \leq x/\lambda_{i*} \leq 256$ in x-direction and $-64 \leq y/\lambda_{i*} \leq 64$ in y-direction. Periodic boundary conditions are assumed in x-direction, while perfect conducting walls [59] are assumed at $y/\lambda_{i*} = \pm 64$. The number of super-particles in each cell is about 250 in initial inflow regions ($\sim 10^3$ super-particles in the current sheet). We drive reconnection by imposing the time-independent resistivity, $\lambda_r(x, y)$, at the center of the simulation box as $\lambda_r(x, y) = \lambda_0 \cosh^{-2}\left[-(x/l_x)^2 - (y/l_y)^2\right]$, where λ_0 is the resistive length and set to 0.075. l_x and l_y are set to $l_x = 1.2\ \lambda_{i*}$ and $l_y = 0.6\ \lambda_{i*}$, respectively. So far, it has been suggested that the resistivity originates from the electron physics, such as the electron inertial effect [94], the non-diagonal electron pressure effect [39], and anomalous transport induced by turbulence [12, 25]. This diffusion region physics is currently a hot topic, and the detail description is beyond the capability of the present hybrid simulation study. The choice of the above resistivity leads to well-developed reconnection jets. (At least, the existence of the large-scale reconnection jets has been often reported by the Earth's magnetotail observations [76] and full-particle simulations [20, 58].)

In the present study, the dependence of the initial ion plasma beta on the development of the reconnection exhausts is investigated. Parameters are summarized in Tab.2.1. We change the ion plasma beta in initial inflow regions by varying ion temperature T_{i0} with Alfvén velocity constant (Runs A–D). In other words, we change the ion cyclotron radius. All other parameters are the same among A–D. Note that the initial temperature is given isotropically and the ion temperature

anisotropy, which we discuss below, is generated by the inherent physics in collisionless magnetic reconnection. The ion temperatures parallel and perpendicular to the local magnetic field are defined by

$$T_{i,\parallel} = \frac{m_i}{n_i} \int_{-\infty}^{\infty} \left(|\boldsymbol{v}_i - \boldsymbol{V}_i| \cos\theta\right)^2 f_i(\boldsymbol{x}_i, \boldsymbol{v}_i, t) d\boldsymbol{v}_i, \tag{2.12}$$

$$T_{i,\perp} = \frac{m_i}{2n_i} \int_{-\infty}^{\infty} \left(|\boldsymbol{v}_i - \boldsymbol{V}_i| \sin\theta\right)^2 f_i(\boldsymbol{x}_i, \boldsymbol{v}_i, t) d\boldsymbol{v}_i, \tag{2.13}$$

where $\theta = \arccos\left[(\boldsymbol{v}_i - \boldsymbol{V}_i) \cdot \boldsymbol{B} / \left(|\boldsymbol{v}_i - \boldsymbol{V}_i| B\right)\right]$. The total ion temperature T_i can be written by $T_i = (T_{i,\parallel} + 2T_{i,\perp})/3$ in the above definitions. The plasma beta in Run A is nearly equivalent to that in the Earth's distant magnetotail. For example, T_{i0} is equivalent to ~ 50 eV if we choose normalization velocity as $V_{A*} = 10^3$ km/s (which is characteristic Alfvén velocity in the Earth's magnetotail lobes).

Table 2.1: Simulation parameters for reconnection.

Run	β_{i0}	$T_{i0}/(m_p V_{A*}^2)$	n_{i0}/n_{i*}	V_{A0}/V_{A*}
A	0.02	0.01	1.0	1.00
B	0.08	0.04	1.0	1.00
C	0.18	0.09	1.0	1.00
D	0.32	0.16	1.0	1.00

§ 2.3 Results and Discussion

2.3.1 Ion beta dependence on the development of fluctuations in reconnection jets

Basic signature of unstable current sheet

Let us begin with the basic signature of the unstable current sheet. (Note that the unstable current sheet has already shown by previous studies [59, 50], but this

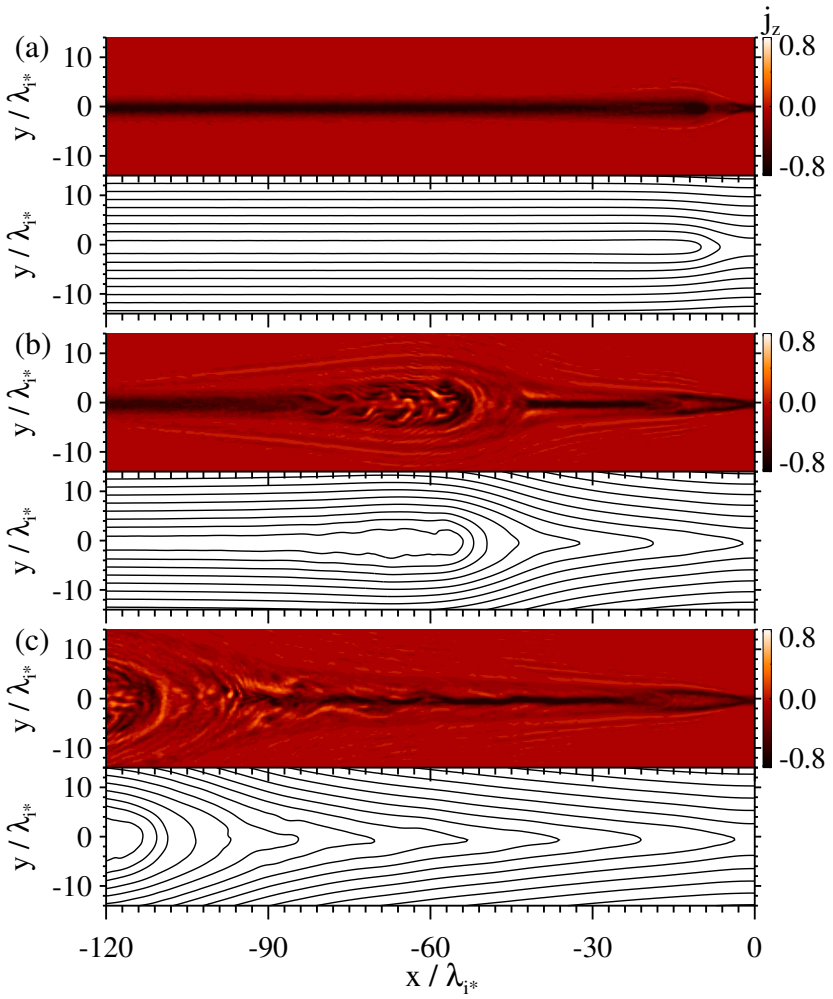

Figure 2.7: From top to bottom, snapshots of the total current, j_z, and magnetic field lines at (a) $t\Omega_{i*} = 100$, (b) 200, and (c) 300 for the $\beta_{i0} = 0.08$ case are shown. Magnetic neutral point is located in $(x, y) = (0, 0)$, and only a part of simulation box is shown here.

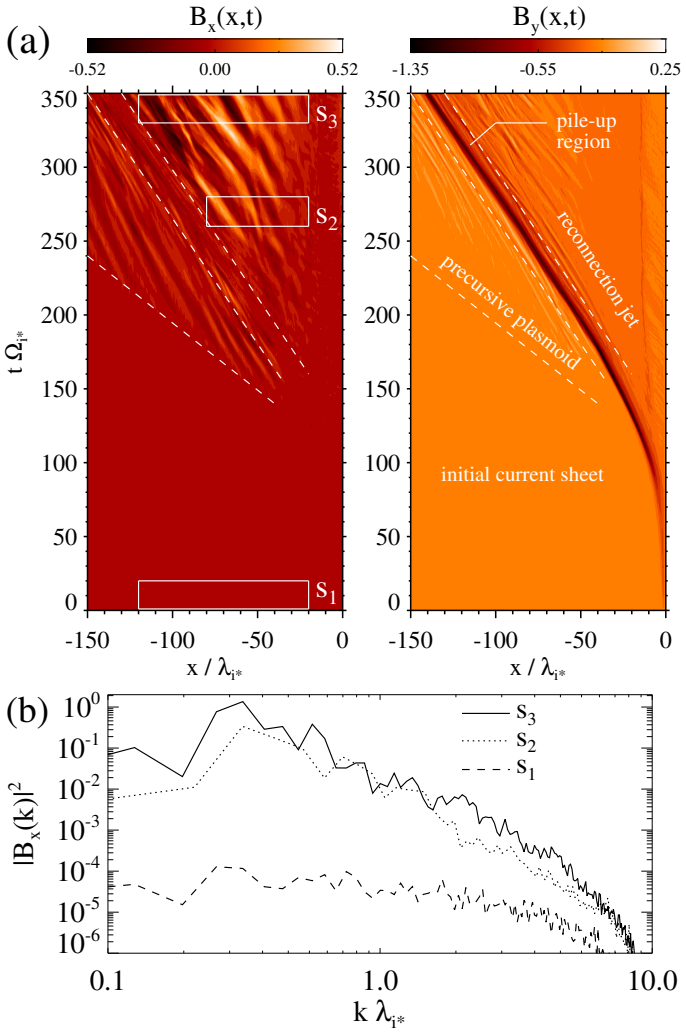

Figure 2.8: (a) Time evolution of x and y components of the magnetic field at $y = 0$, $B_x(x,t)$ and $B_y(x,t)$. The white dashed lines divide the space into the initial current sheet, the precursive plasmoid, the pile-up region in front of the jet, and the reconnection jet region. (b) Fourier spectra calculated by regions s_1 (the initial current sheet), s_2 and s_3(the reconnection jet) shown in Fig.(a). The spectra are averaged with time.

part addresses detail signatures that when and where the instability takes place.) Figure 2.7 shows the time evolution of the total electric current, j_z, and magnetic field lines in $\beta_{i0} = 0.08$ case. The snapshots are taken at time $t\Omega_{i*} =$ (a) 100, (b) 200, and (c) 300. (Only a part of the simulation box is shown here.) The magnetic field lines reconnect with each other at $x/\lambda_{i*} \sim 0$, and a thin current sheet forms at the center of the reconnection jet (see the snapshot at (b) $t\Omega_{i*} = 200$). Thickness of the current sheet is about an ion gyro radius and the current is mainly carried by Speiser-type motion of the ions [85, 23]. Subsequently, the current sheet becomes unstable (see the snapshot at (c) $t\Omega_{i*} = 300$). In order to closely discuss where and when such unstable structures emerge, we show time evolution of B_x and B_y at $y/\lambda_{i*} = 0$ in Fig. 2.8(a). Reconnection starts in $t\Omega_{i*} = 60$–80 and B_y is strengthened in the pile-up region. In $t\Omega_{i*} < 150$, the laminar reconnection develops without fluctuations. Fluctuations first emerge in the precursive plasmoid (see $x/\lambda_{i*} \sim -60$ in Fig. 2.7(b) and Fig.2.8(a)), and subsequently the unstable structure appears inside the reconnection jet. When the current sheet becomes unstable, the sheet length exceeds ~ 30–$50\ \lambda_{i*}$ ($t \sim 200$–$250\ \Omega_{i*}^{-1}$). Since the boundaries in the x-direction are in $x/\lambda_{i*} = \pm 256$ and far from the neutral point, the fluctuations are not affected by boundary conditions. Also, because the flow speed is super-Alfvénic in the neutral sheet, $y/\lambda_{i*} \sim 0$, these fluctuations stem from the upstream dynamics. As the size of the jet becomes larger, the current sheet shows turbulent structures. Figure 2.8(b) shows power spectra of the magnetic field in the initial current sheet, s_1, and in the reconnection jet, s_2–s_3 (respectively calculated using the data in the white boxes in Fig. 2.8(a)), and the spectra develops as time passes.

Ion beta dependence on the development of jets

One of the important suggestions that should be addressed in this unstable jet signature is that the evolution quite differs depending on the ion plasma betas, β_{i0}. Figure 2.9 shows the current sheet structures of the reconnection exhausts depending on β_{i0}. The z component of the total current j_z is shown in the contour

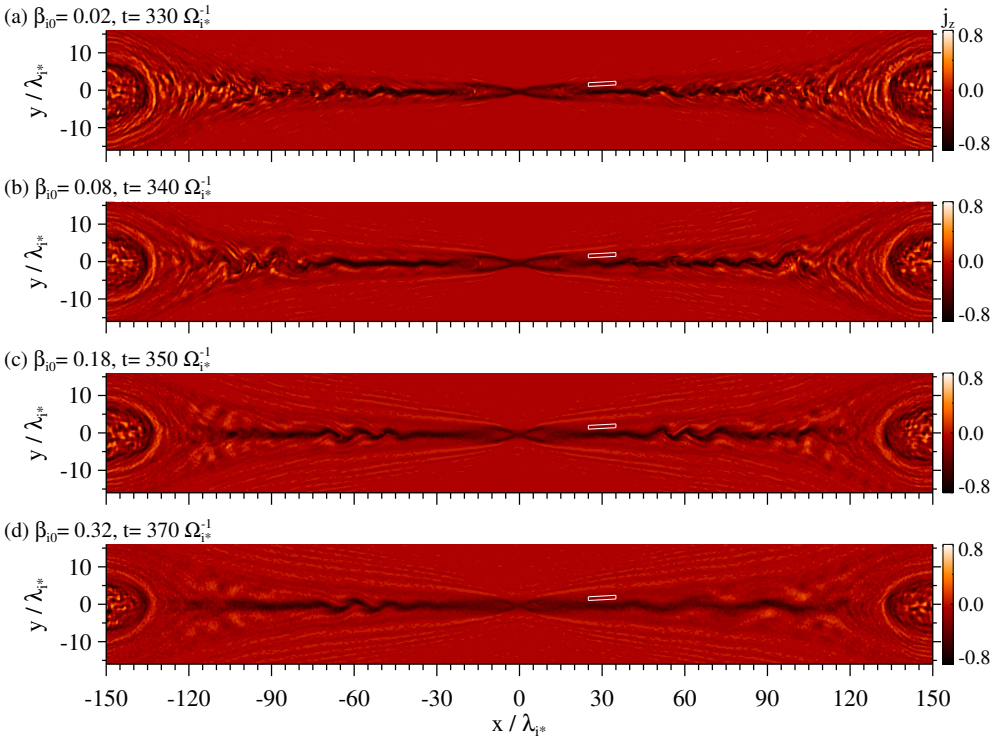

Figure 2.9: From the top to the bottom, electric current density j_z (upper panels), magnetic field lines (black lines in the lower panels) and ion bulk flow lines (blue lines in the lower panels) for Runs A–D are shown, respectively.

panels. The plasma jets encounter pile-up regions at $|x|/\lambda_{i*} \sim 130$. In all cases, fluctuations in the reconnection jets are observed from a distance $|x|/\lambda_{i*} \sim 30$ away from the X-point. However, on increasing the distance from the X-point, the evolution of these fluctuations shows a different behavior: these current sheets easily break up as β_{i0} decreases.

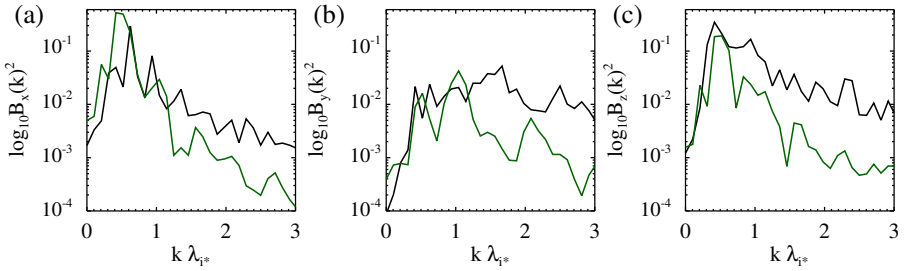

Figure 2.10: Power spectra for the magnetic field components, B_x, B_y and B_z, in the range $-120 < x/\lambda_{i*} < -60$ for $y/\lambda_{i*} = 0$. The black and green lines denote the power spectra for Runs A and D, respectively.

Figure 2.10 shows these differences in the power spectra $|B_x(k)|^2$, $|B_y(k)|^2$, and $|B_z(k)|^2$ on a logarithmic scale. The magnetic field components, B_x, B_y, and B_z, at $y/\lambda_{i*} = 0$ in the range $-120 < x/\lambda_{i*} < -60$ are chosen to calculate the spectra. The spectra are averaged over 20 Ω_{i*}^{-1} with time. In Fig. 2.10(b), the magnetic field cascades down to the smaller scales (a few ion inertial lengths) specifically in low beta cases, while not so in high beta cases. The reason for this would be related to wave excitation and damping processes occurring inside the reconnection jet, and details will be discussed in the next subsection.

In addition to the difference in the spectra, there is also changes in the reconnection rate. Figure 2.11 shows time profiles of the inflow Alfvén Mach number, $M_{A,\mathrm{in}}$, the inflow velocity, V_{in}, the reconnected magnetic field, Λ_R, and reconnec-

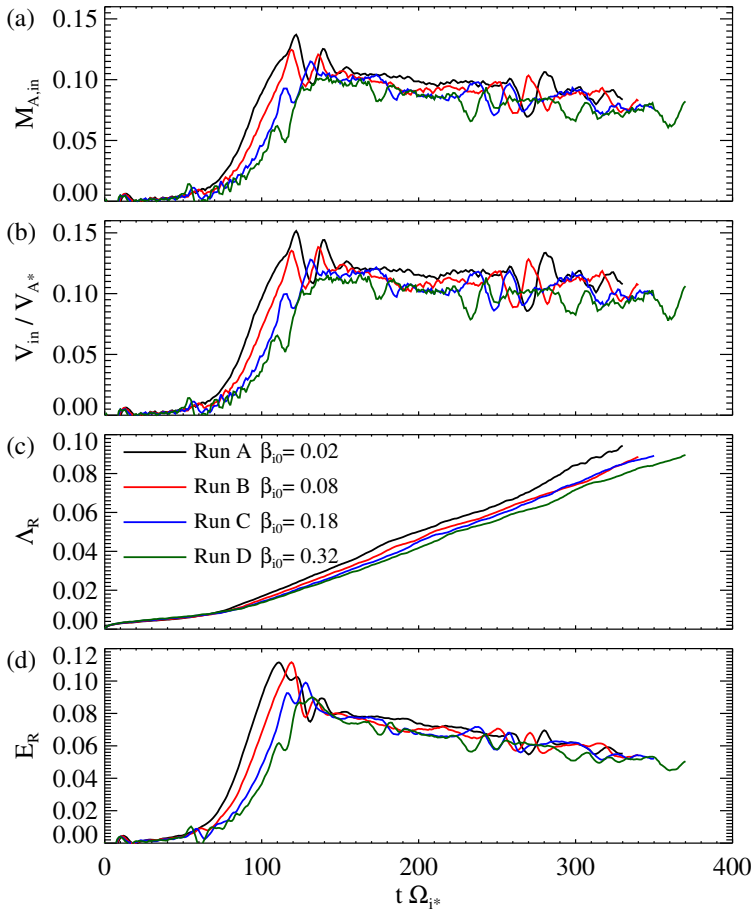

Figure 2.11: Time profiles of (a) inflow Mach number, $\mathcal{M}_A$, (b) inflow velocity, V_{in}, (c) reconnected magnetic flux, Λ_R, and (d) reconnection electric field, E_R.

tion electric field, E_R,:

$$M_{A,\mathrm{in}} \equiv \frac{1}{2D_x}\left\{\int_{-D_x/2}^{+D_x/2} dx \left[\left.\frac{V_y}{V_{AL}}\right|_{y=-D_y/2} - \left.\frac{V_y}{V_{AL}}\right|_{y=+D_y/2}\right]\right\}, \tag{2.14}$$

$$V_{\mathrm{in}} \equiv \frac{1}{2D_x}\left\{\int_{-D_x/2}^{+D_x/2} dx \left(V_y|_{y=-D_y/2} - V_y|_{y=+D_y/2}\right)\right\}, \tag{2.15}$$

$$\Lambda_R \equiv \frac{1}{L_x}\int_{-L_x/2}^{+L_x/2} dx \left|B_y(x)\right|_{y=0}, \tag{2.16}$$

$$E_R \equiv \frac{1}{D_x D_y}\int_{-D_x/2}^{+D_x/2} dx \int_{-D_y/2}^{+D_y/2} dy \left|E_z(x,y)\right|, \tag{2.17}$$

where $D_x = 30\ \lambda_{i*}$, $D_y = 10\ \lambda_{i*}$, and L_x is the box size in the x-direction. V_{AL} is the local Alfvén velocity. In low beta turbulent reconnection, the reconnection rate slightly exceeds that of high beta cases, which implies further energy transfer occurs in turbulent jets.

Property of fluctuations

Let us discuss the properties of such low beta turbulent reconnection jets. To grasp the nature of fluctuations and their spatial distribution quantitatively, we introduce a turbulent statistical quantity, cross-helicity, $\mathcal{W}(x,y) \equiv \langle (\boldsymbol{V}_i' \cdot \boldsymbol{B}') \,/\, (|\boldsymbol{V}_i'|\,|\boldsymbol{B}'|)\rangle$, which is often used to discuss Alfvénicity of turbulence, e.g., in the solar wind [64, 34]. Here, the cross-helicity is normalized by $|\boldsymbol{V}_i'|\,|\boldsymbol{B}'|$ for the purpose of convenience. The brackets $\langle\rangle$ represent a time averaged value. Note that the wave momentum is carried by the ions ($m_e = 0$), and the cross-helicity is defined using only the ion bulk velocity. The terms $\boldsymbol{V}_i'$ and $\boldsymbol{B}'$ are the fluctuating parts of ion bulk velocity and magnetic field, respectively. (The velocity fluctuation is defined by $\boldsymbol{V}_i' = \boldsymbol{V}_i - \langle \boldsymbol{V}_i \rangle$.) Basically, a finite cross-helicity distribution is related to the generation or asymmetric propagation of Alfvén waves.

Figure 2.12 shows the spatial distributions of: (a) the mean magnetic field, $\langle B_z \rangle$, (b) the temporal magnetic field, B_z, (c) the mean ion velocity, $\langle V_{iz} \rangle$, (d)

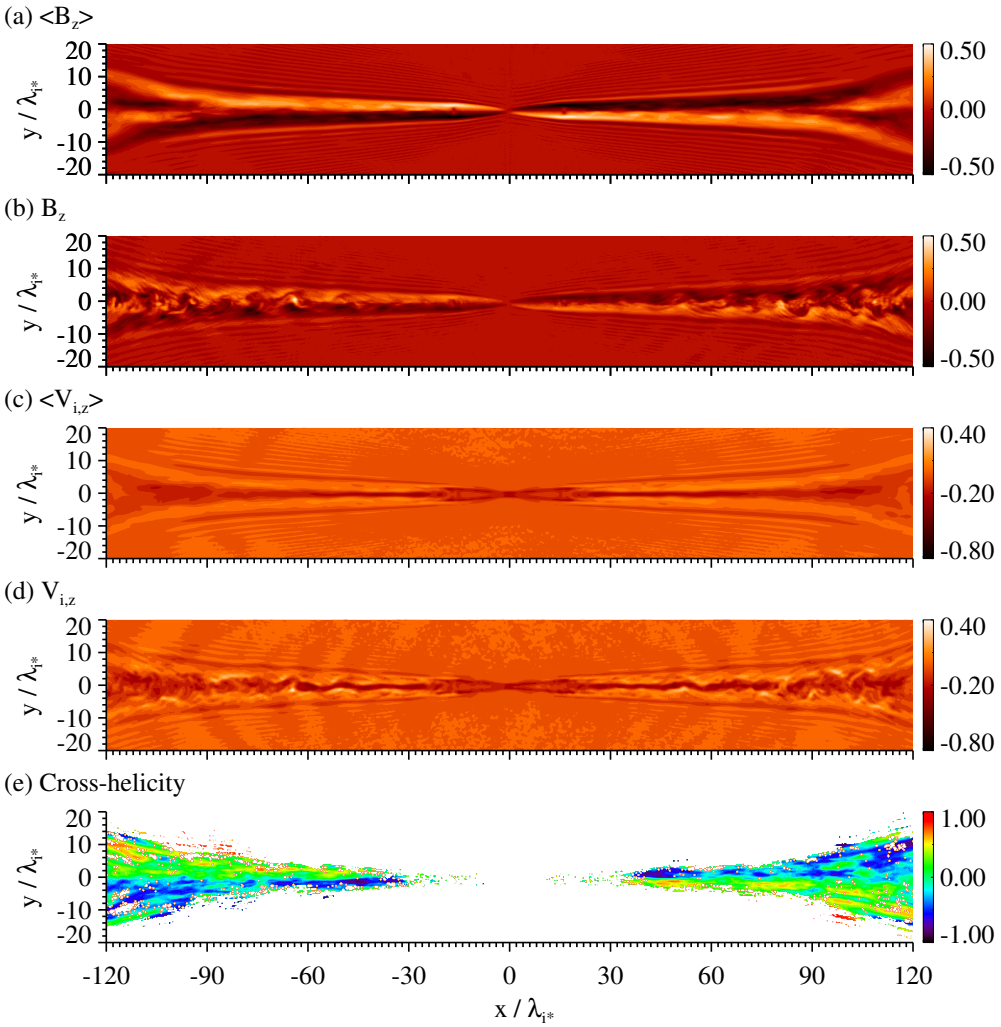

Figure 2.12: Spatial distributions of: (a) the mean Hall magnetic field, $\langle B_z \rangle$, (b) the Hall magnetic field, B_z, at $t = 330\ \Omega_{i*}^{-1}$, (c) the mean ion flow velocity, $\langle V_{iz} \rangle$, (d) the ion flow velocity, V_{iz}, at $t = 330\ \Omega_{i*}^{-1}$, and (e) the (normalized) cross-helicity $\langle (\boldsymbol{V}_i' \cdot \boldsymbol{B}') \,/\, (|\boldsymbol{V}_i'|\,|\boldsymbol{B}'|) \rangle$. Time averages $\langle\rangle$ are taken in the range of $t = 300$–$330\ \Omega_{i*}^{-1}$ for 31 data. In Fig. (e), the region where the fluctuation level is low, $|\boldsymbol{V}_i'|\,|\boldsymbol{B}'| < 5 \times 10^{-4}$, is masked for convenience.

the temporal ion velocity, V_{iz}, and (e) the cross-helicity, $\mathcal{W}$. The time range used to calculate the integration, $\langle\rangle$, is $t = 300$–$330\ \Omega_{i*}^{-1}$. In time-averaged exhausts, the out-of-plane Hall magnetic field and ion velocity, which are generated by the in-plane Hall current and the out-of-plane ion Speiser motion, respectively, are still present in Figs 2.12(a) and (c). In such mean field structures, fluctuations emerge. It is important to note that the fluctuation variables, such as velocity and magnetic field, are not distributed randomly but have a certain correlation. Figure 2.12(e) shows this correlation, i.e., a quadrupole structure of the cross-helicity. A finite cross-helicity distribution denotes a situation where the fluctuations are Alfvénic and predominantly consist of outgoing Alfvén waves. Cross-helicity begins to appear from the ion current region, and the origin of these waves seems to be mainly outside the electron diffusion region, where electron kinetic effects becomes important and the physics is beyond this hybrid model. Outside the electron diffusion region, inflowing magnetic field energy is converted into ion kinetic energy through electrostatic acceleration in the current sheet, and these ions obtain free energy as temperature anisotropy and bulk flow energy as mentioned in the introduction of this Chapter (seeFig. 2.4). It is suggested that a part of the free energy is once again released as wave energy, and not only the ions but also the Alfvén waves would transfer energy outward.

2.3.2 Alfvénic fluctuations in reconnection jets: Local analysis

The problem—and our main interest— is why such Alfvénic fluctuations appear specifically in low beta plasmas. In this section, we investigate the upstream jet regions, $|x|/\lambda_{i*} < 60$, where waves are expected to grow linearly. That is, keeping the ion beta dependence in mind, the possible ingredients to generate Alfvénic waves in the PSBL and the current sheet regions are discussed, based on the local analysis.

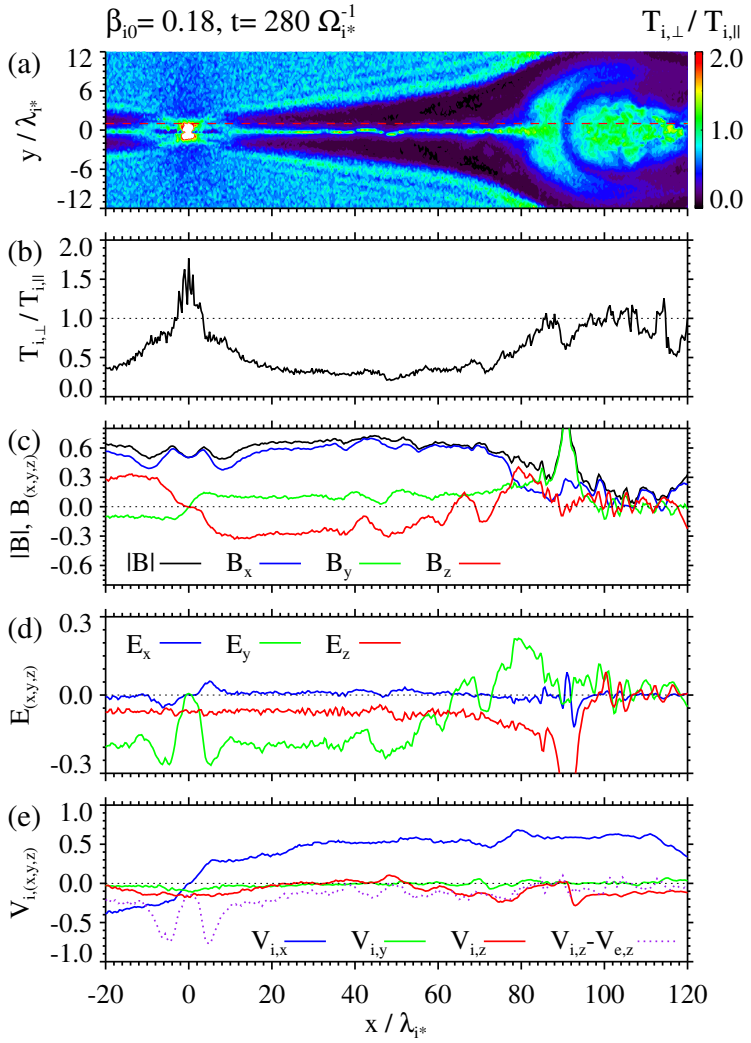

Figure 2.13: Physical quantities in the reconnection jets for Run C are shown. From top to bottom: (a) the spatial distribution of the ion temperature anisotropy, $T_{i,\perp}/T_{i,\parallel}$, and (b)–(e) the distribution of physical quantities in the red dashed line.

Plasma sheet boundary layer

First, let us focus on the dynamics in the PSBL. In the PSBL, the ion anisotropy, $T_{i,\parallel}/T_{i,\perp} > 1$, is enhanced and is one of the most probable free energy sources for waves. Figure 2.13 shows: (a) ion temperature anisotropy, $T_{i,\perp}/T_{i,\parallel}$, and (b)–(e) the cross-sectional physical quantities outside but close to the edge of the current sheet. For $30 < x/\lambda_{i*} < 60$ in Figs 2.13(c) and (d), the magnetic field is mainly in the x-direction, ($|\mathbf{B}| \simeq B_x$), and the transverse fluctuations (B_y, B_z, E_y, and E_z) can be clearly observed, which implies an Alfvénic mode excitation is occurring. In this region, $T_{i,\parallel}$ is always a few times larger than $T_{i,\perp}$, as seen in Fig. 2.12(b). For further discussion, we show the ion velocity distribution function, $f_i(v_x, v_y)$, for Runs A–D in Fig. 2.14. These velocity distribution functions are calculated by integrating super-particles inside the white boxes shown in Fig. 2.9. The velocity is normalized to the local Alfvén velocity, where the subscript L denotes the local quantity inside the white box (see also Table 2.2). These ion distribution functions consist of beam ions (the right-side component) and inflowing ions (the left-side component). It is important to note that both the relative velocity, V_0 ($\simeq 2V_{AL} \simeq 1.2V_{A*}$), and the beam-to-total density ratio, n_b/n_{iL} ($\simeq$ 0.4–0.5), have about the same value independent of β_{i0}. This means that the inflowing ions gain about the same magnitude of energy, $\simeq m_{i*}V_{A*}^2/2$, during non-gyro motion at $y/\lambda_{i*} \sim 0$. In addition, the temperature of the beam ions shows good agreement with that of the inflow ions, which is because the ion motion is quasi-adiabatic even for the non-gyro motion. (In the jet, almost all ions experience the Speiser type motion, and such ion motion is shown to be nearly adiabatic [11, 14].)

Let us discuss the linear properties of electromagnetic modes driven by the two ion components in the PSBL as a function of β_{i0}. The dispersion relation for these components is

$$\frac{k^2c^2}{\omega^2} = 1 + \sum_{j=e,c,b} \left[\frac{\omega_{p,j}^2}{\omega^2} \zeta_j^{(0)} \mathcal{Z}(\zeta_j^{(\pm 1)}) \right] \tag{2.18}$$

[28] (only parallel modes are discussed here). The subscripts $j = e$, c and

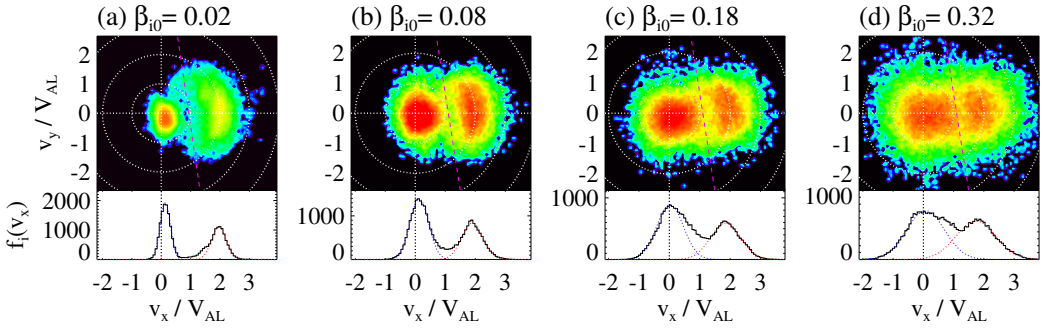

Figure 2.14: Ion velocity distribution functions, $\log_{10} f_i(v_x, v_y)$ (upper contour) and $f_i(v_x)$ (lower histogram). The velocities, v_x and v_y, are normalized to the local Alfvén velocity. The two ion components are divided by the magenta dashed lines in the upper contour. The blue and red dotted lines in the lower panels are the Maxwellian fits for the inflowing ions and beam ions, respectively.

Table 2.2: Local quantities inside the white boxes shown in Fig. 2.9.

Run	B_L	n_{iL}	V_{AL}	n_b/n_{iL}	$T_c/(m_{i*}V_{AL}^2)$
A	0.60	1.09	0.57	0.48	0.03
B	0.66	1.27	0.58	0.38	0.12
C	0.65	1.21	0.59	0.40	0.27
D	0.66	1.26	0.59	0.40	0.48

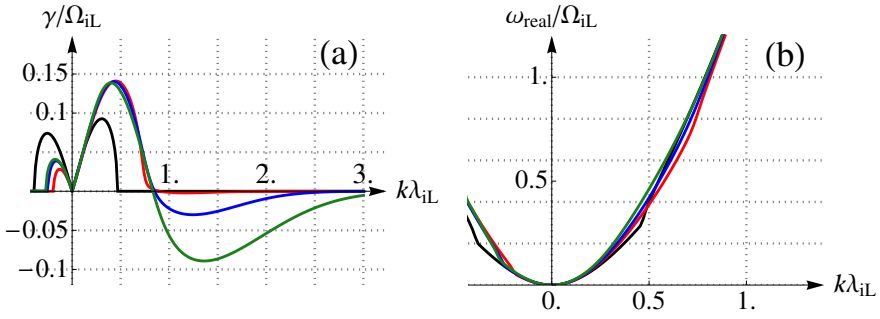

Figure 2.15: Right-handed polarized electromagnetic modes for the parameters given in Table 2.2. Figures (a) and (b) show the growth rates and real frequency in Runs A–D, respectively.

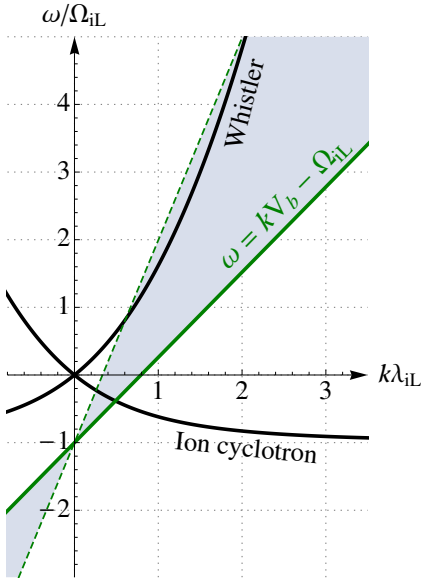

Figure 2.16: Damping effects in the plasma rest frame for the case of high ion beta (Run D). The cyclotron resonance condition is shown by a green line, where $V_b = +V_0(n_{iL} - n_b)/n_{iL}$. The ashed green line represent the thermal broadening, $\omega = k(V_b + 2.5v_{th,i}) - \Omega_{iL}$ (where $v_{th,i} = (T_c/m_i)^{1/2}$), and the blue shaded area represents the cyclotron damping region due to beam ions.

b represent electrons, core ions (inflowing ions), and beam ions, respectively. $\omega_{p,j}$ is the plasma frequency, $\mathcal{Z}$ is the plasma dispersion function, and $\zeta_j^{(n)} = (\omega - kV_j + n\,|\Omega_j|) \,/\, \left(\sqrt{2}kv_{j,th}\right)$, where $v_{j,th}$ is the thermal velocity parallel to the magnetic field $v_{j,th} \equiv \left(T_{j,\parallel}/m_j\right)^{1/2}$. Figure 2.15 shows the imaginary and real parts of ω, which are normalized to the local cyclotron frequency Ω_{iL}. The parameters used to draw Fig. 2.15 are summarized in Table 2.2, and are estimated from the ion distribution functions shown in Fig. 2.13. We assumed that $T_b/T_c = 1$ (beam/core temperature ratio) and $V_0 = 2.1\ V_{AL}$ (the relative bulk velocity between beam and core ions). (Also, $T_e = 0.01$ is used.) In Fig. 2.15(a), both the parallel and anti-parallel whistler waves are unstable ($\gamma > 0$) in $k\lambda_{iL} < 0.5$, independent of the initial conditions, but the damping signatures ($\gamma < 0$) are different, depending on the ion plasma beta. In the reconnection jet frame, since the relative bulk speed of the two ion components is not fast enough to excite whistler waves from cyclotron resonance, the waves are excited by non-resonant interactions independent of β_{i0} [30]. On the other hand, since the beam temperature is strongly correlated with the inflow temperature through the quasi-adiabatic motion, the thermal broadening of the beam ions contributes to wave damping on increasing the temperature of the inflowing ions. This damping signature is briefly explained using Fig.2.16. This figure explains the interaction between beam ions (core ions as well) and Alfvénic waves in the plasma rest (reconnection jet) frame for the Run D case. The green solid line represents the cyclotron resonance condition between beam ions ($T_{ib} = 0$) and Alfvén waves, $\omega - kV_b - \Omega_{iL} = 0$. V_b is the beam speed in the plasma rest frame, $V_b = V_0(n_{iL} - n_b)/n_{iL}$, and is estimated using the data shown in Table 2.2. The dashed green line represents the thermal broadening of beam ions, and the blue shaded area represents the cyclotron damping region due to beam ions. As temperature of beam ions increases, the cyclotron damping region broadens and the Alfvén (whistler) wave energy in $k\lambda_{i*} \gtrsim 1$ is absorbed by beam ions. That is, as the value of β_{i0} increases, the wave energy is once again converted into ion (thermal) energy in $k\lambda_i \sim 1$, before cascading down to smaller scales. These results suggest such a difference appears in $\beta_{i0} \sim 0.1$–0.2 in the

PSBL, and this provides good agreement with nonlinear simulation results, where the fluctuations are suppressed in the cases of $\beta_{i0} = 0.18$ and 0.32 (Run C and D).

In addition, it is worth noting that waves driven in the PSBL could contribute to the generation of turbulence in the neutral sheet. In the outflow jets, the local Alfvén velocity in the PSBL is $\sim 0.6\ V_{A*}$, and is $V_{AL} \sim 0.1\ V_{A*}$ in the current sheet. Therefore, the refractive index for the Alfvén wave, $N_A \propto V_{AL}^{-1}$, decreases as $|y|/\lambda_{i*}$ increases, and the PSBL Alfvén waves are always refracted into the current sheet.

Current sheet

As another candidate, we briefly refer to the possibility of a local Weibel instability in the current sheet. Figure 2.17 shows the ion temperature anisotropy, $T_{i,\perp}/T_{i,\parallel}$, and magnetic field in the cross section $y/\lambda_{i*} \simeq 0$. The simulation data are the same as those shown in Fig. 2.13. At the center of the current sheet, $T_{i,\perp}/T_{i,\parallel}$ is almost unity, and the anisotropy is much smaller than that of the pair–plasma system [88] (independent of the value of the initial plasma beta). In addition, in Fig. 2.17(b), B_y (the eigenvector of the Weibel mode) is stable compared with B_x and B_z. Therefore, we concluded that the Weibel mode does not participate in the ion–electron reconnection dynamics. As for the B_x and B_z fluctuations, we suggest that these are attributable to the coherent kinking current structure seen in Fig. 2.7 (clearly observed for $-70 < x/\lambda_{i*} < -30$). Such a coherent current fluctuation itself may not be explained solely by the local effects discussed above. This point was first pointed out by [2] based on the simple MHD model. However, a discussion on such a global mode itself is beyond the scope of this local analysis.

§ 2.4 Summary

We have discussed the self-generated fluctuations in collisionless ion-scale magnetic reconnection based on the results of the hybrid simulation and the local linear

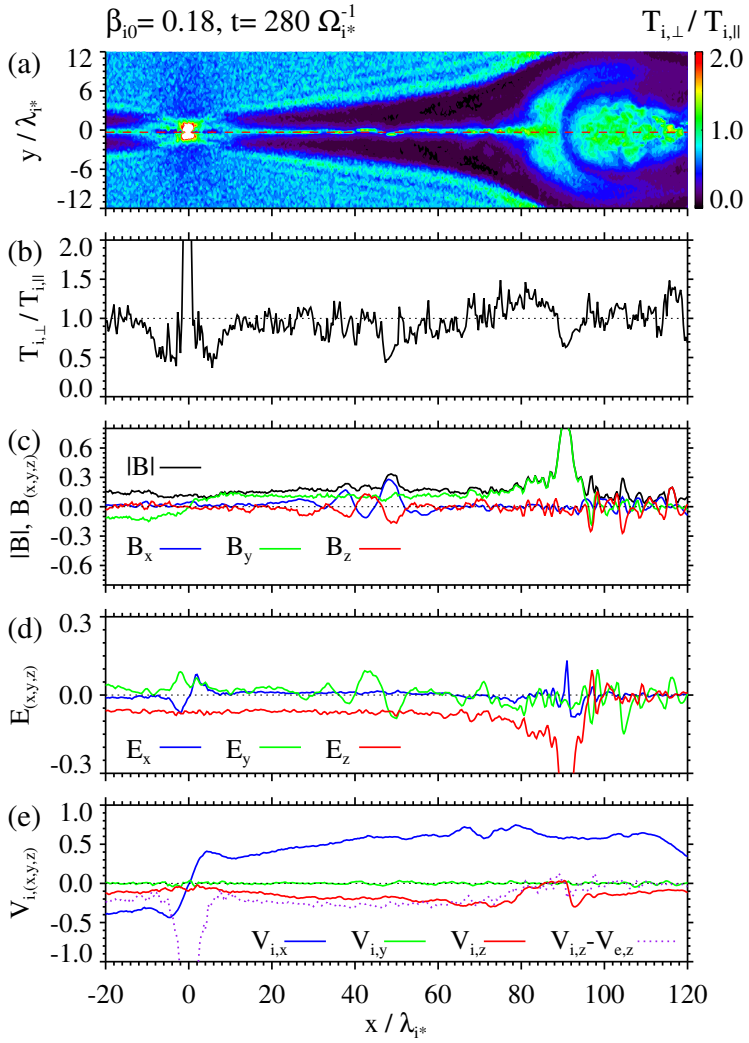

Figure 2.17: Physical quantities in the reconnection jets for Run C are shown. From top to bottom: (a) the spatial distribution of the ion temperature anisotropy, $T_{i,\perp}/T_{i,\parallel}$, and (b)–(e) the cross-sectional physical quantities in the red dashed line.

analysis. The unstable signature of the reconnection jet has already been reported by some preceding studies [59, 50, 2]. Also, some possible mechanisms to generate fluctuations (such as the Weibel mode in the current sheet [88, 17] and the instability in the PSBL [30]) have been suggested, but their detailed contribution to the ion-scale jet dynamics has not been so clear. We carefully analyzed the reconnection jets obtained by the hybrid simulation with different initial conditions, and addressed some important issues on the condition and the ingredients to control wave activities in the reconnection jet.

1 Whether the reconnection jet becomes turbulent or not is related to the ion plasma beta, β_{i0}, in the inflow region. The simulation results show that the jet becomes turbulent in low beta cases ($\beta_{i0} < 0.1$–0.2), while it looks less turbulent in high beta cases.

2 The local linear analysis in the PSBL showed that the ion temperature anisotropy is enough large to excite Alfvén waves independent of β_{i0} in the PSBL. On the other hand, the wave damping signature is different depending on β_{i0}: the damping rate becomes large as β_{i0} increases ($\beta_{i0} > 0.1$–0.2). This threshold seems to be in good agreement with nonlinear simulation results, suggesting the importance of wave excitation and suppression in the PSBL.

3 In the current sheet of the present ion-electron system, the temperature anisotropy, $T_\perp/T_\parallel$, is small compared to that of the pair–plasma system, and the Weibel mode does not participate in the ion-electron reconnection jet dynamics.

In the low beta condition, we checked the correlation between magnetic field and velocity fluctuations by using the cross-helicity, and the fluctuations in the jets are shown to consist of outgoing Alfvénic wave packets that transfer the electromagnetic energy outward. Also, the reconnection rate in the low beta case slightly increases compared to the high beta case. Local analysis in upstream regions, $|x|/\lambda_{i*} < 60$, suggests that PSBL dynamics would play an important part in generation and suppression of Alfvénic modes, while the Weibel mode is irrelevant to

the ion-electron reconnection jet dynamics. In the PSBL, because both the beam speed and the density show little difference for all β_{i0} cases, the Alfvén waves could be driven by non-resonant interactions at longer wavelengths ($k\lambda_{i*} < 0.5$) independent of β_{i0}. At the same time, we note that ion motions in jets preserve temperature information well, and that the damping rate caused by hot beam ions may be controlled by the ion beta in the inflow regions. Local linear analysis suggests that low beta jets ($\beta_{i0} < 0.1$–0.2) are free from wave damping for the smaller scales, $k\lambda_{i*} > 0.5$. In addition, since the local Alfvén velocity in the neutral sheet is small compared with that in the PSBL, the Alfvén waves driven in the PSBL are refracted toward the neutral sheet and contribute to the generation of turbulence in the reconnection jets. Observations of low β_{i0} turbulent reconnection jets in the Earth's magnetotail have been presented recently [22] and our results seem to be consistent with them. On the other hand, in high β_{i0} cases, the wave damping rate is enough large to suppress Alfvénic modes in $k\lambda_{i*} \sim 1$ and the fluctuations in this range would not survive in the reconnection jets. As a result, the high beta reconnection outflow is suggested to be laminar without small scale fluctuations.

In the above discussions, it should be noted that the reconnection jet has strong inhomogeneity across the outflow and the unstable nature in such a complex system will not be explained by only the above local discussions. At least, the globally emerging structure (e.g., kinking current sheet structures observed in Fig 2.9) cannot be explained by only the above local discussions. This point is discussed in the next Chapter 3 in detail.

CHAPTER 3

Analysis for a global magneto-hydro-dynamic mode in reconnection jets

A global magneto-hydro-dynamic mode observed in reconnection jets is discussed by a linear eigenmode analysis. The main objective of this Chapter is to account for the global instability observed in the nonlinear reconnection jet (namely, a kinking current sheet structure beyond the discussions by the local analysis in Chapter 2). Aside from the reconnection jet, it has been suggested by the previous linear eigenmode analysis that there are three MHD unstable modes in the streaming current sheet: the resistive tearing, the non-resistive sausage, and the non-resistive kink modes. According to the previous analysis with isotropic plasma pressure approximation, the resistive tearing and the non-resistive sausage modes dominates in the streaming current sheet, and it is suggested that the kink mode is unimportant in the current sheet dynamics. In order to resolve such discrepancy between simulations (including anisotropy) and the previous analysis, we considered the linear stability including both non-uniformity and pressure anisotropy effects. We carefully investigated properties of unstable modes in the streaming current sheet, and the analysis suggests that the symmetric sausage mode is an Alfvén type mode, and the property seems to be independent of non-uniformity and the pressure anisotropy. On the other hand, the kink mode shows the slow Alfvén type property, where the globally-appearing magnetic pressure gradient force always weakens the magnetic tension force, and is sensitive to pressure anisotropy effects. Additionally, the linear growth rate of the kink mode considerably exceeds that of the sausage mode in the case of $p_{\parallel}/p_{\perp} > 1$ ($p_{\parallel}$ and $p_{\perp}$ are the pressures parallel and perpendicular to the ambient magnetic field), suggesting an importance of kink mode in reconnection jets of anisotropic plasmas.

§ 3.1 Introduction

Dynamics in MHD to ion-scale reconnection jets are theoretically investigated. In Chapter 2 the origin of Alfvén waves in the PSBL and a current sheet was discussed from a local kinetic viewpoint. However, only the local discussion cannot explain the global unstable structure across the current sheet in reconnection jets. Figure 3.1 again shows the time evolution of such a global current sheet structure. The parameter and the model of this simulation are the same as the hybrid simulation Run C in Chapter 2, and the X-point is located at $(x, y) = (0, 0)$. The kinking current sheet structure appears when both the time and the spatial scales become $\sim 10^2\ \Omega_{i*}^{-1}$ and $\sim 10^2\ \lambda_{i*}$, where Ω_{i*} and λ_{i*} are respectively the ion cyclotron frequency and the ion inertial length in the inflow region. In the reconnection jet, magnetic field non-uniformity (a current sheet at the center of the jet), ion (electron) bulk velocity, and the ion pressure anisotropy develop in a macroscopic scale. The main target of this Chapter is to clarify the behavior of such a global mode in ion-scale reconnection jets, including ingredients, such as pressure anisotropy and non-uniformity in jets. The brief introduction and the objective is mentioned below. In section 3.2 and 3.3, the linear analysis of the above global mode is presented.

3.1.1 Preceding studies on the streaming current sheet dynamics

After *Furth, Killeen, and Rosenbluth* (FKR) made a great progress for a current sheet stability [26], many succeeding studies on the nature of a current sheet, such as Hall [89] and pressure anisotropy effects [13], have been made. As one of such studies, the property of a current sheet with finite plasma flow has been investigated by some researchers [78, 83, 55, 2].

The stability of the collimated jet has been investigated with and without magnetic field. For example, in the case of neutral fluid, the collimated jet nature has been investigated, and it is known that the jet has both symmetric and antisymmetric unstable modes [6]. In the MHD case, the property of a magnetized

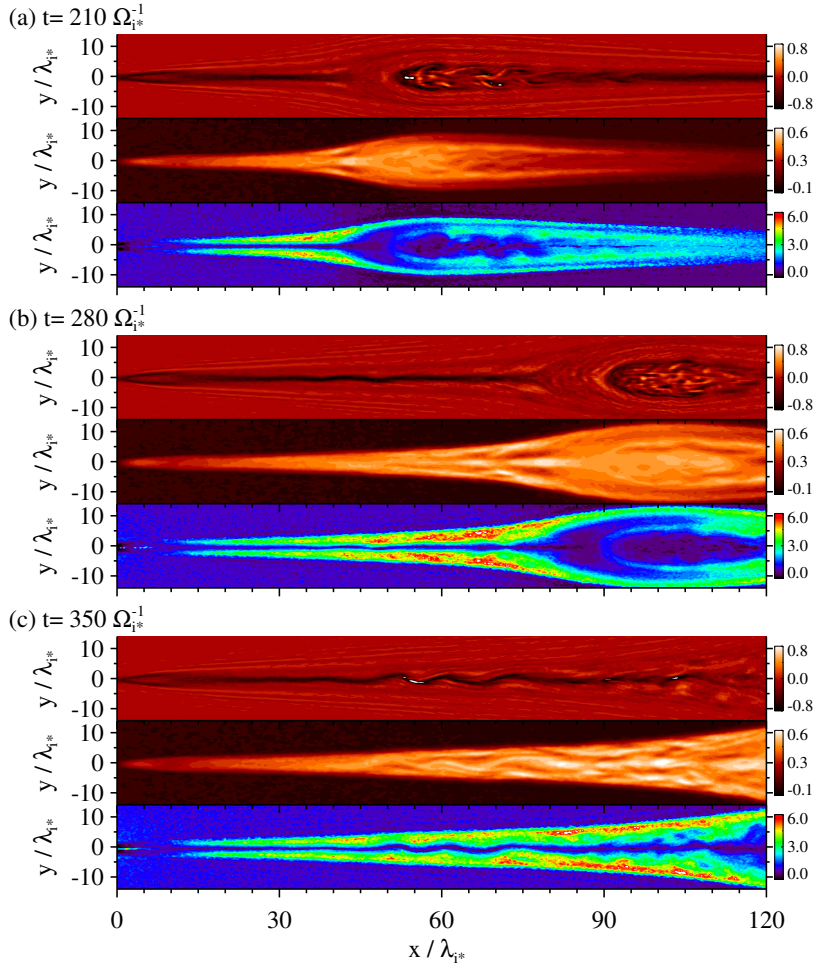

Figure 3.1: The time evolution of the electric current, j_z (upper contour), the outflow ion velocity, V_{ix} (middle contour), and the ion temperature anisotropy, $T_{i,\parallel}/T_{i,\perp}$ (lower contour) are shown. The snapshots are taken at (a) $t = 210\ \Omega_{i*}^{-1}$, (b) $t = 280\ \Omega_{i*}^{-1}$, and (c) $t = 350\ \Omega_{i*}^{-1}$.

jet was first investigated by nonlinear MHD simulations [78]. They examined the current sheet stability with the plasma flow along the ambient anti-parallel magnetic field, and found that the tearing mode grows faster than that of the usual Harris current sheet. Then, it was shown theoretically by the linear eigenmode analysis that the growth rate and the unstable wavenumber of the tearing mode become larger as the flow speed increases [83]. Subsequently, the linear analysis of the magnetized jet with isotropic pressure approximation showed that there are three possible global unstable mode in jets: the resistive streaming tearing mode, the non-resistive kink and sausage modes [55]. The sausage mode symmetrically grows with respect to the neutral sheet, while the kink mode anti-symmetrically grows. They suggest that the sausage mode grows much faster than the kink mode and the kink mode is unlikely to grow in the parameter associated with reconnection jet.

On the other hand, as the computational resources increases, some hybrid simulations, which include ion kinetic effects beyond MHD, began to report that the kink mode appears in nonlinear MHD to ion-scale reconnection jets [59, 50, 2]. The appearance of kinking current sheet structure in reconnection jets was first pointed out in [59], and the modeling of the global reconnection jet structure was attempted by [2]. They consider three layers associated with reconnection jet structures: two lobes and the outflow region between them. Using the model, they attempted to explain basic properties, such as growth rate and wavelength. They seem to explain the unstable signature in the reconnection jets. However, the detailed analysis, such as eigenvector and parameter dependence, has not been shown, and whether the kink mode exceeds the sausage mode or not is still ambiguous.

3.1.2 The objective of this Chapter

The objective of this Chapter is to explain the non-local instability observed in reconnection jets. For this purpose, at least, we aim to understand

1 the property of the global unstable modes,

2 non-uniformity in the reconnection jet,

3 pressure anisotropy,

in parallel, and discuss the instability in anisotropic inhomogeneous reconnection jets. In what follows, a simple three layer model, which is the first attempt to discuss the global mode in reconnection jets, are first introduced in Section 3.2, and the remaining problem to explain the instability in jets are mentioned. Then, in Section 3.3, the property of unstable modes, including the effects of non-uniformity and pressure anisotropy, are discussed by the linear eigenmode analysis.

§ 3.2 Linear analysis by the simple three layer model

In this section, the basic properties of global unstable modes are discussed based on a simplified three layer model that was suggested by [2]. Among three modes shown by [55], non-resistive modes can be considered here in association with the reconnection jet.

3.2.1 A review of *Arzner & Scholer* three layer model

In the well developed X-type magnetic reconnection, the outflow region mainly consists of two lobes (inflow regions) and a jet region. In order to discuss a global MHD instability there, *Arzner and Scholer* considered simplified three layers as shown by Fig.3.2. In each layer, we could assume different physical quantities which reflect the parameters in reconnection outflows (such as the density, the velocity, and the pressure anisotropy).

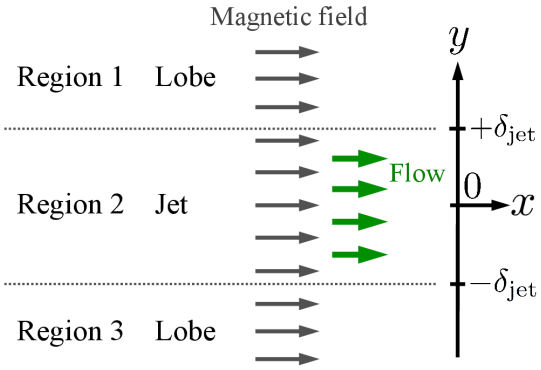

Figure 3.2: A schematic view of the three layer model in the x-y plane.

Since the objective is to discuss the kinking current sheet structure in reconnection jets, they use the y component of the equation of motion and the induction

equation:

$$\rho_0 \frac{d\tilde{V}_y}{dt} = -\frac{\partial \tilde{p}_t}{\partial y} + \epsilon_0 \left(\boldsymbol{B}_0 \cdot \boldsymbol{\nabla}\right) \tilde{B}_y, \tag{3.1}$$

$$\frac{\partial \tilde{B}_y}{\partial t} = -\frac{\partial}{\partial x}\left(V_{x0}\tilde{B}_y - B_{x0}\tilde{V}_y\right), \tag{3.2}$$

$$\tilde{V}_y = \frac{d\tilde{y}}{dt}, \tag{3.3}$$

where $d/dt = \partial/\partial t + (\boldsymbol{V}_0 \cdot \boldsymbol{\nabla})$, $\tilde{p}_t$ is the total perturbed pressure, and ϵ_0 is an anisotropic parameter, defined by $1 - \left(p_\parallel - p_\perp\right)/B_{x0}^2$. For the purpose of convenience, the fluctuation of y displacement, $\tilde{y}$, is introduced in their analysis. Ambient magnetic field, B_0, is in the x-direction, and only parallel modes are discussed here with inhomogeneity in the y-direction, i.e., $\boldsymbol{\nabla} = (ik_x, \partial_y, 0)$. Note that the pressure perturbation may couple with Alfvén waves because of the non-uniformity in the y-direction. Combining Eqs. (3.1)–(3.3) gives the equation,

$$\xi_r \tilde{y} = \frac{\partial \tilde{p}_t}{\partial y}, \tag{3.4}$$

where $\xi_r = \rho_0 \left(k_x V_0 - \omega\right)^2 - \epsilon_0 k_x^2 B_0^2$. The subscript $_r$ stands for the region on which we focus ($r = 1, 2, 3,$ or $r = \mathrm{jet}, \mathrm{lobe}$). In order to consider the non-uniformity in the y-direction, the total pressure is assumed to be the form of $\tilde{p}_{t,r} = \phi_r e^{-k_x y} + \psi_r e^{k_x y}$. Since the amplitude of the perturbation goes to zero in $y \to \pm\infty$, it is reduced to the form of

$$\tilde{p}_t(x, y) = \exp\left[i\left(k_x x - \omega t\right)\right] \times \begin{cases} \phi_1 e^{-k_x y} & (y > \delta_{\mathrm{jet}}) \\ \phi_2 e^{-k_x y} + \psi_2 e^{k_x y} & (-\delta_{\mathrm{jet}} \le y \le \delta_{\mathrm{jet}}) \\ \phi_3 e^{k_x y} & (y < -\delta_{\mathrm{jet}}) \end{cases} \tag{3.5}$$

Then, the connectivity of $\tilde{p}_t$ and $\tilde{y}$ at $y = \pm\delta_{\mathrm{jet}}$ for different three layers gives the

relationship for the above coefficients, ϕ_r and ψ_r,

$$\begin{pmatrix} 1 & -1 & -e^{2k_x\delta_{\rm jet}} & 0 \\ 0 & e^{2k_x\delta_{\rm jet}} & 1 & -1 \\ \xi_2 & -\xi_1 & \xi_1 e^{2k_x\delta_{\rm jet}} & 0 \\ 0 & \xi_3 e^{2k_x\delta_{\rm jet}} & -\xi_3 & \xi_2 \end{pmatrix} \begin{pmatrix} \phi_1 \\ \phi_2 \\ \psi_2 \\ \psi_3 \end{pmatrix} = \mathbf{0}, \tag{3.6}$$

and taking the determinant expansion of the above 4×4 matrix gives the following dispersion relation for the three layer interaction mode,

$$\left(\xi_{\rm lobe}^2 + \xi_{\rm jet}^2\right)\tanh\left(2k_x\delta_{\rm jet}\right) + 2\xi_{\rm lobe}\xi_{\rm jet} = 0. \tag{3.7}$$

For simplicity, symmetric lobes are assumed (r; $2 = \text{jet}$, $1 = 3 = \text{lobe}$). In the above model, we need nine parameters to discuss the global stability: the half-thickness of the plasma jet, $\delta_{\rm jet}$, the densities, $\rho_{0,\rm jet}$ and $\rho_{0,\rm lobe}$, the bulk flow velocities, $V_{0,\rm jet}$ and $V_{0,\rm lobe}$, the local Alfvén velocities, $V_{A,\rm jet}$ and $V_{A,\rm lobe}$, and the pressure anisotropy, $\epsilon_{0,\rm jet}$ and $\epsilon_{0,\rm lobe}$. From Eq.(3.1) and the setup (three layers with different velocity), the instability considered to be the pressure anisotropy (such as fire-hose and mirror instabilities) and velocity shear (such as Kelvin-Helmholtz instability (KHI)) coupling mode.

3.2.2 Results and Discussion: parameter dependence of the instability and modes

Here, the instability in reconnection jets and the basic properties are discussed using the above three layer model. In the followings, the parameters related to the above model is evaluated using nonlinear hybrid simulation results that was presented in Chapter 2, and the detailed properties of unstable modes, such as eigenvectors and the parameter dependence, are investigated.

Physical quantities in the nonlinear reconnection jet

Let us first check the realistic reconnection jet parameters from hybrid simulation data presented in Chapter 2. The left panels in Fig. 3.3 show the cross sectional quantities in $x/\lambda_{i*} = 45$ for Fig.2.7 associated with the three layer model; the ion density, n_i, the x-component of the ion bulk velocity, V_{ix}, the local Alfvén velocity, $V_{AL} = B/\sqrt{n_i}$, and the anisotropic parameter, $\epsilon_{\rm ani} = 1 - \left(p_{\parallel} - p_{\perp}\right)/B^2$. The vertical black dotted lines at $y/\lambda_{i*} = \pm 3$ divide the region into a jet and two lobes, and the averaged values in the lobe and the jet regions are shown in the right panels. The color in the left panels represents the ion beta in the initial inflow regions and is the same as that shown in Chapter 2.

The ion density, the outflow velocity, the Alfvén velocity, and the pressure anisotropy are roughly the same in the jet region independent of the ion beta. As discussed above, because the model is sensitive to outflow speed and the pressure anisotropy, $V_{x,\rm jet}$ and $\epsilon_{\rm ani,jet}$ are chosen as free parameters. The other parameters are set as Table 3.1. Additionally, the jet width, $\delta_{\rm jet} = 3.0\ \lambda_{i*}$. The listed quantities are normalized as $n_i = n_i/n_{i*}$ and $V_A = V_A/V_{A*} = V_A B_*^{-1}\sqrt{n_{i*}}$, where n_{i*} and B_* are normalization constants.

Table 3.1: Parameters from hybrid simulations for magnetic reconnection

	Density, n_i	Outflow velocity, V_{ix}	Alfvén velocity, V_A	Pressure anisotropy, $\epsilon_{\rm ani}$
Lobe	0.9	0.0	0.9	1.0
Jet	1.5	Free parameter	0.5	Free parameter

Basic property in isotropic jets

First, the property of the global mode in isotropic plasmas is examined using the parameter shown in Table 3.1. $\epsilon_{\rm ani,jet}$ is set to unity, because of the isotropy. We have four solutions in Eq.(3.7), and two of them are growing modes. Figure 3.4 shows the growth rates for these two physical modes as a function of wavenumber and jet speed. The white dashed line on the contour plot is a threshold for the KHI

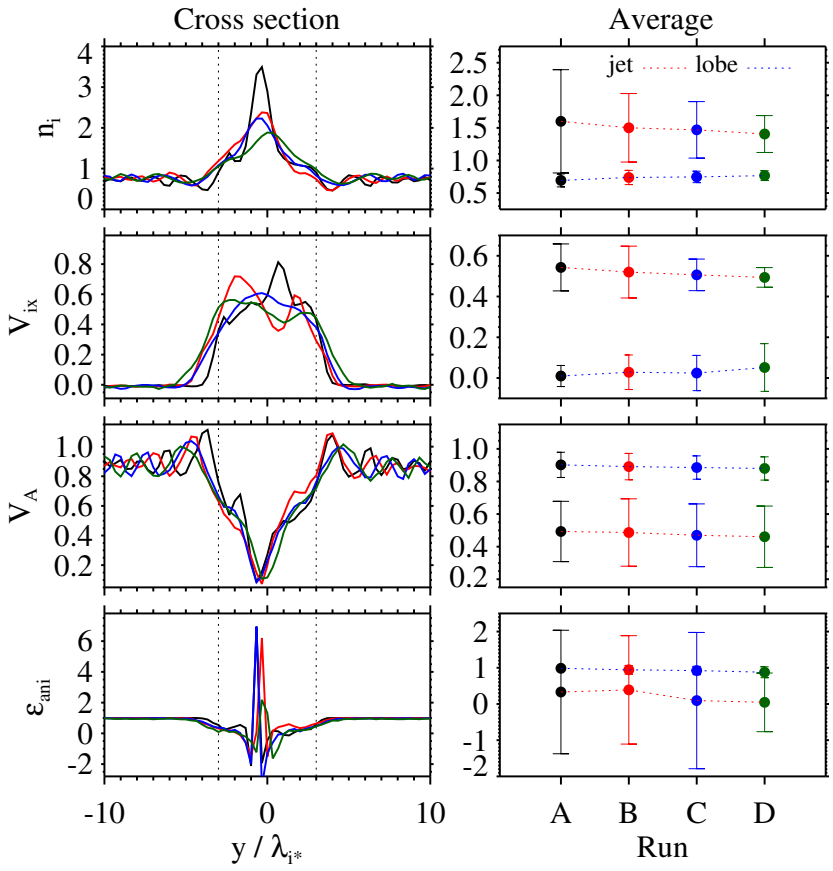

Figure 3.3: Left panels: Physical quantities associated with parameters of three-layer model in the cross section $x/\lambda_{i*} = 45$. Right panels: Averaged values and the standard deviations in jet and lobe regions for each Run.

occurring between a lobe and a jet. This threshold is calculated by considering only the upper connectivity between the lobe and jet regions. These two modes are unstable beyond the KHI threshold.

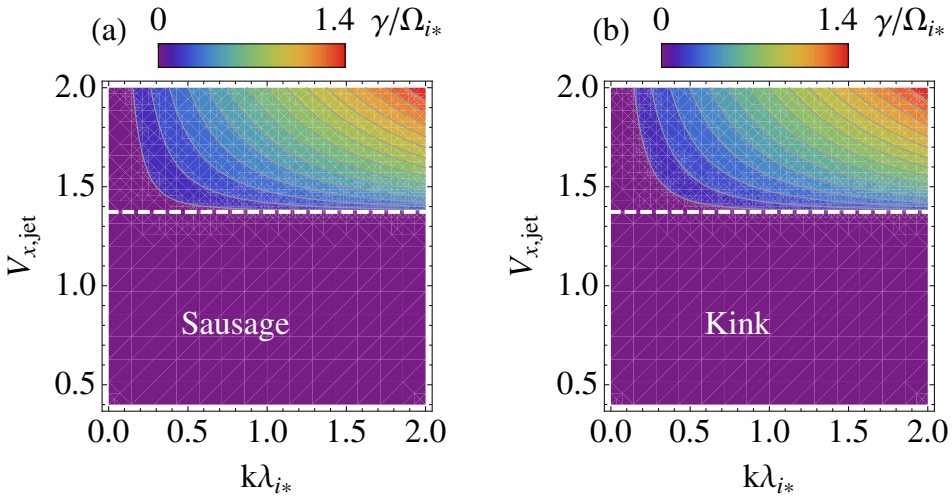

Figure 3.4: Growth rates of the global unstable modes as a function of the wavenumber and the jet speed. The white dashed line corresponds to the threshold of KHI between the jet and the lobe regions. Fig. (a) and (b) are two growing modes of Eq.(3.7).

Figure 3.5 shows the corresponding real and the imaginary parts of these two solutions at $V_{x,\mathrm{jet}} = 1.5$ in Fig. 3.4. Left and right contours respectively show the growth rates for the sausage and the kink modes. These modes become unstable from $k_x\delta_{\mathrm{jet}} \sim \mathcal{O}(0.1)$ and the growth rate increases as k_x becomes larger. For the same reason as the KHI analysis, this is because the model assumed wafer-thin discontinuities in the boundary between lobes and a jet. In more realistic situations, it should have a cut-off, if the boundary has a finite thickness. The propagation speed is almost the same as the phase velocity of the Alfvén wave in lobes, $V_{AL} = 0.9$. Additionally, the phase speed in the kink mode is smaller than that of the sausage mode.

Let us further discuss the eigenvectors of these two modes that was not dis-

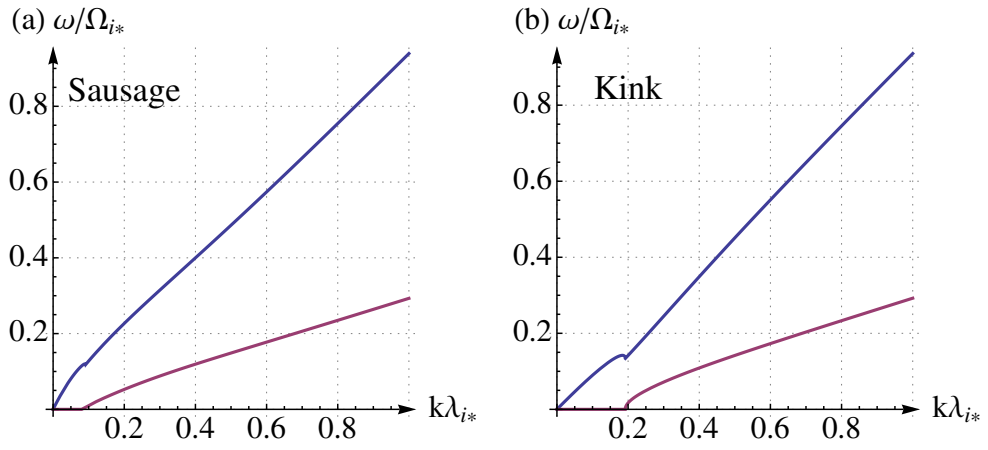

Figure 3.5: Real (blue solid line) and imaginary (red solid line) parts of two solutions of Eq.(3.7) with $\epsilon_{\rm ani,jet} = 1.0$ and $V_{x,\rm jet} = 1.5$.

cussed by [2]. Noting the relation

$$\psi_{\rm jet} = \frac{\xi_{\rm lobe} - \xi_{\rm jet}}{\xi_{\rm lobe} + \xi_{\rm jet}} \phi_{\rm jet} e^{-2k_x \delta_{\rm jet}} \tag{3.8}$$

in Eq.(3.6) gives the eigen functions for the three layer model:

$$\tilde{p}_t(x,y) = p_{\rm amp}(y) e^{i(k_x x - \omega t)}, \tag{3.9}$$

$$\tilde{V}_y(x,y) = V_{\rm amp}(y) e^{i(k_x x - \omega t)}, \tag{3.10}$$

$$\tilde{B}_y(x,y) = B_{\rm amp}(y) e^{i(k_x x - \omega t)}. \tag{3.11}$$

In the following discussions, only the eigen functions in the jet region are shown,

and the amplitude can be calculated as

$$p_{\rm amp}(y) = \frac{\phi_{\rm jet}}{\xi_{\rm lobe}+\xi_{\rm jet}}\left[(\xi_{\rm lobe}+\xi_{\rm jet})\,e^{-k_x y} + (\xi_{\rm lobe}-\xi_{\rm jet})\,e^{k_x\left(y-2\delta_{\rm jet}\right)}\right], \quad (3.12)$$

$$V_{\rm amp}(y) = i\frac{k_x V_0-\omega}{\xi_{\rm jet}}\frac{\partial p_{\rm amp}}{\partial y}, \quad (3.13)$$

$$B_{\rm amp}(y) = i\frac{k_x B_0}{\xi_{\rm jet}}\frac{\partial p_{\rm amp}}{\partial y}. \quad (3.14)$$

Note that $\phi_{\rm jet}$ is given arbitrarily.

Figures 3.6 and 3.7 show the eigen functions calculated using the wavenumber and the frequency of the unstable modes. The wavenumber used here is $k_x = 0.6$, and the amplitude and the two dimensional distribution are shown. The mode shown in Fig.3.6 corresponds to the mode shown in Fig.3.4(a) and 3.5(a), and is the non-resistive streaming sausage mode [55]. On the other hand, the mode in Fig.3.7 is the eigen function of Fig.3.4(b) and 3.5(b), and is the non-resistive streaming kink mode. In each figure, the one-dimensional amplitude ($p_{\rm amp}$, $V_{\rm amp}$, and $B_{\rm amp}$ in the left plots) and the two-dimensional eigen functions (right contour plots) are shown.

The total pressure of the sausage mode has the symmetric pressure perturbation. Comparison of $\tilde{p}$ with $\tilde{B}_y$ suggests that the pressure gradient force, $-\partial_y\tilde{p}$, is absent in the region where the magnetic tension force reaches a maximum (for example at $x \sim -2.5$), and the phase velocity of this mode may be controlled by the magnetic tension force. Thus, the sausage type mode would be an Alfvén type mode. In addition, in the neutral sheet ($y \sim 0$), the total pressure gradient is almost zero.

In the kink mode, it shows the anti-symmetric total pressure perturbation across the neutral sheet. The pressure gradient force is absent in the region where the magnetic tension force becomes the maximum, and the mode is also suggested to be an Alfvénic mode. On the other hand, $-\partial_y\tilde{p}$ is non-zero in the neutral sheet, and the spatial inhomogeneity such as the magnetic field and velocity, whose effects cannot be taken into account in this model, may change the property of this

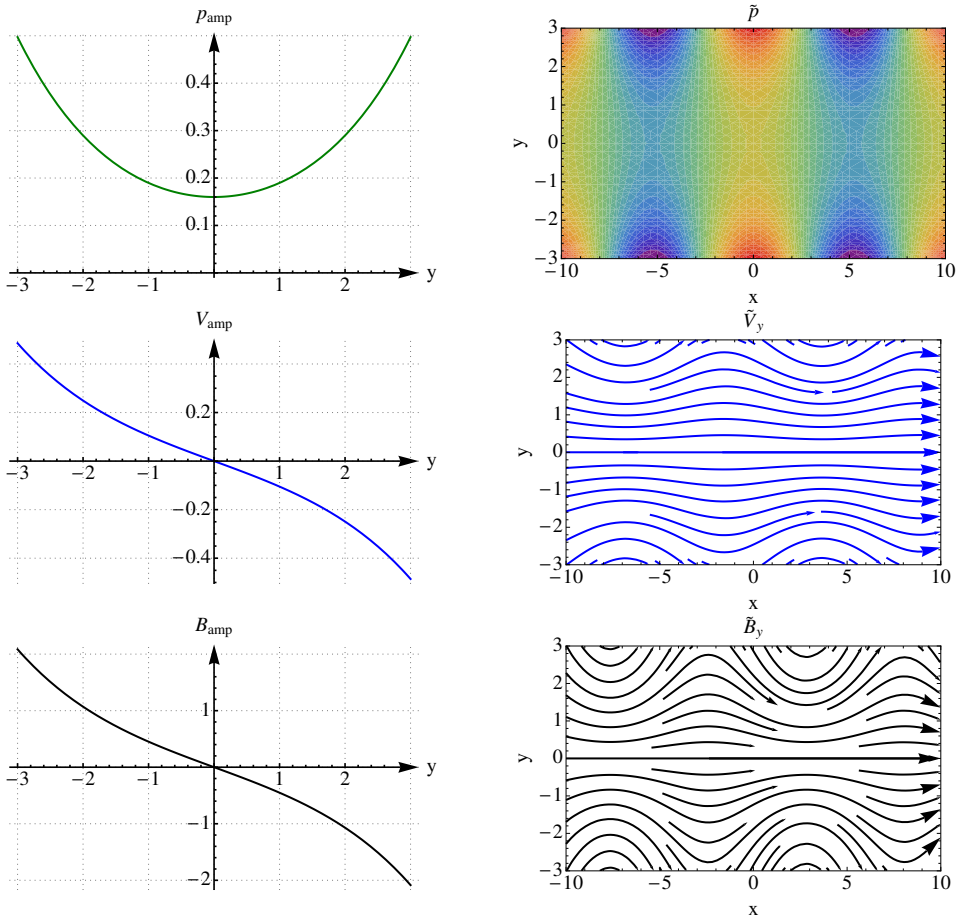

Figure 3.6: From top to bottom, the one- (left panels) and two-dimensional (right panels) eigenfunctions of the total pressure, $\tilde{p}$, the flow velocity, $\tilde{V}_y$, and the magnetic field, $\tilde{B}_y$, in the jet region are shown, respectively. These eigenfunctions are calculated using the solution at $(k, V_{\rm jet}) = (0.6, 1.5)$ in Fig.3.4(a).

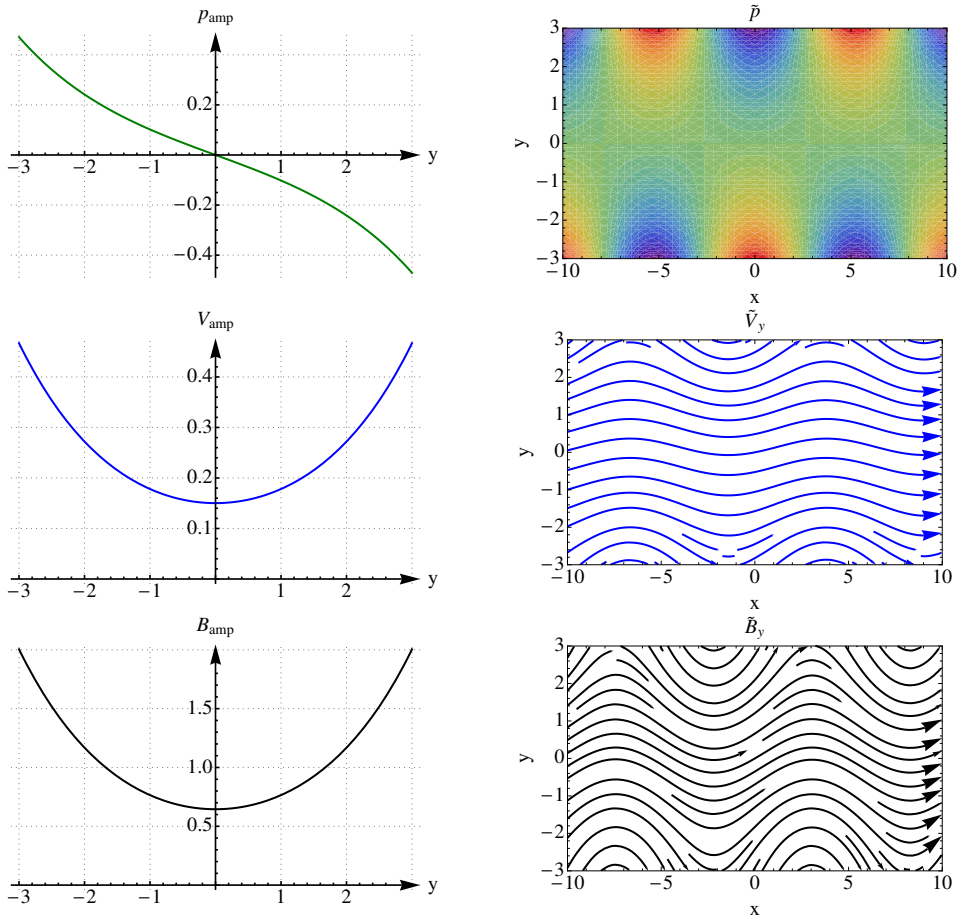

Figure 3.7: From top to bottom, the one- (left panels) and two-dimensional (right panels) eigenfunctions of the total pressure, $\tilde{p}$, the flow velocity, $\tilde{V}_y$, and the magnetic field, $\tilde{B}_y$, in the jet region are shown, respectively. These eigenfunctions are calculated using the solution at $(k, V_{\rm jet}) = (0.6, 1.5)$ in Fig.3.4(b).

unstable mode. This point is discussed in the next section 3.3.

Based on the three layer model, the major points on the properties of unstable modes in the isotropic reconnection jet are:

i Both the sausage and the kink modes are attributed to the interaction of KHIs in two boundaries, and the unstable condition is almost the same as the KHI between the lobe and the jet without three layers.

ii The sausage mode is suggested to be an Alfvén type mode, and the property may not be affected by the magnetic field inhomogeneity.

iii The kink mode would be also an Alfvénic mode. But, the pressure gradient effect is still large in the neutral sheet and the nature may be changed by the non-uniformity such as magnetic field and velocity, which are not taken into account in this model.

Anisotropic pressure effects

The pressure anisotropy effects on the above isotropic discussions are presented here. As shown in Fig.3.3, the anisotropic parameter $\epsilon_{\mathrm{ani,jet}}$ is smaller than unity in reconnection jets, and the parallel pressure exceeds that of perpendicular pressure. Figure 3.8 shows the growth rates of both the sausage (left panels) and the kink (left panels) modes with different jet speed, $V_{0,\mathrm{jet}} = 1.5$, 1.0, and 0.5.

In the slow jet case, $V_{x,\mathrm{jet}} = 0.5$, the growth rates of the kink and sausage modes slightly differ, but in either case strong anisotropy is needed to trigger the instability (stronger than that in the nonlinear hybrid simulation). In the relatively fast jet case, $V_{x,\mathrm{jet}} = 1.5$, where both kink and sausage modes are unstable in the isotropic limit, either of them have broad unstable regions in k_x–ϵ_{ani} space. Since the magnetic tension force in anisotropic plasmas can be expressed as $\epsilon_{\mathrm{ani}} \left(\boldsymbol{B} \cdot \boldsymbol{\nabla}\right) \boldsymbol{B}$, the tension force suppresses KHIs in two boundaries as $p_{\parallel}/p_{\perp}$ (ϵ_{ani}) increases. As the jet speed decreases, the unstable region shrinks and becomes even smaller than the fire-hose marginal condition, $\epsilon_{\mathrm{ani}} = 0$. This would

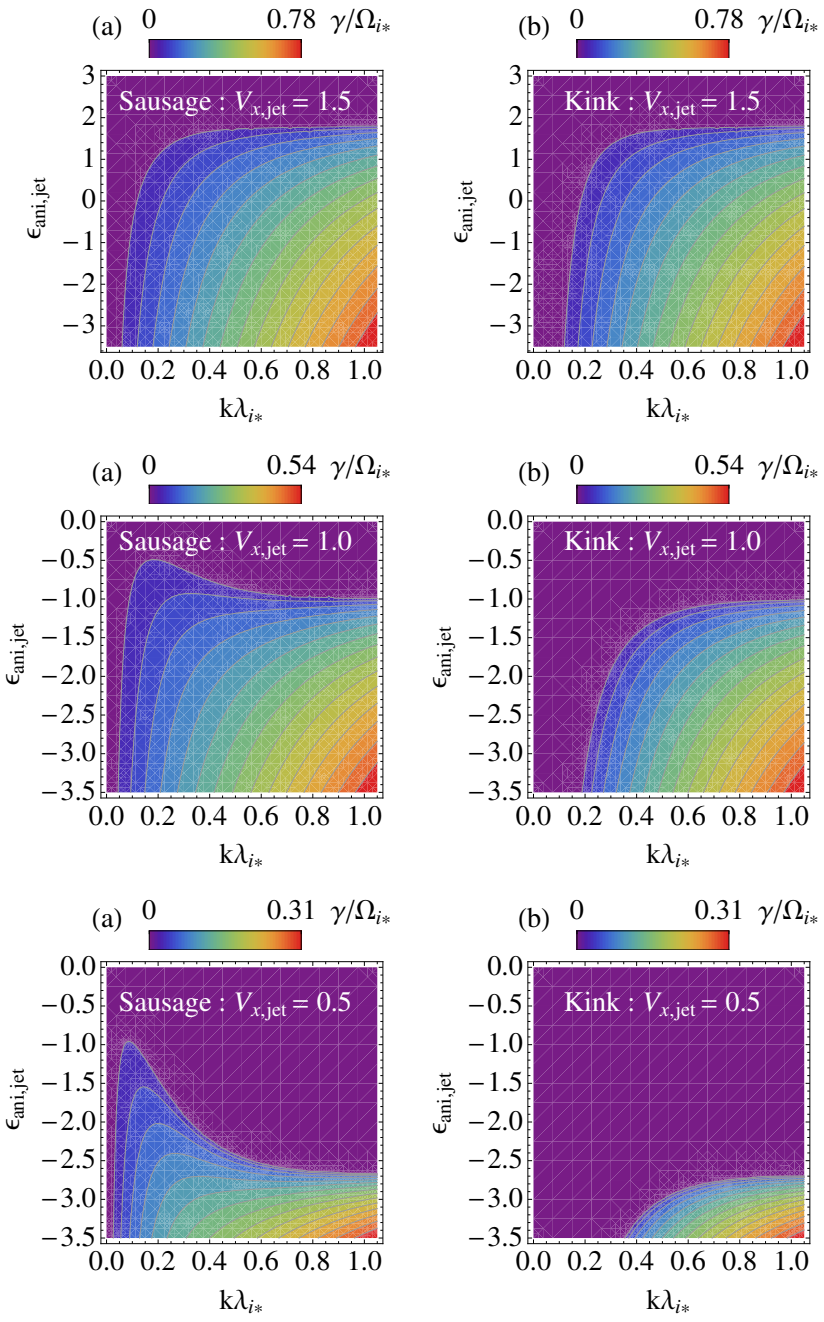

Figure 3.8: Growth rates of the sausage and the kink modes as a function of the anisotropic parameter in jets. From top to bottom, $V_{0,\mathrm{jet}} = 1.5$, 1.0, and 0.5 cases are shown.

be because the centrifugal force by the large parallel pressure, $p_{\parallel}$, in the jet is stabilized by the tension force in the outer isotropic lobes. The sausage mode has a broad unstable range compared to the kink mode, and the sausage mode seems to occur easily in anisotropic reconnection jet as suggested by preceding isotropic studies [55]. However, the above results contradict to the nonlinear particle simulations, where the kink mode dominates in the jet, and we need more detailed analysis to understand the global instability in the reconnection jet.

§ 3.3 Linear eigenvalue analysis for reconnection jets

The property of the unstable modes in reconnection jets are discussed by an incompressible anisotropic MHD eigenvalue analysis. In what follows, the basic equations and setup are presented. Next, the detailed property of unstable modes in the incompressible approximation and the effects of non-uniformity and pressure anisotropy are investigated.

3.3.1 Basic Equations and Setup

In the three layer model presented in Section 3.2, the reason why the kink mode dominates in reconnection jets remains ambiguous. So, in order to discuss the kink and sausage modes in the non-uniformity and the pressure anisotropy without assuming the connectivity used in the three layer model, the eigenmode analysis for the incompressible anisotropic plasma is presented. The instability will be associated with the structural change of the current sheet, and the compressibility is neglected to eliminate the additional elements. The basic equations are

$$\frac{\partial \boldsymbol{V}}{\partial t} = -\boldsymbol{\nabla} \cdot \left[\left(p_\perp + \frac{B^2}{2} \right) \overleftrightarrow{\boldsymbol{I}} + \boldsymbol{V}\boldsymbol{V} - \epsilon_{\rm ani} \boldsymbol{B}\boldsymbol{B} \right] + \nu \boldsymbol{\nabla}^2 \boldsymbol{V}, \tag{3.15}$$

$$\frac{\partial \boldsymbol{B}}{\partial t} = \boldsymbol{\nabla} \times (\boldsymbol{V} \times \boldsymbol{B}) + \eta \boldsymbol{\nabla}^2 \boldsymbol{B}, \tag{3.16}$$

where ν and η are respectively the kinematic viscosity and the magnetic diffusivity. $\overleftrightarrow{\boldsymbol{I}}$ is the unit tensor. (In what follows, we consider the current sheet stability, and the velocity and the magnetic field are respectively normalized by the Alfvén velocity and the magnetic field outside the current sheet. Spatial scale is normalized by the half thickness of the current sheet.) The density is assumed to be constant in space and set to unity. $\epsilon_{\rm ani}$ is an anisotropic parameter and defined by

$$\epsilon_{\rm ani} = 1 - \frac{p_\parallel - p_\perp}{|\boldsymbol{B}|^2}, \tag{3.17}$$

where $p_\parallel$ and $p_\perp$ are respectively pressures parallel and perpendicular to the ambient magnetic field, B. The magnetic field and the velocity are decomposed into zeroth- and first-order components, $\boldsymbol{B} = \boldsymbol{B}_0 + \tilde{\boldsymbol{B}}$ and $\boldsymbol{V} = \boldsymbol{V}_0 + \tilde{\boldsymbol{V}}$, and Eqs.(3.15)–(3.17) are linearized. The first-order fluctuation of the anisotropic parameter is calculated as

$$\tilde{\epsilon}_{\rm ani} = 2\frac{\tilde{B}_x}{B_0}\left(p_{\parallel 0} - p_{\perp 0}\right) - \frac{\tilde{p}_\parallel - \tilde{p}_\perp}{B_0^2} \simeq 2B_0\tilde{B}_x\left(1 - \epsilon_{\rm ani0}\right), \tag{3.18}$$

and the relation $\tilde{p}_\parallel = \tilde{p}_\perp$ is assumed. This comes from the difficulties solving the double adiabatic equations [15] without guide field. (We cannot avoid the singularity at $B = 0$.)

Both $\boldsymbol{B}_0$ and $\boldsymbol{V}_0$ are in the x-direction and have non-uniformity in the y-direction, $\boldsymbol{B}_0 = (B_0(y), 0, 0)$ and $\boldsymbol{V}_0 = (V_0(y), 0, 0)$. In the zeroth field, a Harris current sheet is assumed,

$$B_0(y) = B_{\rm lobe}\tanh\left(\frac{y}{\delta_{\rm harris}}\right), \tag{3.19}$$

where $\delta_{\rm harris}$ is the half thickness of the current sheet. The velocity, V_0, is given by

$$V_0(y) = V_{\rm jet}{\rm sech}^2\left(\frac{y}{\delta_{\rm jet}}\right), \tag{3.20}$$

where $V_{\rm jet}$ is speed at the center of the jet, and $\delta_{\rm jet}$ is half width of the jet.

In the following analysis, the stream function, $\boldsymbol{V} = \boldsymbol{\nabla}\times(\boldsymbol{e}_z\psi_z)$, and the vector potential, $\boldsymbol{B} = \boldsymbol{\nabla}\times(\boldsymbol{e}_z A_z)$, are introduced for the purpose of convenience. Linearized Eqs. (3.15) and (3.16) can be written as

$$\omega\boldsymbol{X}\boldsymbol{x} = \boldsymbol{Y}\boldsymbol{x}, \tag{3.21}$$

where $\boldsymbol{x} = {}^t(\tilde{\psi}_z, \tilde{A}_z)$ (the superscript ^{t} represents the transposed matrix). $\boldsymbol{X}$ and

$\boldsymbol{Y}$ are 2×2 matrix:

$$\boldsymbol{X} = \begin{pmatrix} \partial^2 & 0 \\ 0 & 1 \end{pmatrix}, \tag{3.22}$$

$$\boldsymbol{Y} = \begin{pmatrix} k_x \left(V_0 \partial^2 - \partial_y^2 V_0 \right) + i\nu\partial^4 & k_x \left[\partial_y^2 \Phi - \Phi\partial^2 + \partial_y \left(\Psi \partial_y \right) \right] \\ k_x B_0 & k_x V_0 + i\eta\partial^2 \end{pmatrix}, \tag{3.23}$$

where $\partial^2 = -k_x^2 + \partial_y^2$, $\Phi = \epsilon_{\rm ani0} B_0$, and $\Psi = 2B_0 \left(\epsilon_{\rm ani0} - 1 \right)$. Calculation domain in the y direction is in the range of $-L_y < y < L_y$. At $\pm L_y$, the conducting wall boundary condition is assumed: $\psi_z = 0$, $A_z = 0$, $\partial_y^2 \psi_z = 0$, and $\partial_y^2 A_z = 0$ ($B_y = 0$, $V_y = 0$, $\partial_y B_x = 0$, $\partial_y B_z = 0$, $\partial_y V_x = 0$, and $\partial_y V_z = 0$), where the non-resistive Ohm's law is used.

The derivative, ∂_y, is a second-order accurate central-difference scheme. The simulation parameters used in the following results are summarized in Table 3.2. The magnetic Reynolds number and the Reynolds number are defined by $R_m = \delta_{\rm harris} V_A / \eta$ and $R_e = \delta_{\rm harris} V_A / \nu$, respectively. V_A is the Alfvén velocity outside the current sheet and $V_A = 1$. The Reynolds number and the half thickness of the discontinuity are fixed to $R_e = 1.0 \times 10^3$.

Table 3.2: Parameters used for the linear eigenmode analysis

Figure	$k_x\delta_{\rm harris}$	$V_{\rm jet}/V_A$	$\epsilon_{\rm jet}$	R_m	$\delta_{\rm harris}/L_y$	$\delta_{\rm jet}/\delta_{\rm harris}$	L_y/Δ_y
Fig. 3.9	0.0–2.5	0.0–2.2	1.0	5.0×10^2	0.1	1.0	500
Fig. 3.10	0.0–2.5	0.0 / 1.5 / 2.2	1.0	$(2.5 / 5.0 / 7.5) \times 10^2$	0.1	1.0	500
Fig. 3.11	0.3 / 0.5	0.0 / 2.2	1.0	5.0×10^2	0.1	1.0	500
Fig. 3.12	0.5	2.5	1.0	5.0×10^2	0.1	1.0	500
Fig. 3.14	–	0.0 / 2.2	0.4–1.1	5.0×10^2	0.1	1.0	500
Fig. 3.15	–	2.2	1.0	5.0×10^2	0.1	0.5–1.5	500
Fig. 3.16	–	2.2	0.4–1.1	5.0×10^2	0.1	0.5 / 1.5	500

3.3.2 Results and Discussion

Basic unstable modes in an incompressible streaming current sheet

First of all, basic features of the unstable modes in an incompressible streaming current sheet are reviewed for convenience. Note that these unstable modes themselves have been already shown by preceding studies with isotropic plasmas [55]. The detailed property and the anisotropy effects are investigated in the next subsections to explain the instability in the reconnection jet. Here, half width of the jet is always set to $\delta_{\rm jet} = \delta_{\rm harris}$. Figure 3.9 shows the growth rate, γ, of the most unstable modes at $R_m = 5.0 \times 10^2$ as a function of wavenumber and jet speed with both linear (left contour plot) and logarithmic (right contour plot) scales. The growth rate is normalized by the Alfvén transit time, $\tau_A = \delta_{\rm harris}/V_A$. And in Fig.3.10, all the unstable modes are shown along the cross-sections, $V_{\rm jet}/V_A = 0.0$, 1.5, and 2.2, with different magnetic Reynolds numbers ($R_m = 250$; dashed line, $R_m = 750$; dotted line).

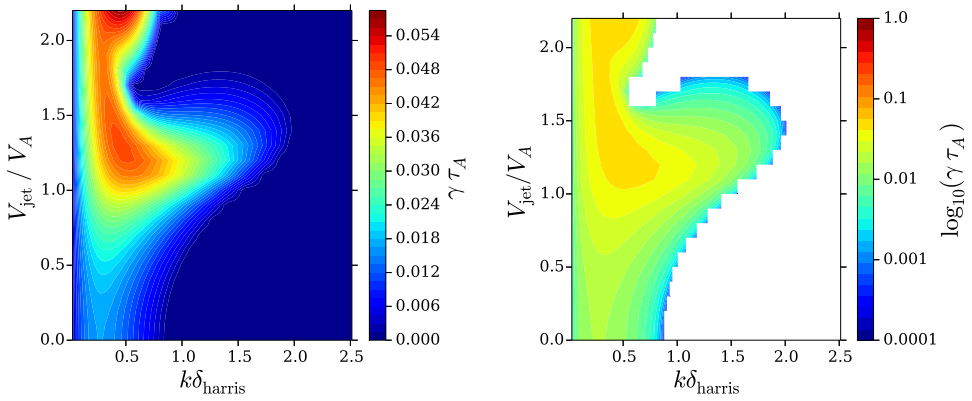

Figure 3.9: The growth rate of the most unstable mode in the streaming current sheet as a function of k_x and $V_{\rm jet}$. The left and right panels are respectively shown in linear and logarithmic scales, and the region where $\gamma = 0$ is masked in the right panel. The jet width $\delta_{\rm jet}$ is equivalent to $\delta_{\rm harris}$, and the magnetic Reynolds number is $R_m = 5.0 \times 10^2$.

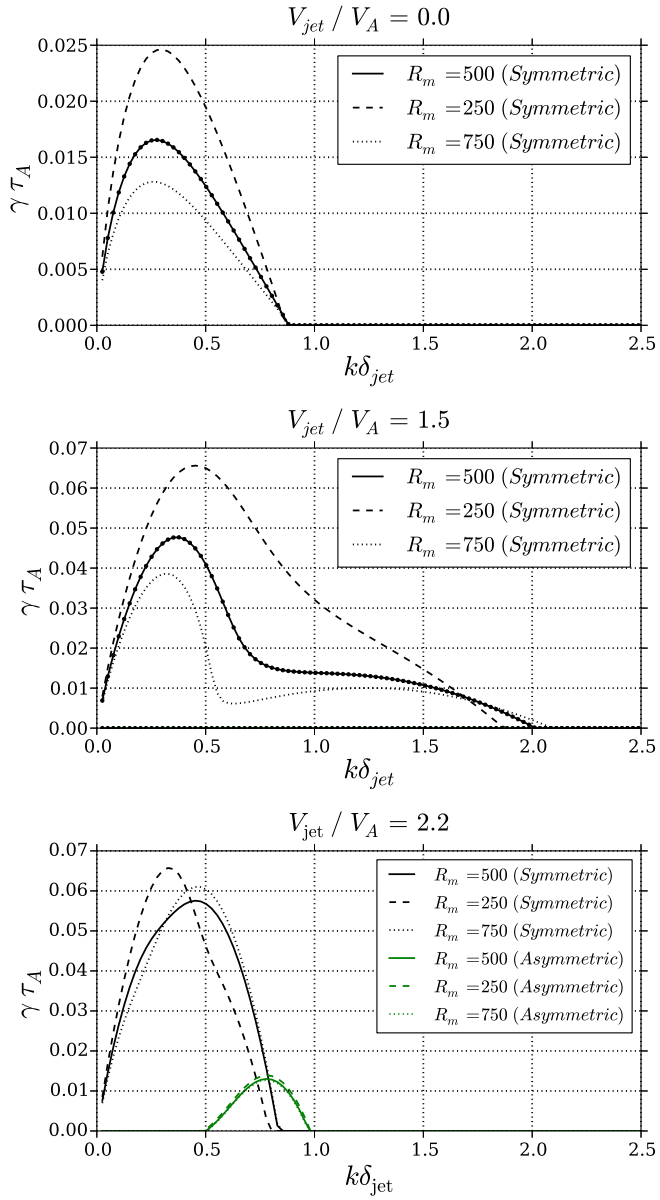

Figure 3.10: The growth rate at $V_{\rm jet}/V_A = 0.0$, 1.5, and 2.2. Solid black and solid green lines respectively shows symmetric and anti-symmetric modes for the $R_m = 5.0 \times 10^2$ case. Dashed and dotted lines show the growth rates for $R_m = 2.5 \times 10^2$ and 7.5×10^2 cases, respectively.

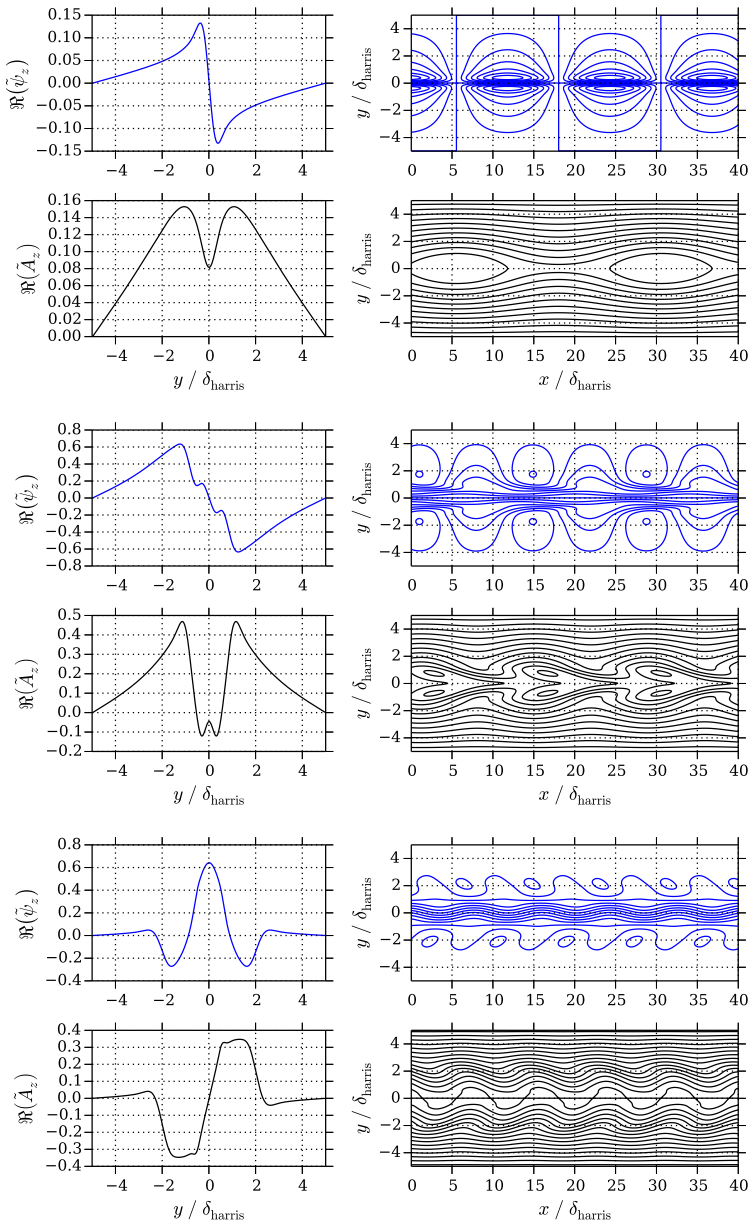

Figure 3.11: The eigenvectors of the tearing mode at $V_{\mathrm{jet}}/V_A = 0$ and $k_x\delta_{\mathrm{harris}} = 0.25$ (top four panels), non-resistive sausage mode at $V_{\mathrm{jet}}/V_A = 2.2$ and $k_x\delta_{\mathrm{harris}} = 0.45$ (middle four panels), and non-resistive kink mode at $V_{\mathrm{jet}}/V_A = 2.2$ and $k_x\delta_{\mathrm{harris}} = 0.75$. Left plots show real parts of $\tilde{\psi}_z$ and $\tilde{A}_z$, and right contours show stream (blue lines) and magnetic field lines (black lines).

In the case of $V_{\rm jet}/V_A = 0.0$, it shows a basic resistive tearing mode (symmetric mode) in $k_x\delta_{\rm harris} < 1$, and the growth rate properly follows the FKR $R_m^{-3/5}$ law. The upper four panels of Fig.3.11 show eigenfunctions for the tearing mode for $V_{\rm jet}/V_A = 0.0$ and $k_x\delta_{\rm harris} = 0.25$. The left plots show the real part of $\tilde{\psi}_z$ and $\tilde{A}_z$, and the right contours show the real part of $\tilde{\psi}_z e^{ik_x x}$ and $\tilde{A}_z e^{ik_x x}$ (they correspond to stream and magnetic field lines, respectively). As $V_{\rm jet}$ increases (see the $V_{\rm jet} = 1.5$ case), the symmetric mode shifted to large k_x and the maximum growth rate increases, which has been reported by [83, 55]. In longer wavelengths, the symmetric unstable mode shows resistive nature, while non-resistive in shorter wavelengths. In the faster jet case (see the $V_{\rm jet} = 2.2$ case), both the wavelength and the growth rate of the symmetric mode increase, and it ceases to depend on the magnetic Reynolds number. The eigenfunctions with $V_{\rm jet}/V_A = 2.2$ and $k_x\delta_{\rm harris} = 0.45$ are shown in the middle four panels of Fig.3.11. This mode symmetrically grows and shows a wedge shaped structure. Additionally, a anti-symmetric mode becomes unstable beyond $V_{\rm jet}/V_A \sim 2$. This mode does not couple with a resistive mode and is almost independent of R_m as shown by [55]. The eigenfunctions are shown in the bottom four panels of Fig.3.11, and both flow and magnetic field lines show the kinking structure.

Properties of unstable modes

To discuss the signatures of sausage and kink modes in nonuniform system, let us further consider the force balance between the pressure gradient and the magnetic tension terms. The y-component of the first-order linearized equation of momentum can be written as

$$\frac{d\tilde{V}_y}{dt} = \underbrace{-\partial_y\left(\tilde{p}_m\right)}_{\tilde{f}_p} + \underbrace{\epsilon_0\left(\boldsymbol{B}_0\cdot\boldsymbol{\nabla}\right)\tilde{B}_y}_{\tilde{f}_t}, \tag{3.24}$$

where $\tilde{p}_m = B_0\tilde{B}_x$ is the magnetic pressure. Figure 3.12 shows the real part of eigenfunctions of $\tilde{p}_m$, $\tilde{f}_p$, and $\tilde{f}_t$ for the sausage (upper six panels) and the kink

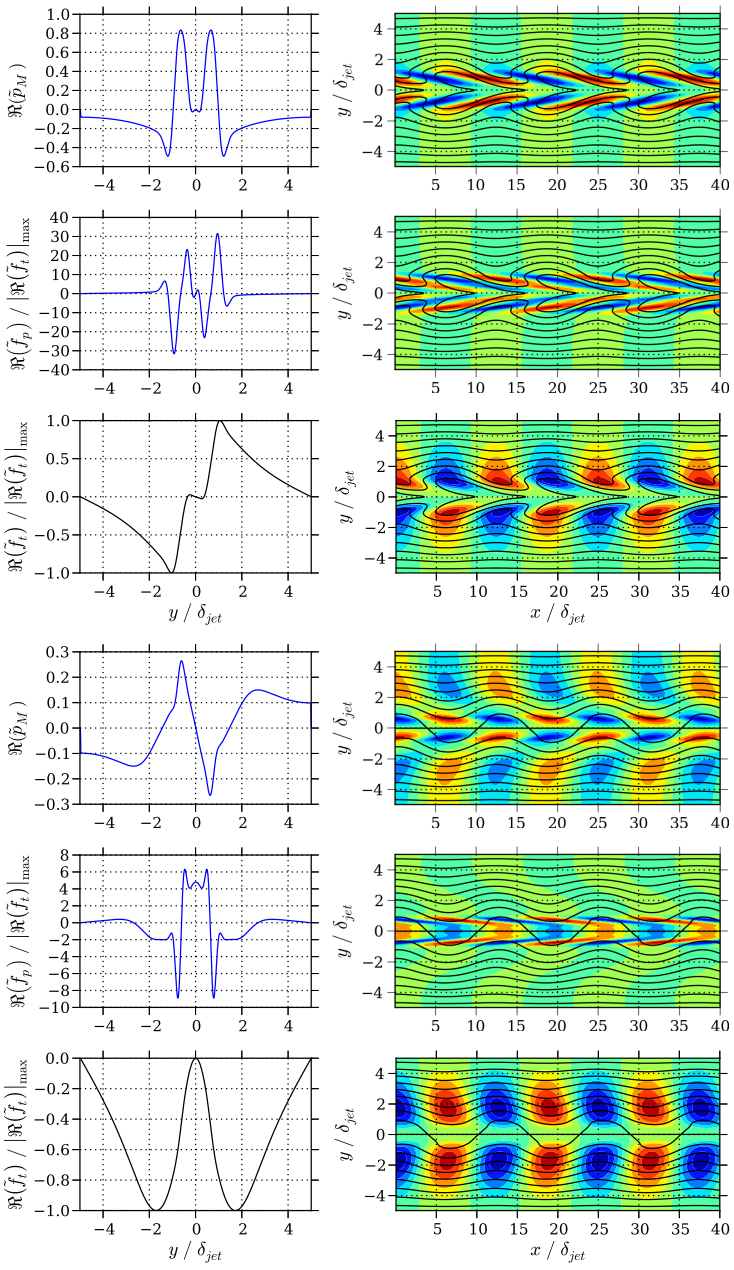

Figure 3.12: The real part of $\tilde{p}_m$, $\tilde{f}_p$, and $\tilde{f}_t$ in one- (left plots) and two-dimensions (right contours) in the case of $V_{\rm jet}/V_A = 2.5$ and $k_x\delta_{\rm harris} = 0.50$. The black solid lines are corresponding magnetic field lines. Upper panels show the sausage mode, and the lower panels show the kink mode.

(bottom six panels) modes. In the right contour plots, the magnetic field lines are overlaid for reference. For the purpose of comparison, $\Re(\tilde{f}_p)$ is normalized by the maximum value in tension force. In either side of the jet, fluctuations are produced by KHI and the magnetic field in the jet are stretched and relaxed as illustrated in Fig.3.13 (or consider the x-component of the induction equation). Then, the globally produced magnetic pressure gradient force in the y-direction, f_p, begins to couple with Alfvén modes.

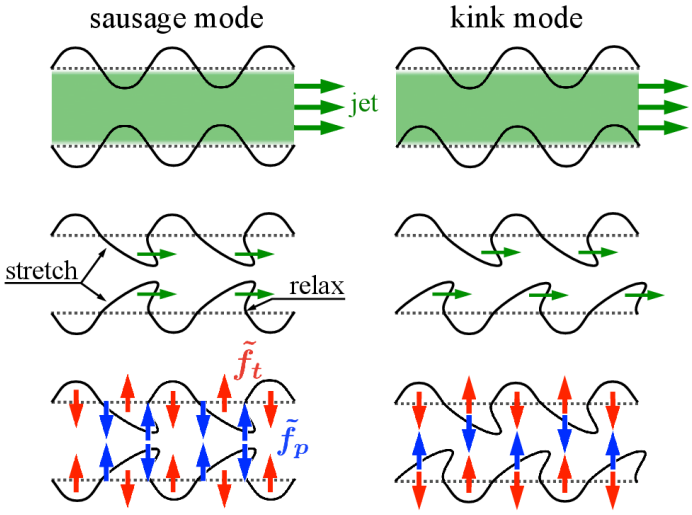

Figure 3.13: A schematic view of sausage (left panels) and kink (right panels) modes. The black lines represent magnetic field lines. The red and the blue arrows respectively stand for $\tilde{f}_t$ and $\tilde{f}_p$ in Eq.(3.24).

In the sausage mode case, the perturbation of the magnetic field pressure symmetrically appears across $y = 0$, and there is no magnetic pressure gradient force near the neutral sheet. Also, the gradient force appears in the wave node as shown in the bottom panel of Fig.3.13 and the mean restoring force is not changed drastically. This property is almost the same that was suggested by the three layer model, and the sausage mode is suggested to be a simple Alfvén type mode.

On the other hand, the kink mode is sustained not only by the magnetic tension

force but also the magnetic pressure gradient force near the neutral sheet. The gradient force appears in the anti-node and is in the direction which weaken the restoring tension force. Thus, the kink mode shows a slow Alfvén type behavior and the unstable property would be affected by the magnetic field strength or pressure anisotropy in contrast to the three layer model.

Pressure anisotropy effects

For the streaming current sheet stability, the pressure anisotropy is an important factor to suppress and enhance the instability. The left two panels of Fig.3.14 show the maximum growth rate and the corresponding wavenumber for the tearing mode as a function of the anisotropic parameter, $\epsilon_{\rm ani}$. The jet speed is set to $V_{\rm jet}/V_A = 0$. The growth rate of the tearing mode decreases as the parallel pressure increases, $\epsilon_{\rm ani} < 1$, and goes to zero below $\epsilon_{\rm ani} = 0.4$.

The right two panels of Fig.3.14 show the maximum growth rates and the corresponding wavenumbers for the sausage (black) and kink (green) modes. The jet speed is $V_{\rm jet}/V_A = 2.2$. The growth rate of the sausage mode is $\gamma_{\rm max}\tau_A \sim 0.06$–$0.07$ independent of the pressure anisotropy. On the other hand, the growth of the kink mode increases as the pressure anisotropy, $p_\parallel/p_\perp$, increases. This behavior is related to the slow Alfvén type property of the kink mode. In the kink mode, the transverse force, $d\tilde{V}_y/dy$, is sustained by both magnetic tension force and global magnetic pressure gradient force. Consider y-component of the equation of motion and the induction equation:

$$\partial_t \tilde{V}_y + V_0 \partial_x \tilde{V}_y = -\partial_y (B_0 \partial_y \tilde{A}_z) - \epsilon_0 B_0 \partial_x^2 \tilde{A}_z, \tag{3.25}$$

$$\partial_t \tilde{A}_z = \partial_x V_0 \tilde{A}_z - B_0 \tilde{V}_y. \tag{3.26}$$

For the kink mode case, the first term of Eq.(3.25) cannot be neglected. Thus, near the current sheet, letting $\partial_y \to \delta^{-1} (= \delta_{\rm jet}^{-1} = \delta_{\rm harris}^{-1})$, $\partial_t \to -i\omega$, $\partial_x \to ik_x$, and

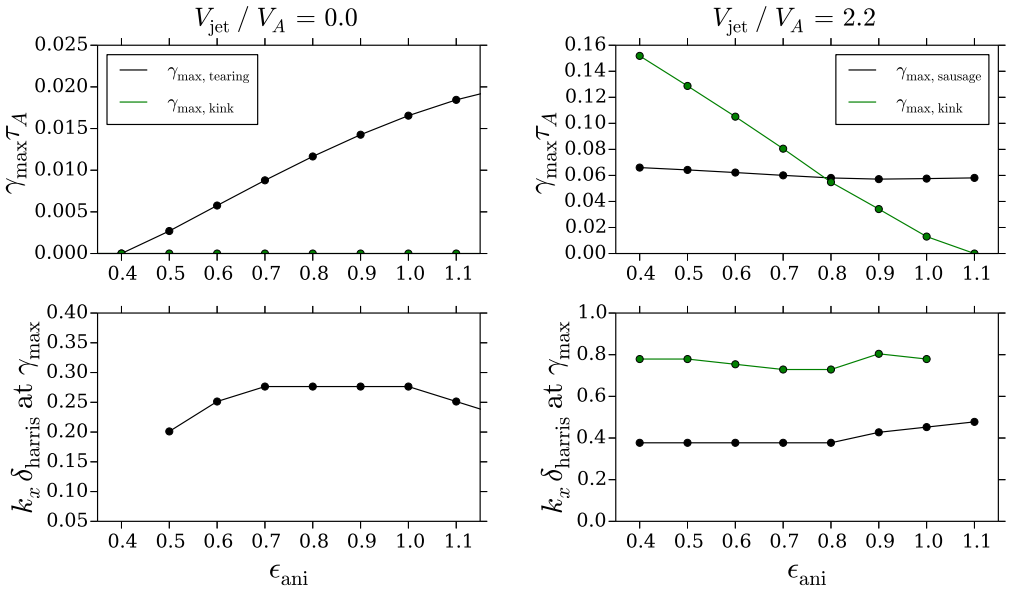

Figure 3.14: The maximum growth rates and the corresponding wave numbers of the resistive tearing mode with $V_{\rm jet} = 0.0$ (left plots), the non-resistive kink mode with $V_{\rm jet} = 2.2$ (the right green line), and the non-resistive sausage mode with $V_{\rm jet} = 2.2$ (the right black line) as a function of the anisotropic parameter $\epsilon_{\rm ani}$.

eliminating $\tilde{A}_z$ from Eq.(3.25) gives

$$\left[(\omega - k_x V_0)^2 - V_A^2 \left(\epsilon_0 k_x^2 - \frac{1}{\delta^2}\right)\right] \tilde{V}_y = 0. \tag{3.27}$$

Then, the solution is

$$\omega = k_x V_0 \pm V_A \sqrt{\epsilon_0 k_x^2 - \frac{1}{\delta^2}}. \tag{3.28}$$

This equation means that the magnetic pressure gradient force produced in the jet reduces the threshold for the fire-hose instability (FHI), $\epsilon_0 < 0$, and the reduced unstable condition becomes $k_x\delta < 1/\sqrt{\epsilon_0}$. Hence the growth rate of the global kink mode is determined by the coupling between KHI and the reduced FHI. On the other hand, in the sausage mode case, the pressure gradient force can be neglected and the solution may be expressed as, $\omega = k_x V_0 \pm k_x V_A \sqrt{\epsilon_0}$. Thus, the sausage mode is a coupling mode of KHI and the pure FHI. In this way, only the growth rate for the kink mode increases below the pure FHI marginal limit, i.e., $\epsilon_0 > 0$. The difference comes from the global magnetic pressure gradient force. Since the non-uniformity in a jet was not taken into account correctly in the three layer model, both the sausage and kink modes would show the similar response to the pressure anisotropy.

Width of the jet and the current sheet

The above discussions were limited in the case of $\delta_{\rm jet}/\delta_{\rm harris} = 1$, but the ratio, $\delta_{\rm jet}/\delta_{\rm harris}$ is also an important factor to suppress and enhance the instability. Figure 3.15 shows the maximum growth rate for the sausage and the kink modes as a function of $\delta_{\rm jet}/\delta_{\rm harris}$. As $\delta_{\rm jet}/\delta_{\rm harris}$ decreases, the growth rates of both the sausage and kink modes increases. In particular, the kink mode is much more sensitive to the ratio, $\delta_{\rm jet}/\delta_{\rm harris}$. In the case of $\delta_{\rm jet}/\delta_{\rm harris} < 1$, because both magnetic pressure gradient force and the magnetic tension force decreases, it is natural that the kink mode dominates as the hydrodynamic case [6]. (Note that in the mag-

netized jet with anisotropic plasmas, only the magnetic tension force decreases as $p_{\parallel}/p_{\perp}$ becomes large.)

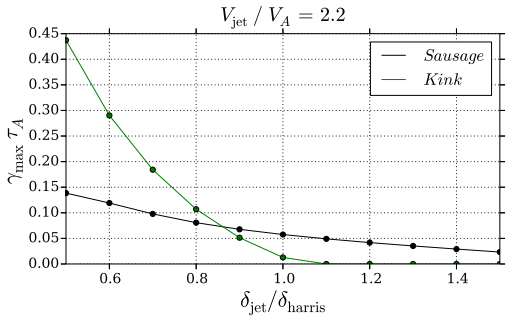

Figure 3.15: The maximum growth rates of the sausage (black line) and kink (green line) modes, depending on $\delta_{\rm jet}/\delta_{\rm harris}$.

Next, let us discuss the anisotropy effect in both narrow ($\delta_{\rm jet}/\delta_{\rm harris} < 1$) and wide jets ($\delta_{\rm jet}/\delta_{\rm harris} > 1$). Figure 3.16 shows the maximum growth rates of the kink (green line) and the sausage (black line) modes as a function of the anisotropic parameter, $\epsilon_{\rm ani}$. In the narrow jet case (left panel), where the magnetic field is weak, both the kink and the sausage modes do not show strong dependence on the anisotropy compared to the case of $\delta_{\rm jet}/\delta_{\rm harris} = 1$ (see the upper right panel in Fig.3.14). This is simply because the unstable modes are in the hydrodynamic limit and the magnetic field is less important. On the other hand, in the wide jet case (right panel), where magnetic field is important, the growth rate of the kink mode strongly depends on the anisotropy. This suggests that KHI could couple with FHI even in the case of $\delta_{\rm jet} \neq \delta_{\rm harris}$ as discussed in the case of $\delta_{\rm jet}/\delta_{\rm harris} = 1$.

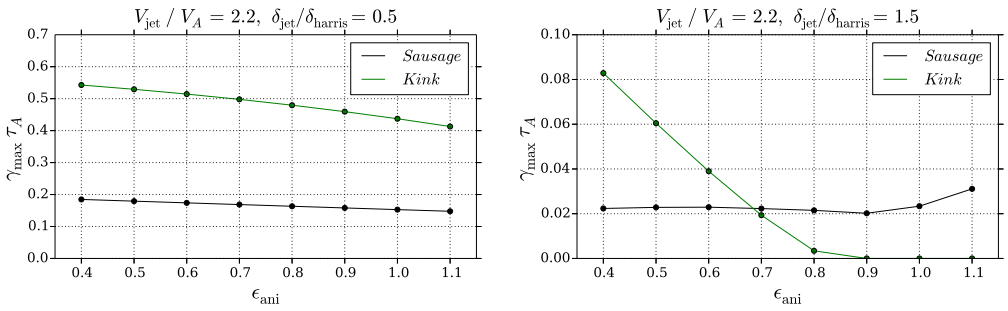

Figure 3.16: The maximum growth rates of the sausage (black line) and kink (green line) modes for the narrow ($\delta_{\rm jet}/\delta_{\rm harris} = 0.5$; left panel) and wide jets ($\delta_{\rm jet}/\delta_{\rm harris} = 1.5$; right panel) depending on the anisotropic parameter, $\epsilon_{\rm ani}$.

§ 3.4 Summary

In the previous Chapter 2, we showed the nonlinear development of reconnection jets, and the ingredients that could generate and suppress Alfvénic fluctuations were discussed by the local viewpoint. However, the reconnection jet is non-uniform and the globally oscillating (kinking) mode could not be explained by only the local analysis. In this Chapter 3, we discussed such global unstable modes by the linear eigenmode analysis that includes both non-uniformity and pressure anisotropy effects. In the preceding studies with isotropic pressure plasmas, it has been suggested that the kink mode may be unimportant and the tearing and sausage modes were believed to dominate in the magnetized plasma jet. But in the ion-scale reconnection jet, both non-uniformity and the pressure anisotropy develop owing to the ion kinetic effects, and the previous discussion may not necessarily be applicable to the reconnection jet.

So, we first considered the kink and sausage modes based on the simple three layer model by [2], but we could not explain the reason why only the kink mode dominates in reconnection jets. Then, we investigated a streaming current sheet stability in the anisotropic plasmas by the eigenmode analysis, and aimed to give a clear understanding of the unstable mode in reconnection jets. Important issues

added to the non-local growing modes are mainly following points:

- The sausage mode is suggested to be an Alfvén type mode, and the unstable condition may be understood by the combination of KHI and the pure FHI in a magnetized jet with anisotropic plasmas.

- The kink mode is suggested to be a slow Alfvén type mode, and it is sensitive to both the pressure anisotropy and the ratio, $\delta_{\rm jet}/\delta_{\rm harris}$. In the case of $\delta_{\rm jet} = \delta_{\rm harris}$ with anisotropic plasmas $p_{\parallel} > p_{\perp}$, the growth rate becomes much larger than that of the isotropic case. Near the current sheet, the pure FHI threshold is largely modified by the magnetic pressure gradient force. Because the unstable nature of the kink mode is determined by the combination of KHI and the modified FHI, the kink mode has enough growth rate in the range of $0 < \epsilon_{\rm ani} < 1$. The relation between the jet and the current sheet widths is also an important factor for the growth of the kink mode. In the case of $\delta_{\rm jet}/\delta_{\rm harris} < 1$, the jet approaches hydrodynamic case and the kink mode dominates. In the case of $\delta_{\rm jet}/\delta_{\rm harris} > 1$, KHI could couple with the modified FHI as in the case of $\delta_{\rm jet} = \delta_{\rm harris}$, and the kink mode dominates in the jet with anisotropic pressure, $p_{\parallel} > p_{\perp}$.

In the scale of $L_R/\lambda_i \sim 10^{1-2}$, ion kinetic effects produce pressure anisotropy, $p_{\parallel}/p_{\perp} > 1$, and the kink mode is suggested to dominate compared to other symmetric modes from the above linear analysis [1]. Also, because the kink mode is an MHD mode, the free energy source is the bulk momentum like a Kelvin-Helmholtz instability. On the other hand, the wave excitation and damping in the PSBL discussed in Chapter 2 occurs by the non-uniformity of velocity space, $f_i(v_{i,x}, v_{i,y})$, and the free energy source is different from the MHD mode. Therefore, the unstable reconnection dynamics may not be described by one element, but would be a complex system. As a result of such competing processes (instabilities), the reconnection jet will develop into turbulent state.

[1] Even in the nonlinear phase, the saturation level of the kink mode is much larger than that of other modes, if the pressure anisotropy is enough large, $\epsilon_{\rm ani} < 0.5$. This issue is shown by nonlinear hybrid simulations in Appendix A.

CHAPTER 4

Effects of fully-developed MHD turbulence on the macroscopic reconnection dynamics

This Chapter focuses on the role of MHD turbulence on the macro-scale reconnection dynamics. The fully-developed MHD turbulence is assumed in the initial current sheet, and the macroscopic effects are discussed from a Reynolds-averaged MHD model. The model calculation suggests that the initial Harris current sheet could develop in three ways, depending on the strength of turbulence: laminar reconnection, turbulent reconnection, and turbulent diffusion. The turbulent reconnection explosively converts the magnetic field energy into both kinetic and thermal energy of plasmas, and generates open fast reconnection jets. In the turbulent magnetic reconnection, turbulent quantities such as turbulent energy and cross-helicity form in the diffusion region through the interaction between mean and turbulent fields. A localized distribution of turbulent energy near the neutral point enhances the effective magnetic field diffusion and leads to efficient reconnection rate. Also, cross-helicity effects suppress the turbulent diffusion in the downstream jet and contribute to localization of the diffusion region and further enhancement of the reconnection rate. This turbulent-mediated process would give one of the important ways to understand macro-scale reconnection dynamics [41].

§ 4.1 Introduction

This study focuses on the relationship between magnetic reconnection and MHD turbulence in a macroscopic scale. In particular, it is based on the viewpoint how the macro-scale reconnection dynamics are modified in the presence of turbulence. In this section, a turbulence model, which is an important concept of this Chapter, is introduced.

Turbulence model

In the area of hydrodynamic turbulence studies, there are mainly three ways to deal with turbulent phenomena: the direct numerical simulation (DNS), the large eddy simulations (LES), and Reynolds-averaged Navier–Stokes (RANS) model. This study adopted the third Reynolds-averaged model, and only DNS and RANS are introduced. Figure 4.1 schematically shows their differences. DNS directly solves the Navier–Stokes equation without any approximation, and aims to resolve at all scales ranging from large phenomenological to small dissipation scales. This method guarantees high-accuracy of the resolvable turbulent motion, while fails to describe the small turbulent motion near the grid scale. To investigate the role of fully-developed turbulence in a high magnetic Reynolds number, this study adopted the concept of the Reynolds-averaged simulation model [53]. This model is based on the concept of Reynolds decomposition, which decomposes a quantity into mean and fluctuating variables, and aims to describe properties of turbulence (such as the energy cascade and the dissipation rate). In the following passage, the concept of Reynolds averaging and how to model microscopic turbulent effects are introduced in association with the method of this study.

Reynolds decomposition and mean field equations

In the mean field approach, the physical quantities such as velocity $\boldsymbol{v}$ and magnetic field $\boldsymbol{b}$ are decomposed into mean and fluctuating turbulent parts, and they are considered separately; $\boldsymbol{v} = \boldsymbol{V} + \boldsymbol{v}'$ and $\boldsymbol{b} = \boldsymbol{B} + \boldsymbol{b}'$, where capital letters stand

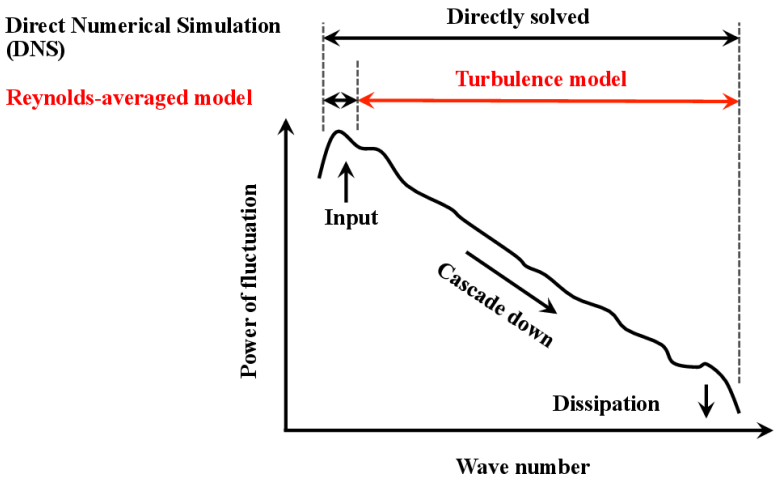

Figure 4.1: A schematic view for turbulence simulation models: direct numerical simulation (DNS) and Reynolds-averaged model.

for mean field. Here, the fluctuating part is not necessarily small compared to mean field, but vanishes after ensemble averaging; $\langle \boldsymbol{v}' \rangle \ll \left\langle (\boldsymbol{v}')^2 \right\rangle^{1/2}$, where the brackets $\langle\ \rangle$ stand for ensemble averaging.

This study starts with incompressible MHD equations to introduce a Reynolds-averaged turbulence model,

$$\frac{\partial \boldsymbol{v}}{\partial t} = -\boldsymbol{\nabla} \cdot \left(\boldsymbol{v}\boldsymbol{v} - \boldsymbol{b}\boldsymbol{b} + p_t \overleftrightarrow{\boldsymbol{I}} \right) + \nu \triangle \boldsymbol{v}, \tag{4.1}$$

$$\frac{\partial \boldsymbol{b}}{\partial t} = \boldsymbol{\nabla} \times \left(\boldsymbol{v} \times \boldsymbol{b} - \eta \boldsymbol{j} \right), \tag{4.2}$$

where $p_t = p + b^2/2$ is total pressure and $\overleftrightarrow{\boldsymbol{I}}$ is an unit tensor. Decomposing variables into mean and turbulent parts and taking ensemble averaging give following mean field equations:

$$\frac{\partial V_i}{\partial t} = -\frac{\partial}{\partial x_j} \left(V_i V_j - B_i B_j + P_t I_{ij} \right) - \frac{\partial R_{ij}}{\partial x_j} + \nu \frac{\partial^2 V_i}{\partial x_j^2}, \tag{4.3}$$

$$\frac{\partial B_i}{\partial t} = \varepsilon_{ijk} \frac{\partial}{\partial x_j} \left[\varepsilon_{klm} \left(V_l B_m - \eta \frac{\partial B_m}{\partial x_l} \right) + E_{M,k} \right], \tag{4.4}$$

where

$$R_{ij} = \left\langle v_i' v_j' - b_i' b_j' \right\rangle, \tag{4.5}$$

$$E_{M,k} = \varepsilon_{klm} \left\langle v_l' b_m' \right\rangle, \tag{4.6}$$

are respectively Reynolds stress and electromotive force, which reflect the information of turbulence and could contribute to the macroscopic (mean field) dynamics. The most important part of modeling turbulence is how to model these correlation terms. Reynolds stress, $\langle \boldsymbol{v}'\boldsymbol{v}' - \boldsymbol{b}'\boldsymbol{b}' \rangle$, could be assumed to be small in magnetic reconnection, and is neglected in the present study as a first step. Then, let us begin with how to model the electromotive force, $\langle \boldsymbol{v}' \times \boldsymbol{b}' \rangle$.

Modeling of electromotive force for MHD turbulence

The simplest way to evaluating the electromotive force, $\langle \boldsymbol{v}' \times \boldsymbol{b}' \rangle$, is so called *first-order smoothing approximation* [67] (may be regarded as quasi-linear analysis). Since both total and mean field equations are given, subtracting mean field from total field equations gives following equations for turbulent fields:

$$\frac{\partial v_i'}{\partial t} = -\frac{\partial}{\partial x_j}\left(v_i' V_j + V_i v_j' - b_i' B_j - B_i b_j' + v_i' v_j' - b_i' b_j' + R_{ij}\right) + \nu \frac{\partial^2 v_i'}{\partial x_j^2} \tag{4.7}$$

$$\frac{\partial b_i'}{\partial t} = \varepsilon_{ijk} \frac{\partial}{\partial x_j}\left[\varepsilon_{klm}\left(v_l' B_m + V_l b_m' + v_l' b_m' - \eta \frac{\partial b_m'}{\partial x_l}\right) - E_{M,k}\right] \tag{4.8}$$

First-order smoothing approximation usually makes some assumptions. For example in Eq.(4.8), fluctuation of magnetic field b' is assumed to be smaller than the mean magnetic field, B, and the term $\varepsilon_{klm} v_l' b_m' - E_{M,k}$ is dropped. (Note that this assumption may restrict discussions for the low R_m case.)

First, let us consider the case that the mean velocity, V, can be neglected. In this case, the equation of the fluctuating magnetic field becomes

$$\frac{\partial b_i'}{\partial t} \sim \varepsilon_{ijk} \frac{\partial}{\partial x_j}\left(\varepsilon_{klm} v_l' B_m\right) = B_j \frac{\partial v_i'}{\partial x_j} - v_j' \frac{\partial B_i}{\partial x_j}. \tag{4.9}$$

Integrating this in time gives

$$b_i' = \int_{-\infty}^{t} dt' \left(B_j \frac{\partial v_i'}{\partial x_j} - v_j' \frac{\partial B_i}{\partial x_j}\right), \tag{4.10}$$

and substituting this into (4.6) gives

$$\varepsilon_{ijk} \left\langle v_j' b_k' \right\rangle = \int_{-\infty}^{t} dt' \varepsilon_{ijk} \left\langle v_j' B_l \frac{\partial v_k'}{\partial x_l} - v_j' v_l' \frac{\partial B_k}{\partial x_l} \right\rangle \tag{4.11}$$

For simplicity, let us replace the time integral with τ (characteristic time scale of turbulence) and assume homogeneity and isotropy. (Velocity is isotropic $v_x' \sim v_y' \sim v_z'$ and invariant under rotations. Also non-diagonal terms vanish.) For

example, x-component of the first term of RHS of Eq.(4.11) becomes

$$\begin{aligned}\left\{\boldsymbol{v}' \times \left[\left(\boldsymbol{B}\cdot\boldsymbol{\nabla}\right)\boldsymbol{v}'\right]\right\}_x &\sim B_x v_x' \left(\partial_x v_z' - \partial_x v_y'\right) \\ &\sim B_x v_z' \left(\partial_y v_x' - \partial_x v_y'\right) = -\frac{1}{3} B_x \left(\boldsymbol{v}'\cdot\boldsymbol{\omega}'\right), \end{aligned} \tag{4.12}$$

where $\boldsymbol{\omega}' = \boldsymbol{\nabla}\times\boldsymbol{v}'$. In this way, the electromotive force becomes

$$\left\langle \boldsymbol{v}'\times\boldsymbol{b}'\right\rangle \sim -\frac{\tau}{3}\left\langle \boldsymbol{v}'\cdot\boldsymbol{\omega}'\right\rangle \boldsymbol{B} - \frac{\tau}{3}\left\langle \boldsymbol{v}'^2\right\rangle \boldsymbol{J}, \tag{4.13}$$

where $\left\langle \boldsymbol{v}'\cdot\boldsymbol{\omega}'\right\rangle$ and $\left\langle \boldsymbol{v}'^2\right\rangle$ are, respectively turbulent kinetic helicity and energy. This is often expressed as

$$\left\langle \boldsymbol{v}'\times\boldsymbol{b}'\right\rangle = \alpha_t \boldsymbol{B} - \beta_t \boldsymbol{J}, \tag{4.14}$$

where $\alpha_t = -\tau\left\langle \boldsymbol{v}'\cdot\boldsymbol{\omega}'\right\rangle/3$ and $\beta_t = \tau\left\langle \boldsymbol{v}'^2\right\rangle/3$ are turbulent transport coefficients for the first-order smoothing approximation, which reflect the information of fluctuations.

Substituting Eq.(4.14) into Eq.(4.4) gives

$$\frac{\partial \boldsymbol{B}}{\partial t} = \boldsymbol{\nabla}\times\left(\boldsymbol{V}\times\boldsymbol{B} + \alpha_t\boldsymbol{B}\right) - \boldsymbol{\nabla}\times\left[\left(\eta+\beta_t\right)\boldsymbol{J}\right], \tag{4.15}$$

α_t contributes to magnetic field generation and β_t contributes to the enhancement of effective magnetic field diffusion. Large fluctuation level (turbulent energy) enhances the β_t effect, and the helicity enhances the α_t effect.

In more realistic cases, one should consider the effects of mean velocity and vorticity. In the above model, the velocity shear is neglected and the mean flow is dropped by a simple Galilean transformation. However, in general, this assumption fails, and the large scale velocity shear should be also taken into account in the model. In this case, one can obtain the following electromotive force after

some algebraic calculation[1] as

$$\langle \boldsymbol{v}' \times \boldsymbol{b}' \rangle \sim \alpha_t \boldsymbol{B} - \beta_t \boldsymbol{J} + \gamma_t \boldsymbol{\Omega}, \tag{4.19}$$

with turbulent transport coefficients

$$\alpha_t = \frac{\tau}{3}\mathcal{H}, \quad \beta_t = \frac{2\tau}{3}\mathcal{K}, \quad \gamma_t = \frac{2\tau}{3}\mathcal{W}. \tag{4.20}$$

$\mathcal{H} \equiv \langle \boldsymbol{b}' \cdot \boldsymbol{j}' - \boldsymbol{v}' \cdot \boldsymbol{\omega}' \rangle$, $\mathcal{K} \equiv \langle \boldsymbol{v}'^2 + \boldsymbol{b}'^2 \rangle / 2$, and $\mathcal{W} \equiv \langle \boldsymbol{v}' \cdot \boldsymbol{b}' \rangle$ are respectively turbulent residual helicity, turbulent energy, and cross-helicity. Hence in general cases, not only α_t and β_t effects, the cross-helicity (γ_t) effect should be taken into account. One can simply understand Eqs.(4.19) by the basic MHD equations for

[1] From Eqs.(4.7) and (4.8),

$$\begin{aligned}
\frac{\partial}{\partial t}\left(\boldsymbol{v}' \times \boldsymbol{b}'\right)_i &= \epsilon_{ijk}\left(v'_j \frac{\partial b'_k}{\partial t} + b'_k \frac{\partial v'_j}{\partial t}\right) \\
&= \epsilon_{ijk}\left(v'_j B_l \frac{\partial v'_k}{\partial x_l} - v'_j v'_l \frac{\partial B_k}{\partial x_l} + v'_j b'_l \frac{\partial V_k}{\partial x_l} - v'_j V_l \frac{\partial b'_k}{\partial x_l}\right. \\
&\quad + b'_k B_l \frac{\partial b'_j}{\partial x_l} + b'_k b'_l \frac{\partial B_j}{\partial x_l} - b'_k v'_l \frac{\partial V_j}{\partial x_l} + b'_k V_l \frac{\partial v'_j}{\partial x_l} \\
&\quad + v'_j b'_l \frac{\partial v'_k}{\partial x_l} - v'_j v'_l \frac{\partial b'_k}{\partial x_l} + v'_j \epsilon_{klm} \frac{\partial E_{M,m}}{\partial x_l} - \eta v'_j \frac{\partial^2 b'_k}{\partial x_l^2} \\
&\quad \left. - b'_k v'_l \frac{\partial v'_j}{\partial x_l} + b'_k b'_l \frac{\partial b'_j}{\partial x_l} - b'_k \frac{\partial R_{jl}}{\partial x_l} + \nu b'_k \frac{\partial^2 v'_j}{\partial x_l^2}\right).
\end{aligned} \tag{4.16}$$

Taking ensemble average and also making homogeneous and isotropic assumptions [100]

$$\langle f'_a g'_b \rangle + \langle g'_a f'_b \rangle = \frac{2}{3}\delta_{ab} \langle f'_i g'_i \rangle \tag{4.17}$$

(where f' and g' are fluctuating variables) gives the time evolution of ensemble-averaged electromotive force:

$$\begin{aligned}
\frac{\partial}{\partial t}\langle \boldsymbol{v}' \times \boldsymbol{b}' \rangle \sim &- (\boldsymbol{V} \cdot \boldsymbol{\nabla}) \langle \boldsymbol{v}' \times \boldsymbol{b}' \rangle + \frac{\langle \boldsymbol{b}' \cdot \boldsymbol{j}' - \boldsymbol{v}' \cdot \boldsymbol{\omega}' \rangle}{3} \boldsymbol{B} \\
&- \frac{\langle \boldsymbol{v}'^2 + \boldsymbol{b}'^2 \rangle}{3} \boldsymbol{J} + \frac{2}{3} \langle \boldsymbol{v}' \cdot \boldsymbol{b}' \rangle \boldsymbol{\Omega} + \boldsymbol{RT}^{(3\mathrm{rd})},
\end{aligned} \tag{4.18}$$

where $\boldsymbol{RT}^{(3\mathrm{rd})}$ represents remaining terms which includes 3rd-order correlation terms.

turbulent fields (Eqs.(4.7) and (4.8)):

$$\frac{\partial v_i'}{\partial t} = \underbrace{B_j \frac{\partial b_i'}{\partial x_j}}_{\alpha_{t,\mathrm{magnetic}}} + \underbrace{b_j' \frac{\partial B_i}{\partial x_j}}_{\beta_{t,\mathrm{magnetic}}} - \underbrace{v_j' \frac{\partial V_i}{\partial x_j}}_{\gamma_t} - V_j \frac{\partial v_i'}{\partial x_j} + (\text{nonlinear terms}), \tag{4.21}$$

$$\frac{\partial b_i'}{\partial t} = \underbrace{B_j \frac{\partial v_i'}{\partial x_j}}_{\alpha_{t,\mathrm{kinetic}}} + \underbrace{b_j' \frac{\partial V_i}{\partial x_j}}_{\gamma_t} - \underbrace{v_j' \frac{\partial B_i}{\partial x_j}}_{\beta_{t,\mathrm{kinetic}}} - V_j \frac{\partial v_i'}{\partial x_j} + (\text{nonlinear terms}), \tag{4.22}$$

where only the terms related to α_t–γ_t effects are shown. For example in Eq.(4.21), if mean velocity shear is present, background turbulence amplifies velocity fluctuation and contributes to the γ_t effect in the electromotive force. As well, mean magnetic field shear and mean magnetic field contribute to α_t and β_t effects. (In more detail and intuitive explanations, see [100].) Above explanations are based on some assumptions for the sake of simplicity (isotropic assumption in Eq.(4.17) and a first-order smoothing approximation where the nonlinear terms in Eq.(4.21)–(4.22) are dropped), but one can also derive Eq.(4.19) by evaluating nonlinear terms in Eq.(4.21)–(4.22) (which is valid even in the case $R_m \gg 1$) from the closure theory of turbulence [107] [2].

[2] Yoshizawa introduced a closure theory called as a two-scale direct-interaction approximation (TSDIA) [104, 105], which extended the direct-interaction approximation for homogeneous turbulence [52] to inhomogeneous one. Using TSDIA analysis, turbulent transport coefficients can be expressed by

$$\alpha_t = \frac{1}{3}\int d\boldsymbol{k} \int_{-\infty}^{t} dt' G(k,t,t') \left[-H_{vv}(k,t,t') + H_{bb}(t,t,t')\right], \tag{4.23}$$

$$\beta_t = \frac{1}{3}\int d\boldsymbol{k} \int_{-\infty}^{t} dt' G(k,t,t') \left[Q_{vv}(k,t,t') + Q_{bb}(k,t,t')\right], \tag{4.24}$$

$$\gamma_t = \frac{1}{3}\int d\boldsymbol{k} \int_{-\infty}^{t} dt' G(k,t,t') \left[Q_{vb}(k,t,t') + Q_{bv}(k,t,t')\right], \tag{4.25}$$

where G is the response function for inhomogeneous turbulence, and H_{vv}, H_{bb}, Q_{vv}, Q_{bb}, and Q_{vb} are spectral functions for turbulent kinetic helicity, current helicity, kinetic energy, magnetic energy, and cross-helicity, respectively. The reduced model for turbulent transport coefficients may be expressed as $\alpha_t = C_\alpha \tau \mathcal{H}$, $\beta_t = C_\beta \tau \mathcal{K}$, and $\gamma_t = C_\gamma \tau \mathcal{W}$, where the time integration is replaced by the characteristic time scale of turbulence and the spectral information is integrated

Equations of turbulent energy, cross-helicity, and residual helicity

In the above subsection, modeling of turbulent electromotive force was introduced. The electromotive force is determined by turbulent transport coefficients α_t, β_t, and γ_t. And in a simplified case, these turbulent transport coefficients depend on turbulent statistics such as turbulent energy $\mathcal{K}$, cross-helicity $\mathcal{W}$, and turbulent residual helicity $\mathcal{H}$ as shown in Eq.(4.20). Usually, turbulent transport coefficients are given by ad hoc parameters or some spatiotemporal functions estimated by observations and theoretical analogy, but one can also construct equations for spatiotemporal evolution for them.

Since equations for turbulent field are strictly given, one can calculate equations of time evolution of $\mathcal{K}$, $\mathcal{W}$, and $\mathcal{H}$

$$\frac{\partial \mathcal{K}}{\partial t} = \left\langle \boldsymbol{v}' \cdot \frac{\partial \boldsymbol{v}'}{\partial t} + \boldsymbol{b}' \cdot \frac{\partial \boldsymbol{b}'}{\partial t} \right\rangle, \tag{4.26}$$

$$\frac{\partial \mathcal{W}}{\partial t} = \left\langle \boldsymbol{b}' \cdot \frac{\partial \boldsymbol{v}'}{\partial t} + \boldsymbol{v}' \cdot \frac{\partial \boldsymbol{b}'}{\partial t} \right\rangle, \tag{4.27}$$

$$\frac{\partial \mathcal{H}}{\partial t} = \left\langle \boldsymbol{b}' \cdot \frac{\partial \boldsymbol{j}'}{\partial t} + \boldsymbol{j}' \cdot \frac{\partial \boldsymbol{b}'}{\partial t} - \boldsymbol{v}' \cdot \frac{\partial \boldsymbol{\omega}'}{\partial t} - \boldsymbol{\omega}' \cdot \frac{\partial \boldsymbol{v}'}{\partial t} \right\rangle. \tag{4.28}$$

After some algebraic calculations, one obtains following equations:

$$\left(\frac{\partial}{\partial t} + \boldsymbol{V} \cdot \boldsymbol{\nabla} \right) \mathcal{G} = P_{\mathcal{G}} + T_{\mathcal{G}} - \epsilon_{\mathcal{G}} + f_{\mathcal{G}}, \tag{4.29}$$

where $\mathcal{G}$ represents turbulent quantities such as $\mathcal{K}$, $\mathcal{W}$, and $\mathcal{H}$. $P_{\mathcal{G}}$, $T_{\mathcal{G}}$, $\epsilon_{\mathcal{G}}$, and $f_{\mathcal{G}}$ are respectively production, transport, dissipation rate, and source terms for turbulence. In the following study, the source term $f_{\mathcal{G}}$, which stands for the source of turbulence beyond the MHD approximation, is neglected. $P_{\mathcal{G}}$, $T_{\mathcal{G}}$, and $\epsilon_{\mathcal{G}}$ can

with respect to wave number k. C_α, C_β, and C_γ are model constants, and they are estimated as $C_\alpha = \mathcal{O}(10^{-2})$, $C_\beta = \mathcal{O}(10^{-1})$, and $C_\gamma = \mathcal{O}(10^{-1})$ by the direct numerical simulations of the Kolmogorov flow test problem [36].

be written by[3]

$$P_{\mathcal{K}} = -\left\langle \boldsymbol{v}' \times \boldsymbol{b}' \right\rangle \cdot \boldsymbol{J} - R_{ij} \frac{\partial V_j}{\partial x_i}, \tag{4.31}$$

$$T_{\mathcal{K}} = \left(\boldsymbol{B} \cdot \boldsymbol{\nabla}\right) \mathcal{W} + \boldsymbol{\nabla} \cdot \boldsymbol{T}'_{\mathcal{K}}, \tag{4.32}$$

$$\epsilon_{\mathcal{K}} = \nu \left\langle \left(\frac{\partial v'_i}{\partial x_j} \right)^2 \right\rangle + \eta \left\langle \left(\frac{\partial b'_i}{\partial x_j} \right)^2 \right\rangle, \tag{4.33}$$

$$P_{\mathcal{W}} = -\left\langle \boldsymbol{v}' \times \boldsymbol{b}' \right\rangle \cdot \boldsymbol{\Omega} - R_{ij} \frac{\partial B_j}{\partial x_i}, \tag{4.34}$$

$$T_{\mathcal{W}} = \left(\boldsymbol{B} \cdot \boldsymbol{\nabla}\right) \mathcal{K} + \boldsymbol{\nabla} \cdot \boldsymbol{T}'_{\mathcal{W}}, \tag{4.35}$$

$$\epsilon_{\mathcal{W}} = (\nu + \eta) \left\langle \left(\frac{\partial v'_i}{\partial x_j} \right) \left(\frac{\partial b'_i}{\partial x_j} \right) \right\rangle. \tag{4.36}$$

$\boldsymbol{T}'_{\mathcal{K}}$ and $\boldsymbol{T}'_{\mathcal{W}}$ are higher-order terms [105]. (As a first step such terms are neglected here, but should be taken into account in future works.) The above equations are for turbulent energy and cross-helicity. Because the volume average of turbulent

[3] For example in the turbulent energy case, one obtains the following formulae from Eq.(4.7) and (4.8):

$$\begin{aligned} v'_i \frac{\partial v'_i}{\partial t} + b'_i \frac{\partial b'_i}{\partial t} = & \underbrace{-V_j \left(v'_i \frac{\partial v'_i}{\partial x_j} + b'_i \frac{\partial b'_i}{\partial x_j} \right)}_{\text{advection related}} \\ & \underbrace{- \left(v'_i v'_j - b'_i b'_j \right) \frac{\partial V_i}{\partial x_j} + \left(v'_i b'_j - b'_i v'_j \right) \frac{\partial B_i}{\partial x_j}}_{\text{production related}} \\ & \underbrace{+ B_j \left(b'_i \frac{\partial v'_i}{\partial x_j} + v'_i \frac{\partial b'_i}{\partial x_j} \right) - \left(v'_i v'_j - b'_i b'_j \right) \frac{\partial v'_i}{\partial x_j} + \left(v'_i b'_j - b'_i v'_j \right) \frac{\partial b'_i}{\partial x_j}}_{\text{transport related}} \\ & \underbrace{- \nu \left(\frac{\partial v'_i}{\partial x_j} \right)^2 - \eta \left(\frac{\partial b'_i}{\partial x_j} \right)^2}_{\text{dissipation rate related}} \\ & - v'_i \frac{\partial R_{ij}}{\partial x_j} + \varepsilon_{ijk} b'_i \frac{\partial E_{M,k}}{\partial x_j} + \nu \frac{\partial^2}{\partial x_j^2} \left(\frac{v'^2_i}{2} \right) + \eta \frac{\partial^2}{\partial x_j^2} \left(\frac{b'^2_i}{2} \right). \end{aligned} \tag{4.30}$$

Working out a sum and taking ensemble averaging gives Eq.(4.29)–(4.33).

energy and cross-helicity are both conserved MHD quantities, the equations for the time evolution are rather robust. For example, if $\eta \ll 1$ and $\nu \ll 1$ in Eqs. (4.1)–(4.2), the time evolution of the volume average of the cross-helicity can be calculated as

$$\frac{\partial}{\partial t}\int_{\mathcal{V}} (\boldsymbol{v}\cdot\boldsymbol{b})\, d\mathcal{V} = \int_{\mathcal{V}} \{-\boldsymbol{b}\cdot[(\boldsymbol{v}\cdot\boldsymbol{\nabla})\,\boldsymbol{v}] - \boldsymbol{b}\cdot\boldsymbol{\nabla}p_t + \boldsymbol{v}\cdot[\boldsymbol{\nabla}\times(\boldsymbol{v}\times\boldsymbol{b})]\}\, d\mathcal{V} \tag{4.37}$$
$$= \int_{\mathcal{S}} \left[-\frac{\boldsymbol{v}^2}{2}\boldsymbol{b} - p_t\boldsymbol{b} + (\boldsymbol{v}\times\boldsymbol{b})\times\boldsymbol{b}\right]\cdot d\boldsymbol{\mathcal{S}}.$$

So, it conserves in the periodic system. On the other hand, the residual helicity is not the conserved quantity and how to construct the α_t related equation is a challenging problem. Preceding mean field approach suggests that the α_t effect may be small compared to other effects if the helicity of mean field is small [9, 106]. This study consider the most basic reconnection problem, where the helical structure is zero in the initial current sheet, $\boldsymbol{B}\cdot\boldsymbol{J} = 0$, and the α_t effect is neglected.

§ 4.2 Numerical Model and Setup

4.2.1 Numerical model

The simulation model presented here is based on the Reynolds-averaged MHD concept shown in the previous section. Basic equations, which describe motion of mean fields, are written by

$$\frac{\partial \rho}{\partial t} + \boldsymbol{\nabla} \cdot (\rho \boldsymbol{V}) = 0, \tag{4.38}$$

$$\frac{\partial}{\partial t}(\rho \boldsymbol{V}) + \boldsymbol{\nabla} \cdot \left[\rho \boldsymbol{V}\boldsymbol{V} + \left(P + \frac{B^2}{2} \right) \overleftrightarrow{\boldsymbol{I}} - \boldsymbol{B}\boldsymbol{B} \right] = \boldsymbol{0}, \tag{4.39}$$

$$\begin{aligned} &\frac{\partial}{\partial t}\left(\frac{P}{\gamma_{\rm adi} - 1} + \frac{\rho}{2} V^2 + \frac{B^2}{2} \right) \\ &+ \boldsymbol{\nabla} \cdot \left[\left(\frac{\gamma_{\rm adi}}{\gamma_{\rm adi} - 1} P + \frac{\rho}{2} V^2 \right) \boldsymbol{V} + \boldsymbol{E} \times \boldsymbol{B} \right] = \epsilon_{\rm exc}, \end{aligned} \tag{4.40}$$

$$\frac{\partial \boldsymbol{B}}{\partial t} + \boldsymbol{\nabla} \times \boldsymbol{E} = \boldsymbol{0}, \tag{4.41}$$

$$\boldsymbol{E} + \boldsymbol{V} \times \boldsymbol{B} + \langle \boldsymbol{v}' \times \boldsymbol{b}' \rangle - \eta \boldsymbol{J} = \boldsymbol{0}, \tag{4.42}$$

where velocity is normalized by the Alfvén velocity (see Appendix for the normalization). $\epsilon_{\rm exc} = \langle \boldsymbol{v}' \times \boldsymbol{b}' \rangle \cdot \boldsymbol{J} + \epsilon_{\mathcal{K}}$ is an energy exchange term between mean and turbulent fields. $\gamma_{\rm adi}$ is an adiabatic constant and set to $5/3$. Additionally, the electric resistivity $\eta = 2.0 \times 10^{-2}$ is assumed to avoid a numerical instability. Here, we applied the model for inhomogeneous MHD turbulence [105, 108, 100] (TSDIA). The electromotive force $\langle \boldsymbol{v}' \times \boldsymbol{b}' \rangle$ are expressed as

$$\langle \boldsymbol{v}' \times \boldsymbol{b}' \rangle \overset{\text{model}}{=} -\beta_t \boldsymbol{J} + \gamma_t \boldsymbol{\Omega}, \tag{4.43}$$

and, here, turbulent transport coefficients β_t, and γ are expressed as

$$\beta_t = C_\beta \tau \mathcal{K}, \tag{4.44}$$

$$\gamma_t = C_\gamma \tau \mathcal{W} \tag{4.45}$$

using characteristic time scale of turbulence τ. C_β and C_γ are model constants of $O(10^{-1})$ as is discussed in the previous section. In this study, these constants are set to $C_\beta = C_\gamma = 0.3$. It is checked that the simulation results do not strongly depend on their exact values. The turbulent energy $\mathcal{K} = \langle \boldsymbol{v}'^2 + \boldsymbol{b}'^2 \rangle / 2$ and cross-helicity $\mathcal{W} = \langle \boldsymbol{v}' \cdot \boldsymbol{b}' \rangle$ are solved by [102];

$$\frac{\partial \mathcal{K}}{\partial t} = - \langle \boldsymbol{v}' \times \boldsymbol{b}' \rangle \cdot \boldsymbol{J} + (\boldsymbol{B} \cdot \boldsymbol{\nabla}) \mathcal{W} - (\boldsymbol{V} \cdot \boldsymbol{\nabla}) \mathcal{K} - \epsilon_{\mathcal{K}}, \tag{4.46}$$

$$\frac{\partial \mathcal{W}}{\partial t} = - \langle \boldsymbol{v}' \times \boldsymbol{b}' \rangle \cdot \boldsymbol{\Omega} + (\boldsymbol{B} \cdot \boldsymbol{\nabla}) \mathcal{K} - (\boldsymbol{V} \cdot \boldsymbol{\nabla}) \mathcal{W} - \epsilon_{\mathcal{W}}. \tag{4.47}$$

$\epsilon_{\mathcal{K}}$ and $\epsilon_{\mathcal{W}}$ are dissipation rates for turbulent energy and cross-helicity, respectively, and expressed as

$$\epsilon_{\mathcal{K}} \overset{\text{model}}{=} \frac{\mathcal{K}}{\tau}, \tag{4.48}$$

$$\epsilon_{\mathcal{W}} \overset{\text{model}}{=} C_{\mathcal{W}} \frac{\mathcal{W}}{\tau}, \tag{4.49}$$

where $C_{\mathcal{W}}$ is a model constant [99], and set to 1.0–2.0. The characteristic time scale of turbulence τ is assumed to be constant through simulations, and is an important simulation parameter which control dissipation rates of turbulent energy and cross-helicity. Instead of above τ-constant model, one may further develop the model by solving equations of $\epsilon_{\mathcal{K}}$ and $\epsilon_{\mathcal{W}}$.

The above set of Eqs.(4.38)–(4.49) is solved using the fourth-order Runge-Kutta and fourth-order central difference scheme, and numerical errors of physical quantities (ρ, P, $\boldsymbol{V}$, $\boldsymbol{B}$, $\mathcal{K}$, $\mathcal{W}$) are controlled using diffusive flux introduced by [74]. (In the present study, the hyper-diffusive type scheme [95] is also examined to solve Eqs.(4.38)–(4.49). The result shows the same result but it is found that

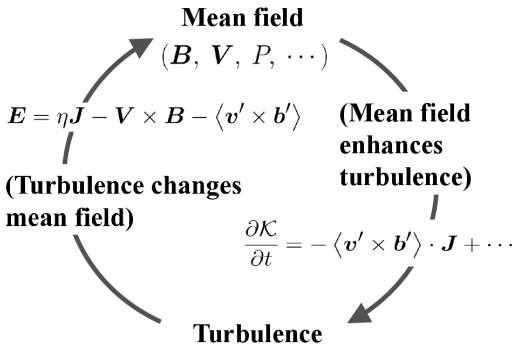

Figure 4.2: A schematic view for the interaction between mean and turbulent fields.

the present code can save calculation time compared to the hyper-diffusive type one.) The numerical error of $\boldsymbol{\nabla}\cdot\boldsymbol{B}$ is cleaned by either diffusion-iteration type [74] or advection-diffusion type schemes [18]. (It is checked that both of them produce the same results.) Simulation time interval Δ_t is determined by $\Delta_t = \mathrm{MIN}(\Delta_{t,\mathrm{adv}}, \Delta_{t,\mathrm{turb}})$ (such as a hyper-diffusion method [95]), where $\Delta_{t,\mathrm{adv}}$ and $\Delta_{t,\mathrm{turb}}$ are respectively time intervals determined by CFL conditions depending on the total wave speed ($V_{\mathrm{wave}} \equiv |\boldsymbol{V}| + V_A + \sqrt{\gamma_{\mathrm{adi}} P/\rho}$) and turbulent transport coefficients (β_t and γ_t).

4.2.2 Initial conditions

In this simulation model, we must give the initial conditions for both the mean field (such as B and P) and the turbulent field (such as $\mathcal{K}$ and $\mathcal{W}$). Since this study is a first challenge for magnetic reconnection using a Reynolds-averaged MHD procedure, the simplest setup for magnetic reconnection is applied and the system is in two-dimensions (x-y plane). Grid intervals Δ_x and Δ_y are set to unity, and the size of simulation box is $L_x \times L_y = 2048 \times 512$. Boundary conditions in x

and y directions are, respectively, periodic and Neuman-type ($\partial_y = 0$) conditions.

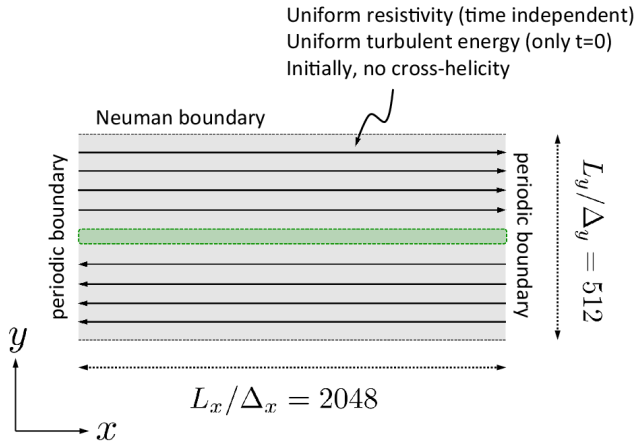

Figure 4.3: Initial conditions and boundary conditions.

As for the initial mean field, a Harris equilibrium [37] is assumed: The mean magnetic field is given by

$$\boldsymbol{B} = B_{x0} \tanh\left(\frac{y}{\delta_c}\right) \boldsymbol{e}_x + B_{y0} \sum_{m=1}^{10} \sin\left(\frac{2\pi m x}{L_x}\right) \boldsymbol{e}_y, \tag{4.50}$$

where $\boldsymbol{e}_x$ and $\boldsymbol{e}_y$ are, respectively, the unit vectors in x and y directions. δ_c ($= 0.02$ L_y) is the half thickness of a current sheet. Magnetic field perturbation to trigger reconnection is set to $B_{y0}/B_{x0} = 2.0 \times 10^{-3}$. The plasma beta outside the current sheets is set to $\beta_p = 0.5$, and the spatial distribution of P is determined to satisfy the pressure balance. The electric resistivity $\eta = 2.0 \times 10^{-2}$ is given uniformly in both time and space to avoid unphysical numerical reconnection.

As for the initial turbulent field, we assume $\mathcal{W} = 0$ and $\mathcal{K} = 1.0 \times 10^{-2}$ everywhere. We found that the magnitude of $\mathcal{K}$ did not change the basic property of turbulent reconnection. In addition, a steady state of turbulent energy, $\partial_t \mathcal{K} = 0$,

is assumed in the initial current sheets. Because $\boldsymbol{\Omega} = \boldsymbol{V} = 0$ and $\mathcal{W} = 0$ at the center of the initial current sheets, the initial balance for $\mathcal{K}$ becomes

$$0 = \beta_t \boldsymbol{J}^2 - \epsilon_{\mathcal{K}}. \tag{4.51}$$

(Eqs.(4.46) and (4.48) are used.) Therefore it holds $\tau_0 = C_\beta^{-1/2} |\boldsymbol{J}|_{y=0}^{-1}$ in the steady state (Here Eqs. (4.44) and (4.48) are used.) In the present simulation, $\tau_0/\tau_A \sim 2$, where $\tau_A \equiv \delta_c/V_A$ is the Alfvén transit time. In order to investigate the relationship between turbulence and reconnection, the characteristic time scale of turbulence τ should be given in this model. Noted that τ is constant throughout each simulation run. Simulations are executed with different τ values, and the characteristic cases A–D are summarized in Table 4.1. (The total number of simulation runs corresponds to the number of points in Fig. 4.6.) It is again emphasized that τ controls the dissipation rate of turbulent energy $\epsilon_{\mathcal{K}}$, and changing the dissipation rate stands for controlling the energy transfer from large scale to smaller scales. If τ/τ_0 is much smaller than unity, $\epsilon_{\mathcal{K}}$ becomes $\epsilon_{\mathcal{K}} \gg 1$. In this case, since the energy transfer from large scale to the smaller scales exceeds that injected by the mean field, $\mathcal{K} \to 0$ and the system will develop into laminar flow. On the other hand, in the case of $\tau/\tau_0 \gg 1$, it is expected that the system quickly becomes turbulent, and reconnection will not occur owing to strong turbulent diffusion. (Here it is noted from Eq. (4.15) that the turbulent diffusion of the mean magnetic field increases as $\mathcal{K}$ increases.) Therefore, in this study, we focus on the most interesting parameters around $\tau/\tau_0 \sim 1$.

Table 4.1: Main simulation parameters

RUN	A	$\cdots$	B	$\cdots$	C	$\cdots$	D
τ/τ_0	0.05	$\cdots$	0.5	$\cdots$	1.2	$\cdots$	3.0

§ 4.3 Results and discussions

Let us first discuss the basic signatures of turbulent magnetic reconnection, such as the spatial structures, the reconnection rate and the cross-helicity effects, including β_t and γ_t effects. Figures 4.4 and 4.5–4.6 respectively show the structure of reconnection and the reconnection speed, depending on the characteristic time scale of turbulence, τ. In Fig. 4.4(a)–(d), the z components of the electric current (upper color contours) and the magnetic field lines (lower contours) at $t/\tau_A = 150$ are shown. Time is normalized by the Alfvén transit time, τ_A. From top to bottom, $\tau/\tau_0 = 0.05,\ 0.5,\ 1.2,\ 3.0$ cases are shown. The black arrows overlaid on the magnetic field lines stand for the plasma flow. Fig.4.5 shows the reconnection electric field, E_R, the inflow Alfvén Mach number, $\mathcal{M}_A$, and the reconnected flux, Λ_R. They are defined by

$$E_R \equiv \frac{1}{D_x D_y}\int_{-D_x/2}^{+D_x/2} dx \int_{-D_y/2}^{+D_y/2} dy\, |E_z|\,, \tag{4.52}$$

$$\mathcal{M}_A \equiv \frac{1}{2D_x}\int_{-D_x/2}^{+D_x/2} dx \left| \left(\frac{V_y}{V_A}\right)_{y=+D_y/2} - \left(\frac{V_y}{V_A}\right)_{y=-D_y/2} \right|, \tag{4.53}$$

$$\Lambda_R \equiv \frac{1}{L_x}\int_{-L_x/2}^{+L_x/2} dx \frac{|B_y|_{y=0}}{B_{x0}}, \tag{4.54}$$

where D_x and D_y are characteristic length to measure above values, and respectively set to $0.1L_x$ and $0.1L_y$. The line colors represent each Run, and the notation is shown in the figure. The reconnection rate (E_R, $\mathcal{M}_A$, and Λ_R) at $t/\tau_A = 150$ is shown in Fig.4.6.

Results suggest that the reconnection develops in three ways depending on the time scale of turbulence. For the small τ case ($\tau/\tau_0 \lesssim 0.5$; Fig.4.4(a) and (b)), a Sweet–Parker-type current sheet forms as shown by resistive MHD simulations [8, 92], and reconnection is more gradual than other cases. The reconnection rates are shown by black and blue lines in Fig.4.5 and 4.6. Magnetic fields begin to reconnect with each other at $t/\tau_A \sim 10$, and the reconnected magnetic field

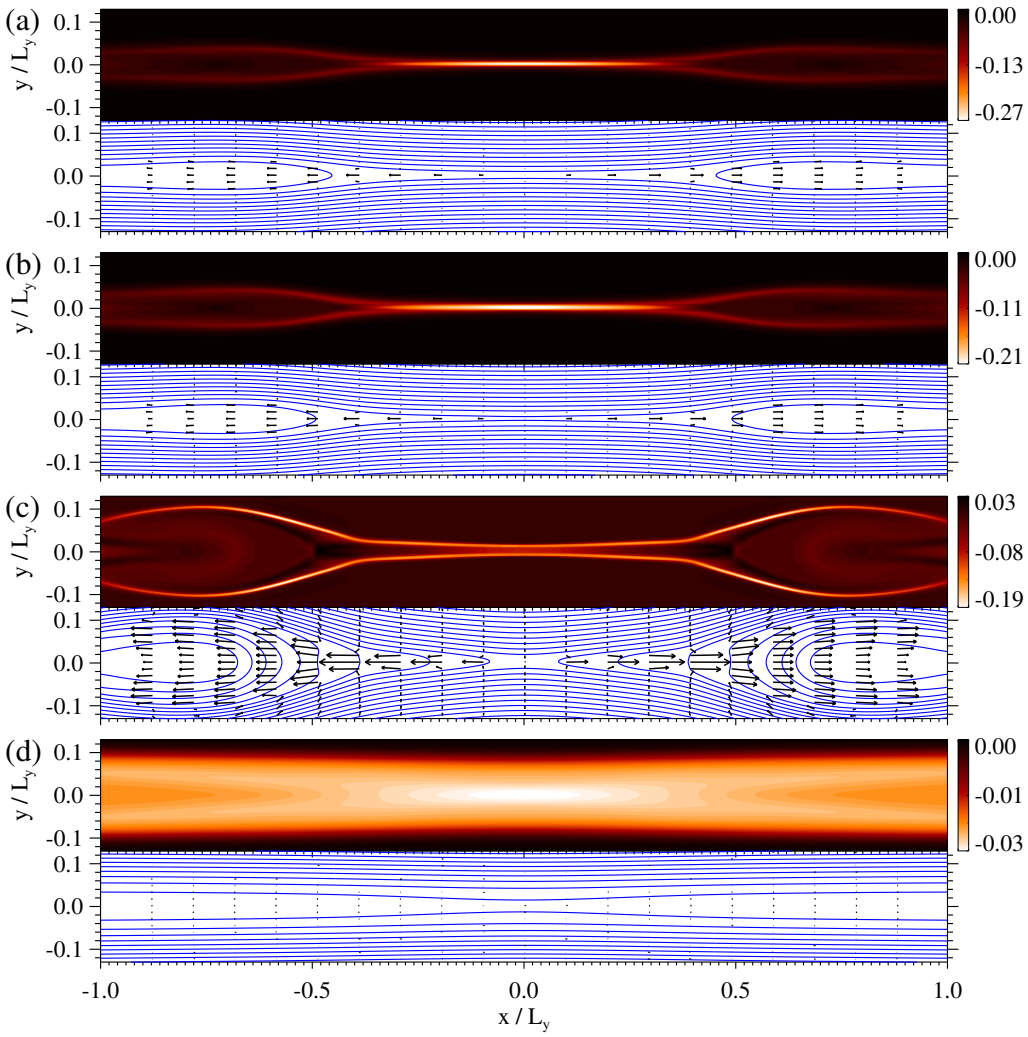

Figure 4.4: Spatial distributions of z component of the electric current (upper contours) and magnetic field lines (below blue lines) for the cases of (a) $\tau/\tau_0 = 0.05$, (b) $\tau/\tau_0 = 0.5$, (c) $\tau/\tau_0 = 1.2$, and (d) $\tau/\tau_0 = 3.0$ are shown. Flow vectors are overlaid as black arrows.

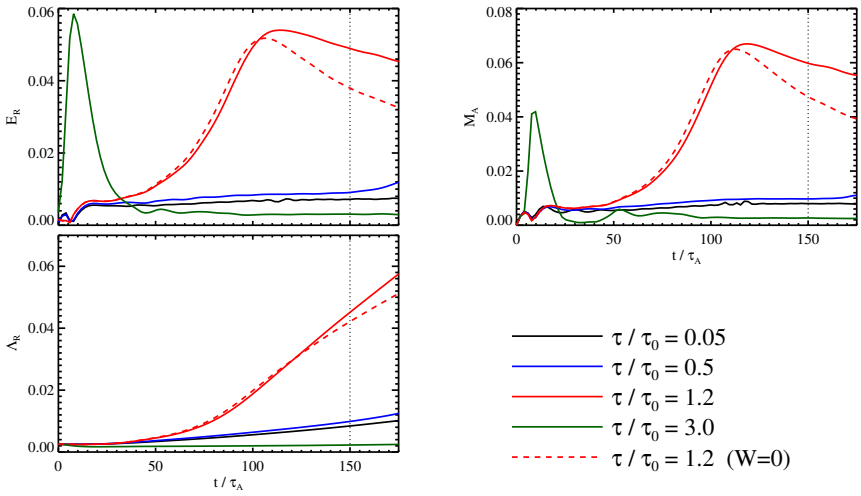

Figure 4.5: Time evolutions of the reconnection electric field, E_R, the Alfvén Mach number in the inflow region, $\mathcal{M}_A$, and the reconnected magnetic flux Λ_R are shown. Black, blue, red, and dark-green lines respectively show the results of Run A–D. The red-dashed line shows the result, where the cross-helicity effect is turned off.

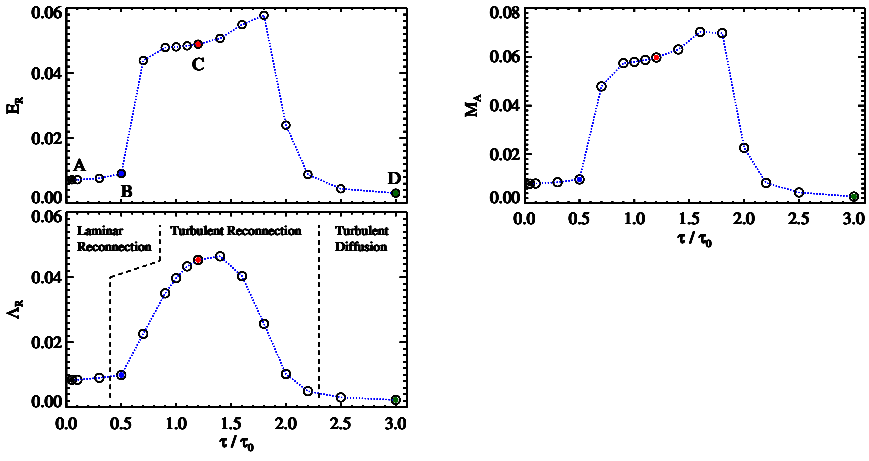

Figure 4.6: The reconnection electric field, inflow Alfvén Mach number, and the reconnected magnetic flux at time $t/\tau_A = 150$ are shown. The horizontal axis is τ parameter that control the dissipation rate of turbulence.

gradually increases as time goes on. At $t/\tau_A = 150$, the reconnection speed reaches a steady state, and E_R, $\mathcal{M}_A$, and Λ_R are almost the same independent of τ as long as $\tau/\tau_0 < 0.5$. In this case, the turbulent energy decreases in the initial current sheet (discussed later) and becomes smaller than the electric resistivity, i.e., $\beta_t < \eta$. So the reconnection develops into a simple Sweet–Parker-type.

On the other hand, for the large τ ($\tau/\tau_0 = 3.0$), the initial current sheet (with thickness $\sim 0.02\, y/L_y$) quickly broadens as shown in Fig.4.4(d). At the first stage, the out-of-plane electric field, E_R, increases, while the reconnected magnetic field flux remains constant as shown in Fig.4.5 (the green line). In the steady state ($t/\tau_A = 150$), the reconnection rate becomes even smaller than that of Sweet-Parker reconnection. The magnetic field energy is certainly converted into the thermal energy, however, the reconnection does not take place and there is no energy conversion into the kinetic energy.

In the moderate parameter ($\tau/\tau_0 \sim 1$) where the initial turbulent energy is sustained in the current sheet, Petschek-type two pairs of current sheets [72] form as shown in Fig.4.4(c), and reconnection jets with wide flare-angle, whose outflow velocity is almost the Alfvén velocity in the inflow region, are observed. In $t/\tau_A = 20$–30, the reconnection switches to fast one, and the reconnection rate ($\mathcal{M}_A$) reaches ~ 0.06–0.07. The existence of fast Petschek-type reconnection itself has been supported by the results of anomalous resistivity models [77, 90], that assume specific functions for the electric current or the plasma flow at the neutral X-point. However the inherent physical processes such as the anomalous resistivity and a scale-coupling problem has been treated as an open issue. One of important contributions of this study in reconnection researches would be in the point that the physics of magnetic field diffusion could be explained by the enhancement and suppression of MHD turbulence.

Let us further discuss the role of turbulence in the above fast turbulent reconnection. Figure 4.7 shows the time profile of the spatial maximum values such as turbulent energy, $\mathcal{K}_{\max}$, and the turbulent electromotive force, $E_{M,\max}$. The color stands for each simulation Run as the same manner in Fig.4.5, and the profile in

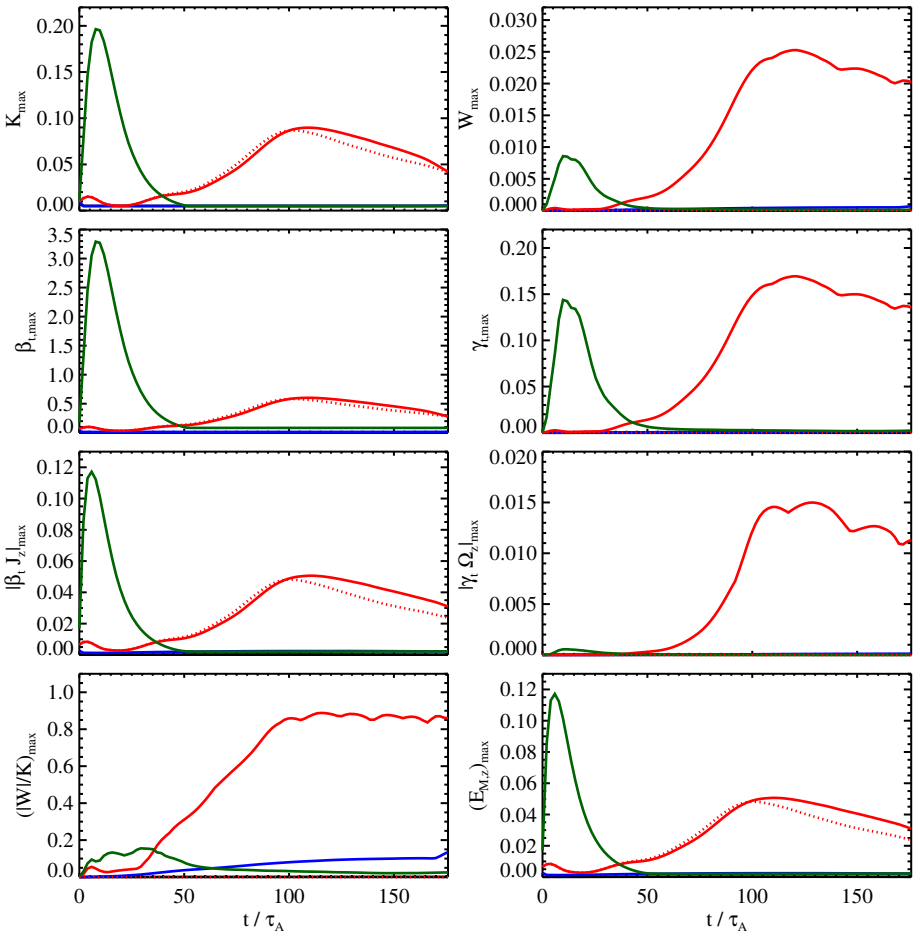

Figure 4.7: Time profiles of maximum (spatially) values. From the upper left to lower right, the profiles of the turbulent energy, $\mathcal{K}$, the cross helicity, $\mathcal{W}$, the turbulent coefficients, β_t and γ_t, contributions of the electromotive force, $|\beta_t \boldsymbol{J}|$ and $|\gamma_t \boldsymbol{\Omega}|$, the ratio $|\mathcal{W}|\,/\mathcal{K}$, and the electromotive force $E_M$are shown, respectively. The color notation is the same as Fig.4.5.

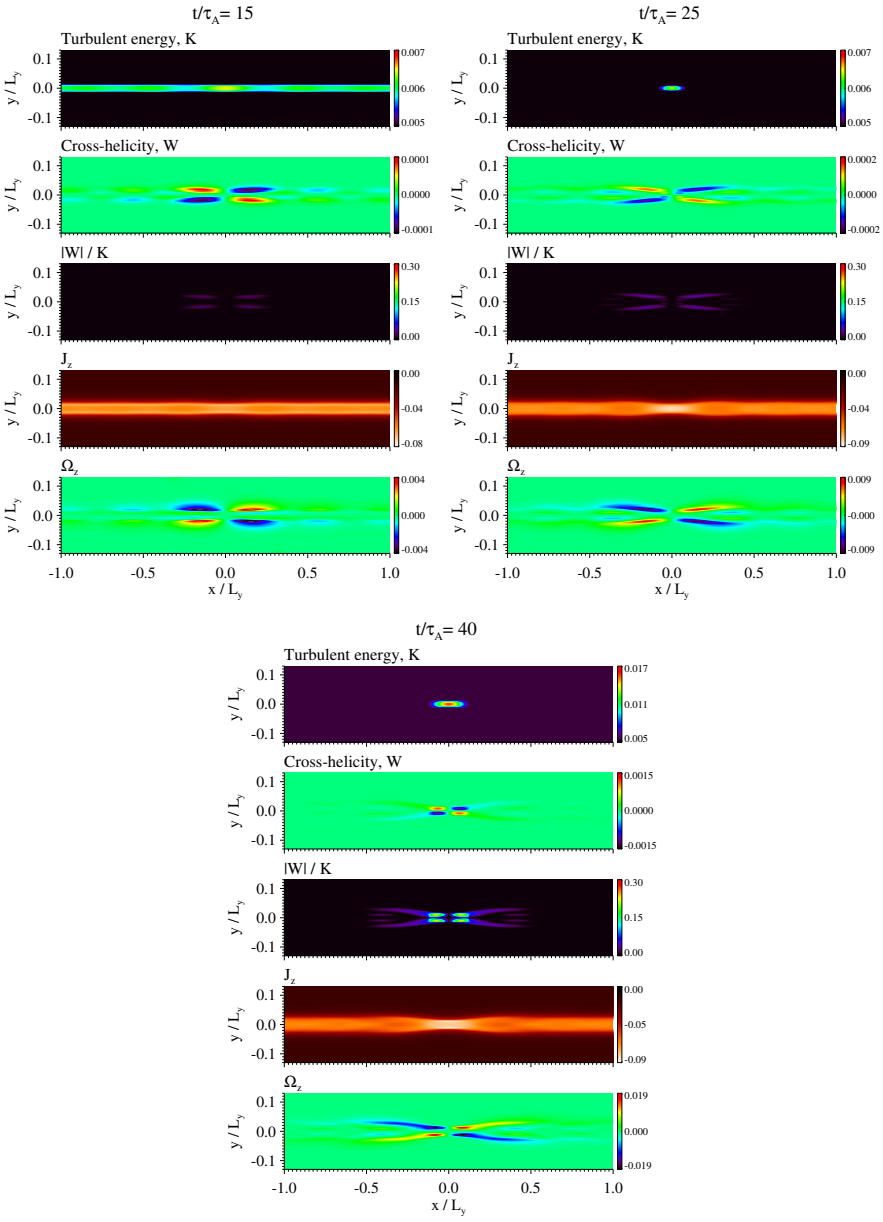

Figure 4.8: From top to bottom, spatial distributions of turbulent energy, $\mathcal{K}$, cross-helicity, $\mathcal{W}$, the ratio, $|\mathcal{W}|/\mathcal{K}$, z component of the electric current, J_z, and the vorticity, Ω_z, are shown. The upper left, the upper right, and the lower panels respectively show their snapshots at $t/\tau_A = 15$ (before the onset of fast reconnection), $t/\tau_A = 25$ (after the onset), and $t/\tau_A = 40$ (before the saturation).

fast magnetic reconnection is shown by the red solid line. In addition to the time profile of the maximum values, Fig. 4.8 shows the spatial distributions of turbulent energy, $\mathcal{K}$, cross-helicity, $\mathcal{W}$, the ratio, $|\mathcal{W}|/\mathcal{K}$, z component of the electric current, J_z, and the vorticity, Ω_z. The upper left, the upper right, and the lower panels in Fig. 4.8 respectively show the variables taken at $t/\tau_A = 15$ (before the onset of fast reconnection), t/τ_A (after the onset), and $t/\tau_A = 40$ (before the saturation of reconnection rate). Before the onset of fast reconnection ($t/\tau_A \lesssim 20$), the production of turbulent energy is almost equivalent to the dissipation rate in the current sheet for the case of $\tau/\tau_0 \sim 1$, and $\mathcal{K}$ remains small. On the other hand, $\mathcal{K}$ decreases outside the current sheet because the dissipation rate exceeds the production. This is seen in Fig. 4.8 in time $t/\tau_A = 15$, and the fluctuation of turbulent energy in the x direction is due to the initial perturbation of mean magnetic field given by Eq.(4.50). In this phase, both cross-helicity, $\mathcal{W}$, and vorticity, Ω_z, remain small, and the ratio $|\mathcal{W}|/\mathcal{K} = |C_\gamma \tau \mathcal{W}|/(C_\beta \tau \mathcal{K}) = |\gamma_t|/\beta_t \ll 1$. So, the β_t production term of equation (4.46), $-\langle \boldsymbol{v}' \times \boldsymbol{b}' \rangle \cdot \boldsymbol{J} \sim \beta_t \boldsymbol{J}^2$, dominates in the current sheet. As time passes, the inhomogeneity of the mean electric current becomes larger and the production rate exceeds dissipation rate, i.e., $\beta_t \boldsymbol{J}^2 > \epsilon_{\mathcal{K}}$. After the onset ($t/\tau_A > 20$), $\mathcal{K}$ is localized near $(x, y) \sim (0, 0)$ as shown by Fig. 4.8 in time $t/\tau_A = 25$. In this time, $|\mathcal{W}|/\mathcal{K} \ll 1$ and the β_t effect mainly contributes to the localization of $\mathcal{K}$. (After $\mathcal{W}$ increases, the cross-helicity transport effect contributes to the further location of $\mathcal{K}$. This point is discussed later.) Then, the increasing turbulent energy facilitates the effective diffusion of the mean magnetic field and triggers reconnection in macroscopic scale. Subsequently, topological change in the mean magnetic field and vorticity develops. The electric current and vorticity generate the cross-helicity. $|\gamma_t|/\beta_t$ begins to increase around $(x, y) \sim (0, 0)$ from time $t/\tau_A \sim 25$ (see the spatial distribution in Fig. 4.8 and the time profile in Fig. 4.7). Once $|\gamma_t|/\beta_t$ increases, $\mathcal{K}$ and $\mathcal{W}$ evolve according to both β_t and γ_t production effects. In this way, both turbulent energy and cross-helicity form in magnetic reconnection. $\mathcal{K}$ and $\mathcal{W}$ saturate at $t/\tau_A \sim 100$ and sustain their finite values. Note that in the diffusion current case (green line) the ratio $|\mathcal{W}|/\mathcal{K}$

becomes smaller than that of turbulent reconnection, and the electromotive force soon drops to zero.

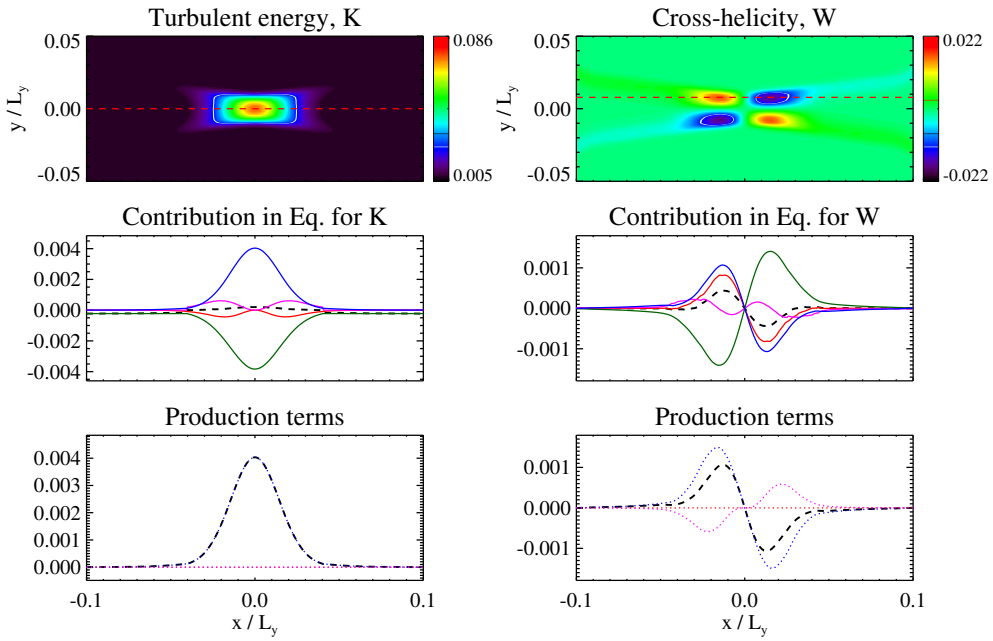

Figure 4.9: The upper contour plots show the spatial distributions of the turbulent energy $\mathcal{K}$ and the cross-helicity $\mathcal{W}$ near the magnetic neutral point in the case of $\tau/\tau_0 = 1.2$. Middle panels show contributions of Eq.(4.55) at $y = 0$ and Eq.(4.56) at $y = 0.01$. (Black-dashed= LHS, blue= production, purple= advection, red= transport, and dark-green= dissipation rate terms, respectively.) Bottom panels show a breakdown of the production term shown in the middle panels, Eqs.(4.57) and (4.58). (Black-dashed= total, blue-dotted= β_t related, and purple-dotted= γ_t related terms.) These snapshots are taken at time $t/\tau_A = 150$.

Figure 4.9 shows the spatial structure of $\mathcal{K}$ and $\mathcal{W}$ (upper contours) the detail contribution to produce and suppress them (middle and lower plots) at the saturated time, $t/\tau_A = 150$. Middle plots show the contribution of production, transport, advection, and dissipation terms at $y = 0$ for $\mathcal{K}$ and $y = 0.01$ for $\mathcal{W}$,

respectively. The color corresponds to the following equations:

$$\frac{\partial \mathcal{K}}{\partial t} = \underbrace{-\langle \boldsymbol{v}' \times \boldsymbol{b}' \rangle \cdot \boldsymbol{J}}_{\text{production}} \underbrace{+ (\boldsymbol{B} \cdot \boldsymbol{\nabla}) \mathcal{W}}_{\text{transport}} \underbrace{- (\boldsymbol{V} \cdot \boldsymbol{\nabla}) \mathcal{K}}_{\text{advection}} \underbrace{-\epsilon_{\mathcal{K}}}_{\text{dissipation rate}}, \tag{4.55}$$

$$\frac{\partial \mathcal{W}}{\partial t} = \underbrace{-\langle \boldsymbol{v}' \times \boldsymbol{b}' \rangle \cdot \boldsymbol{\Omega}}_{\text{production}} \underbrace{+ (\boldsymbol{B} \cdot \boldsymbol{\nabla}) \mathcal{K}}_{\text{transport}} \underbrace{- (\boldsymbol{V} \cdot \boldsymbol{\nabla}) \mathcal{W}}_{\text{advection}} \underbrace{-\epsilon_{\mathcal{W}}}_{\text{dissipation rate}}. \tag{4.56}$$

In the bottom plot, the breakdown of the production term is shown. The color follows β_t and γ_t effects:

$$\underbrace{-\langle \boldsymbol{v}' \times \boldsymbol{b}' \rangle \cdot \boldsymbol{J}}_{\mathcal{K} \text{ production}} = \underbrace{\beta_t \boldsymbol{J}^2}_{\beta_t \text{ effect}} \underbrace{-\gamma_t \boldsymbol{\Omega} \cdot \boldsymbol{J}}_{\gamma_t \text{ effect}}, \tag{4.57}$$

$$\underbrace{-\langle \boldsymbol{v}' \times \boldsymbol{b}' \rangle \cdot \boldsymbol{\Omega}}_{\mathcal{W} \text{ production}} = \underbrace{\beta_t \boldsymbol{J} \cdot \boldsymbol{\Omega}}_{\beta_t \text{ effect}} \underbrace{-\gamma_t \boldsymbol{\Omega}^2}_{\gamma_t \text{ effect}}. \tag{4.58}$$

The left panels of Fig. 4.9 explain turbulent energy. Turbulent energy is locally strengthened in the reconnection point as discussed above, and the effective magnetic field diffusivity increases (hereafter, turbulent diffusion region). This leads to the local enhancement of the internal energy and the resultant fast reconnection through slow-mode shocks. In the middle panel, $\partial \mathcal{K}/\partial t \sim 0$ (the black dashed line) and the turbulent energy is in a steady state. The production (blue line) balances with the dissipation rate (green), and the cross-helicity transport (red solid) balances with the advection (magenta solid). In the details of the production, the turbulent energy is produced by the β_t effect (see the blue dotted line in the bottom plot of Fig.4.9), and the γ_t effect (magenta dotted line) is absent in $y = 0$. The turbulent energy is supplied by the mean field energy, and this may be interpreted as energy cascade from larger scales. Imagine a fully-developed power spectra in the Fourier space. The energy in large scales is injected from mean field though the production term, and the energy cascades down to the smaller scale with the dissipation rate, $\epsilon_{\mathcal{K}}$. Then the turbulent energy is dissipated and converted into the internal energy. In the steady state, the injection energy and cascading energy bal-

ance. In addition, the turbulent energy produced near the X-point is advected by the mean plasma flow, and the advected energy is transported along the ambient magnetic field by the γ_t transport effect.

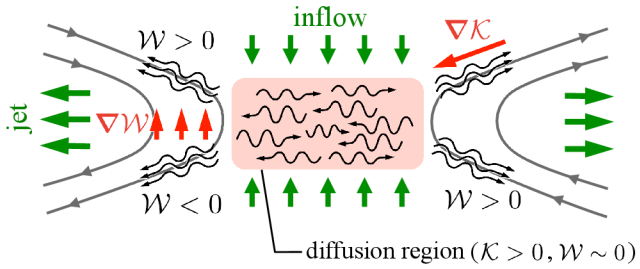

Figure 4.10: A schematic view of turbulent magnetic reconnection.

Then, how about the cross-helicity which is attributed to the γ_t transport coefficient? Right panels of Fig.4.9 explain the cross-helicity formation. A quadrupole cross-helicity distribution emerges around the turbulent diffusion region. From the middle and bottom panels, the cross-helicity is sustained by the balance among the production (blue solid), the advection (magenta solid), and the dissipation rate (green solid). The production consists of both β_t (blue dotted) and γ_t effects, and the cross-helicity forms in the region where the mean velocity shear becomes large. Physically, the distribution of cross-helicity may be interpreted by the propagation of Alfvén wave packets in addition to the interaction between the mean and turbulent fields. Figure 4.10 illustrates such a relation. In the vicinity of the neutral point, $\mathcal{K} > 0$ and $\mathcal{W} \sim 0$. With the viewpoint that the distribution of cross-helicity is related to the propagation of an Alfvén wave or asymmetry of the Alfvén wave packets, Alfvén waves equally propagate in both parallel and anti-parallel direction to the ambient magnetic field. In either edge of the diffusion region where $\mathcal{W} \neq 0$, Alfvén waves propagate outward along the ambient mag-

netic field. In Eq.(4.56), since the energy is large near the X-point, the direction of $\boldsymbol{\nabla}\mathcal{K}$ is always toward X-point. For example in the upper right region of Fig.4.10, the second transport term in Eq.(4.56) becomes positive, $+(\boldsymbol{B}\cdot\boldsymbol{\nabla})\mathcal{K} > 0$, and contributes to the generation of cross-helicity. Once the cross-helicity is generated, it begins to transport turbulence. In the left hand side reconnection jet of Fig.4.10, it can be considered that the wave energy decreases at the center of the jet through the Alfvén wave propagation. In this region, the second transport term in Eq.(4.56) becomes negative, $+(\boldsymbol{B}\cdot\boldsymbol{\nabla})\mathcal{W} < 0$, and the turbulent energy is suppressed before it is advected to the downstream region. The model suggests that the above transport effects participate in the dynamics in addition to the production and the dissipation processes.

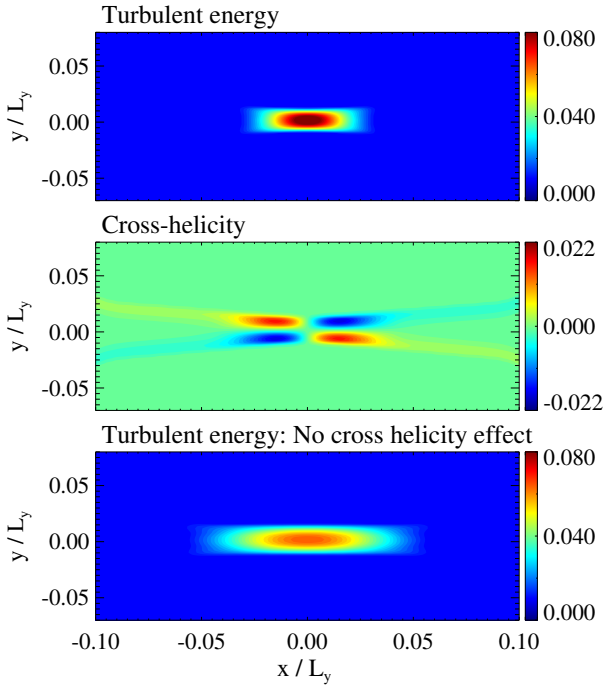

Figure 4.11: The top and middle panels respectively show turbulent energy and cross-helicity when the cross-helicity effect is included. The bottom panel shows turbulent energy in the case that cross-helicity is switched off (Eq.(4.47) is not solved).

We discuss the importance of such transport effects in an alternative way. Figure 4.11 shows the distributions of $\mathcal{K}$ and $\mathcal{W}$ with the cross-helicity effect (upper and middle contours), and the distribution of $\mathcal{K}$ without the cross-helicity effect. In the latter case, $\mathcal{W}$ is always set to zero and Eq.4.47 is switched-off. Without cross-helicity, the evolution of turbulent energy is determined by the β_t production, advection, and dissipation effects, and the transport effect is absent. In that case, the turbulent energy produced near the X-point is advected into the downstream region, and the turbulent diffusion region elongates compared to that with the cross-helicity effect. Then, such a spatial difference affects the reconnection speed. For example in Fig.4.5, the time profile of the reconnection speed (for example, see inflow Alfvén Mach number, $\mathcal{M}_A$) without cross-helicity effect is shown by a red-dashed line. As time passes, reconnection speed drops, suggesting that the turbulent transport plays a part in macroscopic dynamics.

§ 4.4 Summary

In this Chapter, the relationship between turbulence and reconnection dynamics was investigated from macroscopic viewpoint. The discussion is based on the assumption that fully-developed turbulence already exists in a current sheet, and the main interest is in the point that how turbulence affects macro scale reconnection dynamics. To investigate such turbulent current sheet dynamics, a MHD Reynolds-averaged simulation model was newly developed. In the model, equations of time evolution for turbulent variables (such as cross-helicity and turbulent kinetic energy) are solved in addition to the mean field MHD equations. Turbulent effects are included in Ohm's law as turbulent electromotive force, and turbulent and mean field quantities develop with interacting each other through it.

It is suggested that the initial current sheet develops in three ways, depending on the strength of turbulence: laminar reconnection, turbulent reconnection, and turbulent diffusion. In particular, the turbulent reconnection explosively converts the magnetic field energy into both kinetic bulk and thermal energy of plasmas. This turbulent-mediated reconnection develops, balancing the energy injection from mean field with the dissipation rate. In the onset phase, the balance breaks and the β_t effect begins to contribute to the localization of turbulent energy. As time passes, through the interaction between mean and fluctuating fields, the vorticity and the quadrupole cross-helicity distribution form near the turbulent diffusion region. In the steady state of turbulent diffusion region, the turbulent energy is mainly supplied from mean field (through the production term), and the production balances with the dissipation rate. If the cross-helicity is absent, the turbulent energy enhanced in the diffusion region is advected with the bulk flow and the diffusion region elongates. On the other hand with the presence of cross-helicity, the transport effect (arising from the inhomogeneity of cross-helicity along the magnetic field) suppresses turbulent diffusion and the diffusion region shrinks.

The main factor that enhances the reconnection rate is localization of the turbulent diffusion region as suggested by Petschek theory and the nonlinear MHD simulations, but it should be again emphasized that the present model could give an

alternative way of the fast reconnection process through turbulent effects, without assuming any unknown resistive model. Additionally, such turbulent-mediated process would, for example, play an important role in the region where there is a large gap between the overall and dissipation scales. It is not clear whether reconnection around the dissipation scale really develops into a huge-scale phenomenon. Assuming the existence of turbulence, however, the thickness of the current sheet may not necessarily become as thin as the dissipation scale, if $\beta_t > \eta$. Instead of dissipation-scale physics, turbulent diffusion could macroscopically change the topology of (mean) magnetic fields.

In this study, the model allows us to investigate the role of turbulence in the macroscale dynamics even for the high magnetic Reynolds number case. However, the results and suggestions are based on some assumptions, and we need to consider the limitations of the present model and the relation to other frameworks such as the DNS and the LES. Then, the model needs to be improved through mutual understanding with such frameworks and observations in future works. In what follows, the important assumptions of our present model and difference from previous turbulent reconnection studies are discussed.

(I) We injected the background turbulence only at $t = 0$. Once the simulation starts, $\mathcal{K}$ and $\mathcal{W}$ self-consistently develop without forcing background turbulence. On the other hand, the previous DNS studies usually force the background turbulence throughout simulations.

(Ⅱ) The feedback from the turbulent field is considered by the modeling of the electromotive force, i.e., Eq.(4.43).

(Ⅲ) The present model controls the property of turbulence (the dissipation rate, $\epsilon_{\mathcal{K}} = \mathcal{K}/\tau$) using the parameter, τ.

(I) We initially assume background turbulence, where $\mathcal{K} = 10^{-2}$ and $\mathcal{W} = 0$. Letting the characteristic velocity and magnetic field fluctuation $v' \sim b'$, the turbulent energy becomes $\mathcal{K} \sim v'^2$ and $v'/V_A \sim 0.1$. (Velocity is normalized by the

Alfvén velocity in the initial inflow regions.) Also, by the simple dimensional relation, the turbulent transport coefficient may be expressed as $\beta_t = C_\beta \tau \mathcal{K} \sim C_\beta v' l'$, where l' is the mixing length. In the case of fast turbulent reconnection, $\tau/\tau_0 \sim 1$, the coefficient is initially $\beta_t \sim 0.1$ (see Fig. 4.7). The mixing length and the time scale of turbulence can be estimated as $l'/\delta_c \sim 0.3$ and $\tau/\tau_A \sim 2$. So, the mixing length is shorter than the half thickness of the current sheet, and the time scale is shorter than that of mean field magnetic reconnection. The amplitude of fluctuations is in the same order as the preceding DNS reconnection studies that assume the pre-existing turbulence [51, 61]. One of major differences from the previous DNS studies is the energy injection of turbulence. We inject turbulence only at $t = 0$ and the turbulent quantities such as $\mathcal{K}$ and $\mathcal{W}$ develop through the interaction with the mean field, while the previous studies are forcing turbulence throughout the simulations. This difference may originate from the concept of turbulence. For example, the pre-existing major theory for turbulent reconnection [54] is based on the theory of homogeneous anisotropic turbulence [32]. The theory seems to have advantage to describe anisotropic turbulence in magnetized plasmas, but there is no energy injection from the larger scale (because the mean field is assumed to be homogeneous and there is no free energy in large scale). So, in order to obtain the reconnection rate based on the homogeneous anisotropic turbulence theory, one needs to inject ad-hoc turbulence continuously. On the other hand, our study is based on the inhomogeneous isotropic turbulence, and there is no need to assume the background turbulence. The turbulent energy is supplied by the inhomogeneity of mean field. However, the effect of anisotropy is not necessarily included in the present framework, and the results may not correctly describe the dynamics in the region where the magnetic field is strong. So far, no one knows the solution of anisotropic turbulence in the inhomogeneous system, but solving such a discrepancy is an important issue in the future turbulent reconnection study.

(II) In the concept of the Reynolds decomposition, the key point of modeling turbulence is how to consider the higher order correlation terms. In this study, we

discussed the turbulence effect in magnetic reconnection based on the modeling for the electromotive force [105]. As for the relation to DNSs, the model is examined by the Kolmogorov flow test problem, and the model constants are estimated by the DNS [36]. However whether it holds in the reconnection system or not is not so clear (for example, as discussed in (I), the model may not provide the correct result outside the current sheet, where strong magnetic field exists), and the model applicability should be also examined by the DNS for the reconnection system in future works.

As for another issue related to the present model, the effects other than β_t and γ_t effects may become important in more general cases. For example, if the guide magnetic field ($B_z \neq 0$) exists in the mean field (namely, the presence of the mean field current helicity, $\boldsymbol{J} \cdot \boldsymbol{B} \neq 0$), the mean current helicity would cascade down to (produce) the smaller scale current helicity. In this case, α_t dynamo effect may not be neglected.

(Ⅲ) We consider that turbulence is not simple fluctuations but has some signatures such as the energy cascade and the dissipation. In this study, the signatures are given by the constant parameter, τ, and we controlled the dissipation rate, $\epsilon_{\mathcal{K}} = \mathcal{K}/\tau$. Because we control the nature of turbulence, we need to consider this model constant carefully.

At least, the assumption for the spatiotemporally-independent constant τ may overestimate the turbulent diffusion in the case of $\tau/\tau_0 \gg 1$. For example in the case of $\tau/\tau_0 = 3.0$ (the turbulent diffusion case without magnetic reconnection), $\tau/\tau_A \sim 6$ and it is nearly equivalent to or faster than the mean current sheet evolution (see Fig. 4.7). Such an unnatural aspect implies the requirement of more accurate model. Noting the simple dimensional relation, $\beta_t \sim \tau\mathcal{K} \sim \mathcal{K}^2/\epsilon_{\mathcal{K}}$, one of such solutions may be to construct the equation for the dissipation rate, $\epsilon_{\mathcal{K}}$, which is known as $\mathcal{K}$–$\epsilon_{\mathcal{K}}$ model in hydrodynamic turbulence studies. The dissipation rate given by the Reynolds decomposition is expressed as Eq.(4.33), and the complex correlation of derivative of fluctuations may be directly derived by the Eq.(4.7)–(4.8). Alternatively, in the field of engineering, a simplified model is of-

ten used in accordance with an assumption that the dissipation rate should be large in the region where $\mathcal{K}$ is large. Based on this assumption, a dimensional analysis for Eq.(4.46) gives the equation of the dissipation rate for MHD turbulence [105].

Aside from the Reynolds-averaged model, considering the relation to other frameworks such as the DNS and the LES is important. Primarily, properties of turbulence should be determined through the non-linear wave couplings and other non-linear plasma dynamics. And the timescale of turbulence, as well as the dissipation rate of turbulent energy, should be determined according to the nonlinear dynamics. So far, we have no clear answer that what mechanism determines the property of turbulence in the reconnection system. It may be the parametric (decay/modulational) instability for large amplitude Alfvén waves [33, 42] or interactions among weak Alfvén waves [86]. It may be the non-linear couplings among eddies in the current sheet similar to the hydrodynamic turbulence. Or, it may be interpreted as a result of the production and coalescence of magnetic islands induced by the plasmoid instability [47, 3]. In either cases, the importance would be in the point that how do we grasp the coarse-grained macroscale dynamics, and the comparison between DNSs (LESs) and the turbulence model will be an interesting and essential issue.

CHAPTER 5
Concluding remarks

In many geophysical and astrophysical explosive phenomena, the fast energy release due to magnetic reconnection is considered to be indispensable as introduced in Chapter 1, and this dissertation focused on the relationship between turbulence and magnetic reconnection in high R_m plasmas with the strong nonlinearity. In high R_m plasmas, magnetic reconnection is mainly divided into two scales, i.e., MHD and kinetic scales, and the relation to turbulence for each of them was considered. In macroscale MHD reconnection, we discussed evolution of the turbulent current sheet based on the Reynolds-averaged model, and the relation between pre-existing turbulence and magnetic reconnection has been studied. In microscale kinetic reconnection, self-generation of Alfvénic fluctuations in reconnection jets was discussed based on the direct particle simulation and the linear analysis.

The macroscale discussions were given in Chapter 4. In MHD scale discussions, where the scale gap between the kinetic scale and the reconnection size is large, the reconnection study has had a difficulty in explaining the explosive energy release in a consistent manner. In particular, one of the most difficult problems has been to answer how to trigger fast reconnection in a thick MHD scale current sheet. In the laminar MHD current sheet, the possible element that causes magnetic field diffusion would be collisional resistivity, $\eta_{\rm collision}\boldsymbol{J}$, which is often negligible in a high magnetic Reynolds number. If the pre-existing fluctuations can be neglected, the current sheet slowly gets thinner according with the FKR tearing mode instability [26]. And in the nonlinear phase, it may finally reach kinetic scales through the plasmoid chains [93] and trigger fast reconnection. Such

an idea is interesting and theoretically seems to be robust to account for the fast energy release even in a high magnetic Reynolds number place. Aside from such ideas, this study sought another way to account for the fast reconnection problem in macroscale. We think that turbulence may give an alternative way of understanding this problem and discussed how the pre-existing turbulence affects the evolution of the current sheet based on the concept of Reynolds decomposition. With the presence of turbulence, the effect may be expressed as higher order correlation terms such as the electromotive force, $\langle \boldsymbol{v}' \times \boldsymbol{b}' \rangle_{\mathrm{MHD}}$. Based on the theory of inhomogeneous turbulence [105], we took into account the turbulent diffusion and the cross-helicity effects in the electromotive force as turbulent transport coefficients (β_t and γ_t), and developed a self-consistent Reynolds-averaged model for magnetic reconnection. The simulation results suggest that there are three ways for the current sheet evolution, depending on the strength of turbulence: the laminar Sweet–Parker reconnection, the Petschek reconnection induced by turbulence, and the turbulent diffusion without reconnection. Based on the viewpoint of fast magnetic reconnection in high R_m plasmas, it is interesting to consider where the above two reconnections are embedded in the previous reconnection studies (e.g., in Fig. 1.4). In the first case, the background turbulence becomes weak (because the dissipation rate exceeds the production rate of turbulence), and the laminar Sweet–Parker reconnection slowly evolves. On the other hand, the Sweet–Parker reconnection is shown to be unstable to the plasmoid instability by the DNS for high R_m plasmas [5], and the system will finally get the fast energy release. In the second case, where moderate turbulence is sustained by the balance between the production and the dissipation rate of turbulence, the turbulent current sheet develops into the Petschek type fast reconnection. This fast reconnection is achieved through the interaction between mean and turbulent fields. The diffusion region of this reconnection does not necessarily become as thin as the kinetic scale. Instead of kinetic physics, property of turbulence (such as production, transport and dissipation rate) could determine the width and the strength of the effective magnetic field diffusion. In this sense, turbulence may give account on the explosive energy

release by the Petschek reconnection without assuming any resistive model.

On the other hand, we still have problems to solve in determining turbulent transport coefficients as discussed in Chapter 4. One problem is the accuracy and the applicability to magnetic reconnection of this model. This point should be improved, taking clues from observations and other frameworks such as DNSs and LESs. Another problem is the relation to other turbulent reconnection ideas. For example, another theory [54] evaluated the reconnection rate based on the homogeneous anisotropic turbulence model [32] and implies that the turbulence transport coefficients may be determined by the anisotropic signature of turbulence. Of course, the scale and the basic concept of turbulence may differ, the detailed discussion for the discrepancy should be made in future works.

In the micro scale discussion in Chapter 2 and 3, we focused on the small scale-gap situation where kinetic effects should be taken into account. Initially, we assume a current sheet without turbulence, and the sheet width is about an ion inertial length. In kinetic scale, the fast reconnection could be triggered by the electron physics (such as the electron inertial [94] and the non-diagonal electron pressure effects [39]) even in the absence of pre-existing turbulence, and such a situation has been affirmed by experimental and in-situ observations for the small electron-scale diffusion region [49, 110]. Then, our interest is not in the diffusion region physics that triggers the fast reconnection in high R_m plasmas, but in the self-generated turbulence in non-linearly developed reconnection jets. In particular, we focused on the ion-scale dynamics and discussed how and when the Alfvénic fluctuations emerge owing to the inherent ingredients (plasma instabilities) in reconnection. Even if we start with a quiet current sheet without pre-existing fluctuations, the reconnection jet becomes turbulent when the jet size becomes $10^{1-2}\ \lambda_i$ ($t\Omega_{i*} \sim 10^2$) as reported by previous studies [59, 50, 2]. In the kinetic scale, the system has abundant sources, such as non-uniformity and pressure anisotropy, for plasma instabilities even inside the reconnection jet. Because the ion-scale reconnection jet is highly complex and nonuniform, we may not be able to attribute the origin of Alfvénic fluctuations in jets to a single cause. At

least, we addressed some issues on the PSBL dynamics and the global reconnection jet dynamics: the condition ($\beta_{i0} < 0.1$–0.2) and the possible mechanism that causes Alfvénic fluctuations in reconnection jets. The local analysis of the PSBL distribution function suggests that any Alfvénic fluctuations would decay by the kinetic damping effects, and the threshold for the development of Alfvénic fluctuations with $k\lambda_i > 1$ is in $\beta_{i0} < 0.1$–0.2. Additionally, we discussed the origin of Alfvénic fluctuations by global viewpoint. We considered the effect of anisotropy in addition to the previous isotropic analysis, and confirmed that the ion pressure anisotropy is an essential ingredient to account for the non-local instability in reconnection jet.

It is interesting to consider the region where such self-generated turbulence by kinetic reconnection becomes important. For example in magnetosphere, where kinetic effects should be taken into account almost everywhere, turbulence has attracted much attention [111]. The turbulence may become important to explain the magnetospheric convection (induced by turbulent transport), particle heating (dissipation of electromagnetic field energy through turbulence), and particle acceleration (power law spectrum by the stochastic scattering process in turbulence), etc.[1] As was briefly mentioned in Chapter 1, turbulence is often observed in the region where reconnection takes place such as magnetopause [35] and the magnetotail [45][22], and reconnection is regarded as one of the important sources of turbulence. (As another example, the penetration of solar wind turbulence [64][75] may be an important clue.) Then, the above self-generated turbulence in the ion-scale reconnection is considered to play a part in the generation of turbulence in magnetosphere. On the other hand, it should be noted that this study was limited in the two-dimensional anti-parallel magnetic field configuration. The self-generation mechanism would strongly depends on the situation where reconnection takes place (such as the plasma beta, the guide field, [2] the kind of plasmas),

[1] For example, the ion particle acceleration remains one of major outstanding problems in magnetospheric physics. In the magnetotail region, high energy ions (up to 10^6 eV) are often observed [66], but it is known that MeV ions cannot be explained by the simple electrostatic acceleration in magnetic reconnection.

[2] For example, in the case of guide field reconnection, it has been shown that, a secondary

and the study on the self-generated mechanism in kinetic reconnection is still developing. In future works, it will be important to investigate the self-generating mechanism for many other cases and consider how the turbulence affects other outstanding problems such as the particle acceleration.

electron tearing instability takes place in reconnection separatrix regions and the turbulent reconnection outflow develops [16].

CHAPTER A

Nonlinear behavior of the streaming current sheet in anisotropic plasmas

In Chapter 3, the linear stability of the streaming current sheet was discussed in terms of reconnection jet dynamics, and it is suggested that both anisotropy and non-uniformity are important factors to explain the non-local mode in jets. Here, we discuss nonlinear evolution of the streaming current sheet in anisotropic plasmas. Because there is no mechanism to produce PSBL ion beams in the following system (setup), only the nonlinear behavior of the streaming current sheet is briefly investigated.

Model and setup

The simulation model adopted here is the hybrid code shown in Chapter 2. One may think that solving the anisotropic MHD equations with the double adiabatic equations [15] may be a better strategy to discuss the nonlinear nature of the streaming current sheet. However, the double adiabatic model has a difficult problem in solving the singular point ($|\boldsymbol{B}| \sim 0$). Thus the hybrid model is used to avoid such difficulties.

Initially, the anti-parallel magnetic field is given by

$$\boldsymbol{B} = \boldsymbol{e}_x B_0 \left[\tanh\left(\frac{y}{\delta_{\rm jet}}\right) - \tanh\left(\frac{y - 0.5L_y}{\delta_{\rm jet}}\right) - 1 \right], \tag{A.1}$$

and two current sheets are located at $y = 0$ and $0.5L_y$ as shown in Fig. A.1. L_y is the system size in the y-direction, and the spatiotemporal resolution are

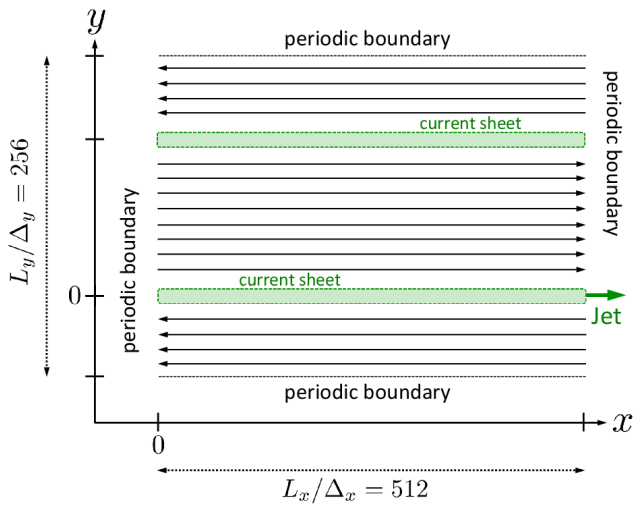

Figure A.1: A schematic view of the setup and boundary conditions

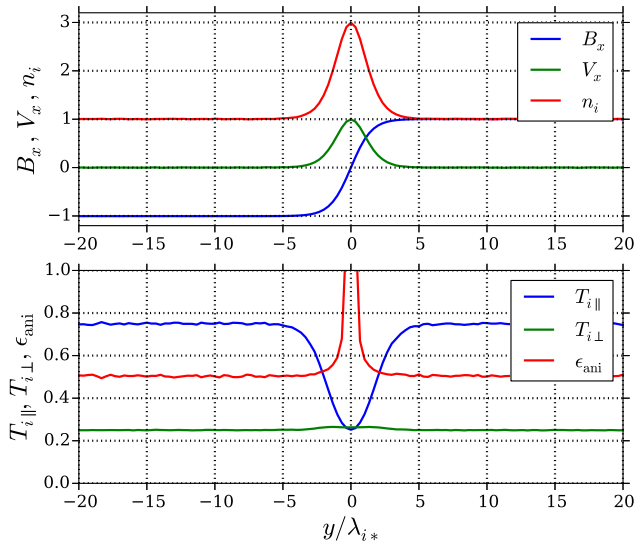

Figure A.2: A setup of the hybrid simulation in the case of $\beta_{i0} = 0.5$, $V_{\rm jet} = 1.0$, $\epsilon_{\rm ani} = 0.5$, and $\delta_{\rm jet} = \delta_{\rm harris} = 1.5\ \lambda_{i*}$. The cross-sectional quantities in the y-direction are shown. They are averaged in the x-direction, and only the lower current sheet is shown.

respectively $\Delta_t \Omega_{i*} = 10^{-2}$ and $\Delta_x = \lambda_{i*}/3.0$. Boundary conditions in both x- and y-directions are periodic. The number of super-particles in each cell outside the current sheets are fixed to $N_{\rm cell} = 200$. The ion temperatures in the lobe and the neutral sheet are assumed to be identical for the purpose of simplicity in giving the ion pressure anisotropy. The anisotropic Harris sheet equilibrium is sustained by the pressure balance perpendicular to the magnetic field, and the thermal velocity for each ion, $v_{i,th}$, is given by Maxwellian defined by $T_{i,\perp}$. The x component of the ion velocity which includes the bulk jet and the pressure anisotropy is given by

$$v_{ix}(y_i) = v_{i,th} \left\{ 1 + \left[\frac{|\boldsymbol{B}(y_i)|^2 (1 - \epsilon_{\rm ani})}{n_i(y_i) T_{i,\perp}} \right]^{1/2} \right\} + V_0(y_i) \tag{A.2}$$

where $\epsilon_{\rm ani} = 1 - n_i \left(T_{i,\parallel} - T_{i,\perp} \right) / |\boldsymbol{B}|^2$ and y_i is the particle location for each ion. The bulk velocity $V_0(y_i)$ is given by Eq.(3.20) in Chapter 3, and the plasma flow is added only in the lower current sheet. In the following discussions, $\epsilon_{\rm ani}$ is given as a constant value in space. Because $T_{i,\perp}$ is constant in space, $T_{i,\parallel}(y)$ is chosen so that $\epsilon_{\rm ani}$ becomes constant as shown in Fig.A.2. The simulation parameters are shown in Table A.1. Basically, the parameters are chosen in association with the ion-scale reconnection jet shown by nonlinear simulations.

Table A.1: Simulation parameters for the streaming current sheet

Figure	β_{i0}	$\delta_{\rm jet}/\lambda_{i*}$	$\epsilon_{\rm ani}$	$V_{\rm jet}$	$L_x \times L_y$ (Δ_x)	$n_{\rm jet}/n_{\rm lobe}$
Fig. A.2	0.5	1.5	0.5	1.0	512×256	2.0
Fig. A.3(a)	0.5	1.5	0.1–1.0	1.0	512×256	2.0
Fig. A.3(b)	0.5	2.0	0.1–1.0	1.0	512×256	2.0
Fig. A.3(c)	0.5	2.5	0.1–1.0	1.0	512×256	2.0

To discuss the nonlinear property of the global mode in anisotropic reconnec-

tion jet, only two points are checked: (1) how does the saturation level depend on the pressure anisotropy, and (2) does the kink mode really grow in the nonlinear system beyond the symmetric mode.

The saturation level and the dominant mode in the anisotropic jet

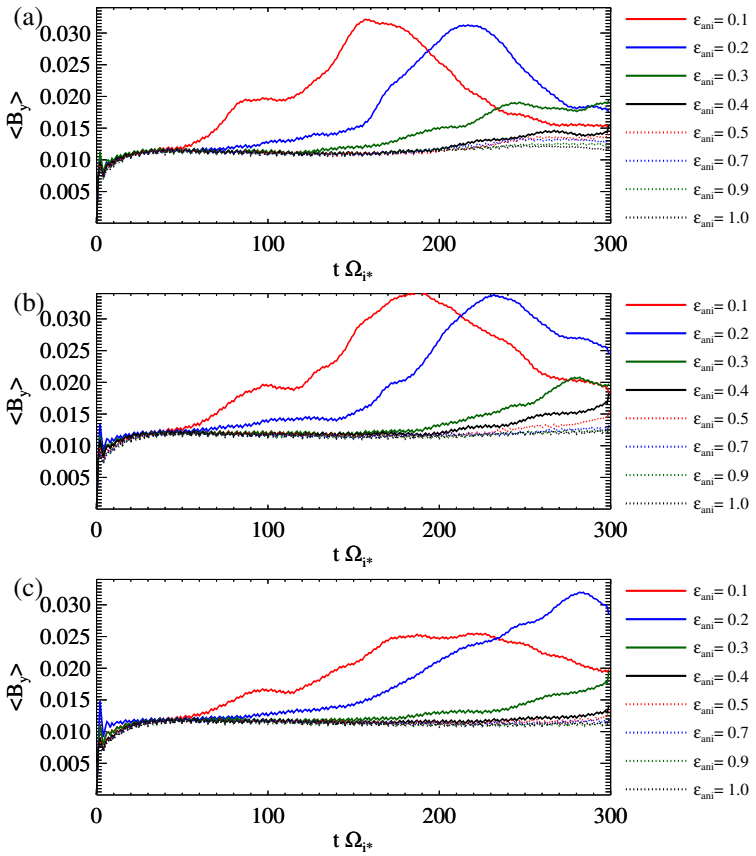

Figure A.3: The time history of $\langle B_y \rangle$ for (a) $\delta_{\rm jet}/\lambda_{i*} = 1.5$, (b) 2.0, and (c) 2.5 cases. In each case, time profile of $\langle B_y \rangle$ is shown for different anisotropy, $\epsilon_{\rm ani} = 0.1$–1.0.

Here, the saturation level is examined using the current crossing component,

B_y. We use the following integrated value,

$$\langle B_y \rangle \equiv \frac{1}{2\delta_{\rm jet} L_x} \int_0^{L_x} dx \int_{-\delta_{\rm jet}}^{+\delta_{\rm jet}} dy \, |B_y(x,y)| \, . \tag{A.3}$$

Figure A.3(a)–(c) show the time history of $\langle B_y \rangle$ for different sheet widths ($\delta_{\rm jet}/\lambda_{i*} =$ 1.5, 2.0, and 2.5 cases, respectively). The initial background pressure anisotropy is denoted by the line-style and the color shown in the right-hand-side of the figure. Among all cases, the baseline $\langle B_y \rangle \sim 0.01$ is due to the background Alfvén waves produced by the thermal fluctuation. The current sheet instability clearly appears as the anisotropic increases in the time scale focused in the present study, $t\Omega_i \sim \mathcal{O}(10^{1-2})$.

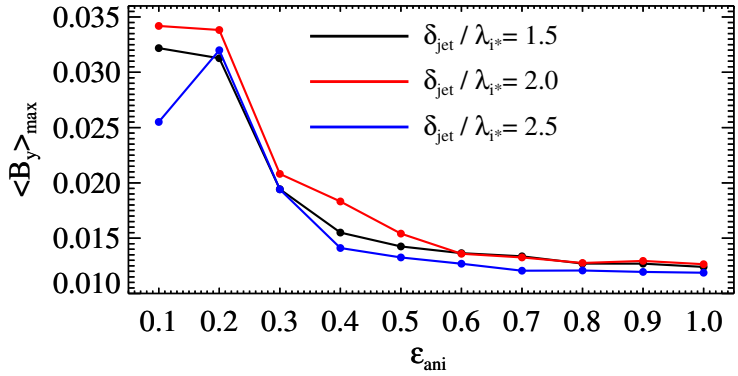

Figure A.4: The maximum values of $\langle B_y \rangle$ in time are shown with different sheet widths and the anisotropic parameters.

Figure A.4 shows the maximum value of $\langle B_y \rangle$ in time. The maximum value does not depend on the width of the current sheet, suggesting that the Hall effect seems to be irrelevant to the saturation. On the other hand, it is sensitive to the pressure anisotropy. The saturation level becomes large in $\epsilon_{\rm ani} < 0.5$, the kink type mode dominates there. Figure A.5 shows the ion density in the x-y plane. From top to bottom, the ion density and magnetic field lines for the cases of (a) $\epsilon_{\rm ani} = 0.1$, (b) $\epsilon_{\rm ani} = 0.2$, and $\epsilon_{\rm ani} = 1.0$ are shown at the time $t\Omega_{i*} = 150$.

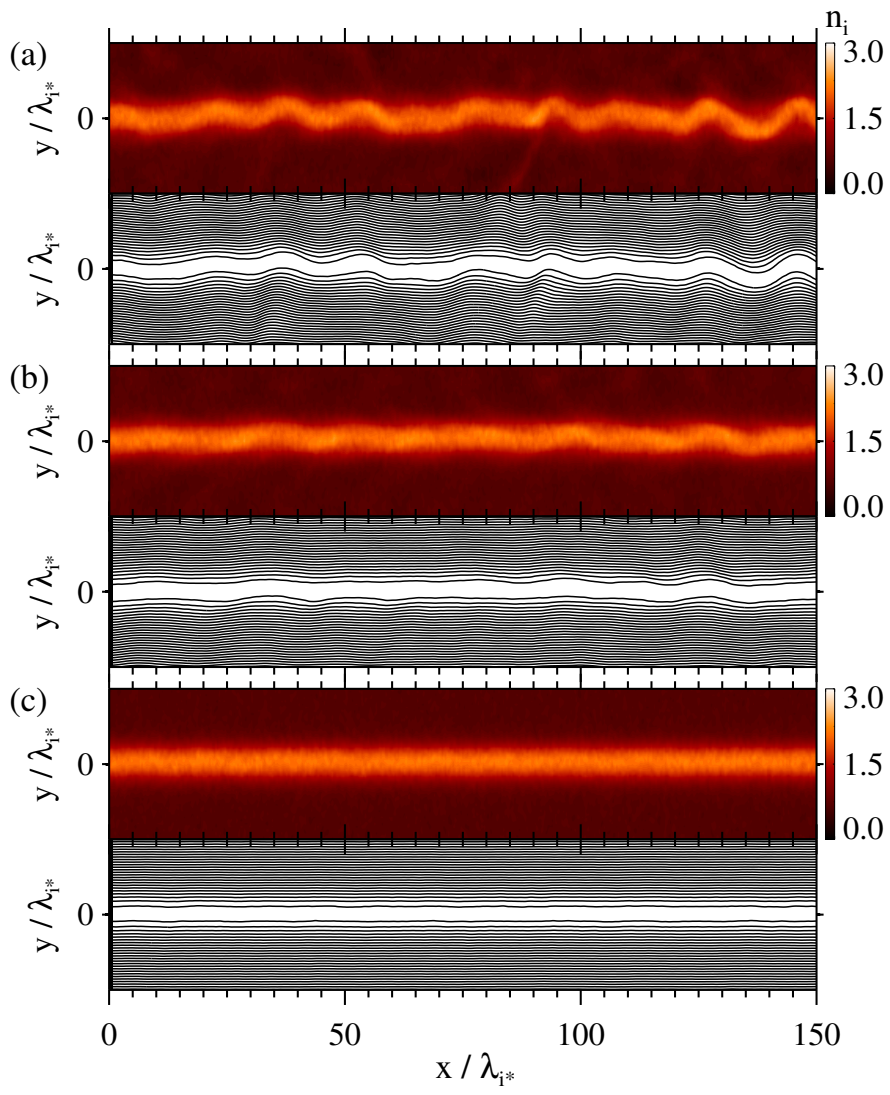

Figure A.5: Ion density and magnetic field lines for (a) $\epsilon_{\rm ani} = 0.1$, (b) $\epsilon_{\rm ani} = 0.2$, and (c) $\epsilon_{\rm ani} = 1.0$ cases at the time $t\Omega_{i*} = 150$. The width of the initial jet is $\delta_{\rm jet}/\lambda_{i*} = 1.5$ in all these cases.

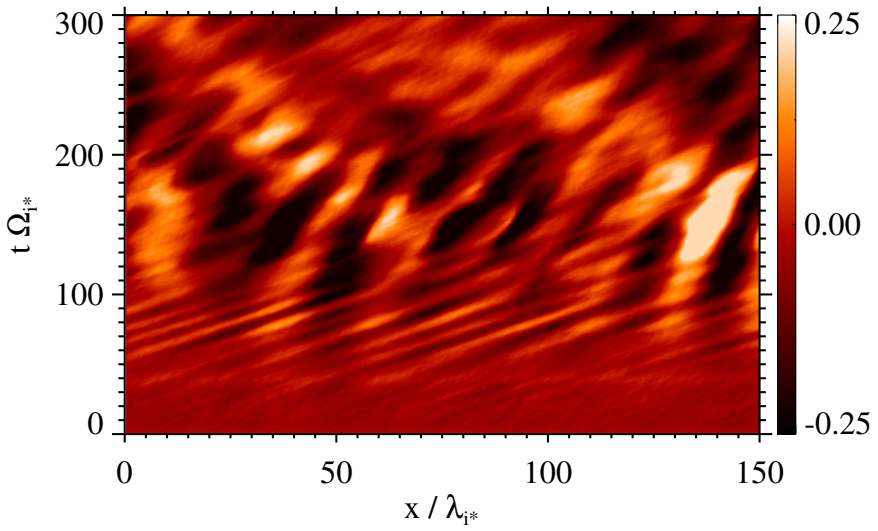

Figure A.6: The spatiotemporal diagram for $B_x(x,t)$ at $y/\lambda_{i*} = 0$.

Figure A.6 shows the time evolution of the streaming current sheet in the most unstable case, $\epsilon_{\rm ani} = 0.1$ and $\delta_{\rm jet}/\lambda_{i*} = 1.5$. This figure shows the spatiotemporal distribution of $B_x(x,t)$ in $y/\lambda_{i*} = 0$. In the linear state ($t\Omega_{i*} \sim$ 50–100), the kink mode appears in the wavelength $\sim 10^{0-1}\delta_{\rm jet}$. Subsequently, the system evolves into nonlinear phase. The mode quickly cascades inversely and generates longer wavelength modes with larger amplitude. In future works, the detail analysis should be done through the comparison with the linear Vlasov analysis for the non-uniform jet.

CHAPTER B

Some theoretical notes

Yokoi–Hoshino reconnection model with turbulent transport effects

Based on the Reynolds decomposition, Yokoi and Hoshino has made a theoretical prediction on turbulent magnetic reconnection [101]. Here, their ideas are briefly summarized. They considered the steady state reconnection, whose inflow Alfvén Mach number (reconnection rate) is modified by the presence of β_t (turbulent diffusion) and γ_t (cross-helicity) effects. The reconnection rate predicts that the reconnection would be enhanced as the cross-helicity effect becomes larger.

The basic equations are mean field equations which include the turbulent transport effects, β_t and γ_t:

$$\frac{\partial \boldsymbol{\Omega}}{\partial t} = \left[\left(\boldsymbol{V} - \frac{\gamma_t}{\beta_t} \boldsymbol{B} \right) \times \boldsymbol{\Omega} + \frac{7}{5} \beta_t \boldsymbol{\nabla}^2 \left(\boldsymbol{V} - \frac{\gamma_t}{\beta_t} \boldsymbol{B} \right) + (\boldsymbol{E} + \boldsymbol{V} \times \boldsymbol{B}) \right], \quad \text{(B.1)}$$

$$\frac{\partial \boldsymbol{B}}{\partial t} = \left[\boldsymbol{V} \times \boldsymbol{B} - \beta_t \left(\boldsymbol{\nabla} \times \boldsymbol{B} \right) + \gamma_t \left(\boldsymbol{\nabla} \times \boldsymbol{V} \right) \right], \quad \text{(B.2)}$$

where Eq.(B.1) is the rotation form of Eq.(4.4). In addition, they considered modifications of mean fields ($\boldsymbol{V}$ and $\boldsymbol{B}$) to discuss how the mean field could be modified by the turbulent transport effects (β_t and γ_t effects):

$$\boldsymbol{V} = \boldsymbol{V}_0 + \tilde{\boldsymbol{V}}, \quad \text{(B.3)}$$

$$\boldsymbol{B} = \boldsymbol{B}_0 + \tilde{\boldsymbol{B}}, \quad \text{(B.4)}$$

where $\tilde{\boldsymbol{V}}$ and $\tilde{\boldsymbol{B}}$ are modified mean fields. Substituting this into Eq.(B.1) and

(B.2) gives following equations for modified mean fields:

$$\frac{\partial \tilde{\boldsymbol{\Omega}}}{\partial t} = \boldsymbol{\nabla} \times \left[\left(\tilde{\boldsymbol{V}} - \frac{\gamma_t}{\beta_t} \boldsymbol{B} \right) \times \boldsymbol{\Omega}_0 + \frac{7}{5} \beta_t \boldsymbol{\nabla}^2 \left(\tilde{\boldsymbol{V}} - \frac{\gamma_t}{\beta_t} \boldsymbol{B} \right) \right], \tag{B.5}$$

$$\frac{\partial \tilde{\boldsymbol{B}}}{\partial t} = \boldsymbol{\nabla} \times \left[\boldsymbol{V} \times \tilde{\boldsymbol{B}} - \beta_t \left(\boldsymbol{\nabla} \times \tilde{\boldsymbol{B}} \right) - \gamma_t \left(\boldsymbol{\nabla} \times \tilde{\boldsymbol{V}} \right) \right]. \tag{B.6}$$

In the steady state, one notes that there are special solutions for $\tilde{\boldsymbol{V}}$ and $\tilde{\boldsymbol{B}}$

$$\tilde{\boldsymbol{V}} = \frac{\gamma_t}{\beta_t} \boldsymbol{B}, \tag{B.7}$$

$$\tilde{\boldsymbol{B}} = \frac{\gamma_t}{\beta_t} \boldsymbol{V}. \tag{B.8}$$

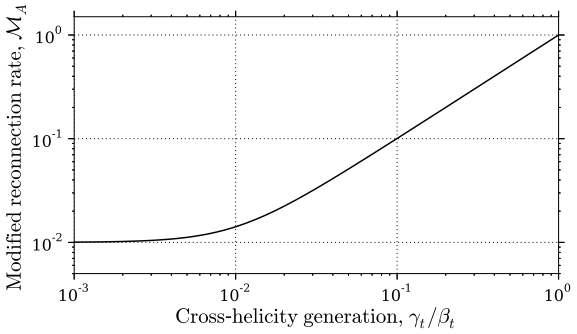

Figure B.1: Reconnection rate (inflowing Alfvén Mach number) modified by the cross-helicity effect, $\mathcal{M}_A$.

Since $\gamma_t/\beta_t \propto \mathcal{K}/\mathcal{W}$, these relations suggest that generation of cross-helicity could change the mean field. They considered that such turbulent effect could change the inflow conditions. Defining the unmodified reconnection rate (inflowing Alfvén Mach number) as $\mathcal{M}_{A0} \equiv \boldsymbol{V}_0/V_A$, the resultant reconnection rate mod-

ified by β_t and γ_t effects can be calculated as

$$\mathcal{M}_A = \frac{\boldsymbol{V}_0 + \tilde{\boldsymbol{V}}}{V_A} = \left(\frac{\mathcal{M}_{A0}^2 + \left(\frac{\gamma_t}{\beta_t}\right)^2}{1 + \mathcal{M}_{A0}^2 \left(\frac{\gamma_t}{\beta_t}\right)^2} \right)^{1/2} , \tag{B.9}$$

where Eqs.(B.3)–(B.4) and (B.7)–(B.8) are used and $\boldsymbol{V}_0 \cdot \boldsymbol{B}_0 = 0$ is assumed in the inflow region, here. The modified reconnection rate is shown in Fig.B.1, and it is shown that the cross-helicity generation changes the structure of the inflow region and enhances the resultant reconnection rate.

CHAPTER C
Numerical Methods

Normalization manner and some test problems for the simulation model adopted in this dissertation (an electromagnetic hybrid code, a plasma dispersion solver, and a Reynolds-averaged MHD model) are briefly summarized for references.

§ C.1 Normalization

An electromagnetic hybrid model

Basic equations consist of the equation of motion of ions, Faraday's law, generalized Ohm's law, and Ampere's law in CGS Gauss unit:

$$m_{\mathrm{i}}\frac{d\boldsymbol{v}_{\mathrm{i}}}{dt} = q_{\mathrm{i}}\left(\boldsymbol{E} + \frac{\boldsymbol{v}_{\mathrm{i}}\times\boldsymbol{B}}{c}\right), \tag{C.1}$$

$$\frac{d\boldsymbol{x}_{\mathrm{i}}}{dt} = \boldsymbol{v}_{\mathrm{i}}, \tag{C.2}$$

$$\frac{\partial\boldsymbol{B}}{\partial t} = -c\boldsymbol{\nabla}\times\boldsymbol{E}, \tag{C.3}$$

$$\boldsymbol{E} = -\frac{1}{en_{\mathrm{i}}}\boldsymbol{\nabla}p_{\mathrm{e}} - \frac{\boldsymbol{V}_{\mathrm{e}}\times\boldsymbol{B}}{c} + \lambda_r\boldsymbol{\nabla}\times\boldsymbol{B}, \tag{C.4}$$

$$\boldsymbol{V}_{\mathrm{e}} = \boldsymbol{V}_{\mathrm{i}} - \frac{c}{4\pi en_{\mathrm{i}}}\boldsymbol{\nabla}\times\boldsymbol{B}. \tag{C.5}$$

$$n_i = \int_{-\infty}^{\infty} f_i(\boldsymbol{x}_i,\boldsymbol{v}_i,t)d\boldsymbol{v}_i, \tag{C.6}$$

$$\boldsymbol{V}_i = \frac{1}{n_i}\int_{-\infty}^{\infty}\boldsymbol{v}_i f_i(\boldsymbol{x}_i,\boldsymbol{v}_i,t)d\boldsymbol{v}_i. \tag{C.7}$$

The velocity, the time scale, and the spatial scale are respectively normalized by Alfvén velocity, ion cyclotron frequency, and ion inertial length:

$$m_{\rm i}\frac{d\boldsymbol{v}_{\rm i}}{dt} = q_{\rm i}\left(\boldsymbol{E} + \boldsymbol{v}_{\rm i}\times\boldsymbol{B}\right), \tag{C.8}$$

$$\frac{d\boldsymbol{x}_{\rm i}}{dt} = \boldsymbol{v}_{\rm i}, \tag{C.9}$$

$$\frac{\partial\boldsymbol{B}}{\partial t} = -\boldsymbol{\nabla}\times\boldsymbol{E}, \tag{C.10}$$

$$\boldsymbol{E} = -\frac{1}{n_{\rm i}}\boldsymbol{\nabla}p_{\rm e} - \boldsymbol{V}_{\rm e}\times\boldsymbol{B} + \lambda_r\boldsymbol{\nabla}\times\boldsymbol{B}, \tag{C.11}$$

$$\boldsymbol{V}_{\rm e} = \boldsymbol{V}_{\rm i} - \frac{1}{n_{\rm i}}\boldsymbol{\nabla}\times\boldsymbol{B}, \tag{C.12}$$

where

$$\begin{aligned} m_i/m_p \to 1,\ \ q_i/e \to q_i,\ \ \Omega_{\rm i*}t \to t,\ \ \lambda_{\rm i*}\boldsymbol{\nabla} \to \boldsymbol{\nabla}, \\ \boldsymbol{x}/\lambda_{\rm i*} \to \boldsymbol{x},\ \ \boldsymbol{v}/V_{A*} \to \boldsymbol{v}, \\ \boldsymbol{B}/B_* \to \boldsymbol{B},\ \ c\boldsymbol{E}/(V_{A*}B_*) \to \boldsymbol{E},\ \ \boldsymbol{V}_{\rm i}/V_{A*} \to \boldsymbol{V}_{\rm i},\ \ \boldsymbol{V}_{\rm e}/V_{A*} \to \boldsymbol{V}_{\rm e}, \\ n_{\rm i}/n_* \to n_{\rm i},\ \ p_{\rm e}/(m_p n_* V_{A*}^2) \to p_{\rm e},\ \ \lambda_r/\lambda_{\rm i*} \to \lambda_r. \end{aligned} \tag{C.13}$$

where m_p is proton mass. The subscript $\_*$ stands for the normalization constant. $\lambda_r = \eta c^2/(4\pi V_{A*})$ is the resistive length and its resistivity is due to the electron-ion interactions which can not be considered in ion-particle and electron-fluid hybrid models.

A plasma dispersion solver

In this paper, velocity distribution functions for particles are assumed to consist of superposition of multicomponents,

$$f_{\rm i} = \frac{n_{\rm i}}{\left(2\pi\right)^{3/2}\sigma_{\rm i}v_{{\rm i},th}^3}\exp\left[-\frac{\left(v_{\rm i,\parallel} - V_{\rm i}\right)^2}{2v_{{\rm i},th}^2} - \frac{v_{\rm i,\perp}^2}{2\sigma_{\rm i}v_{{\rm i},th}^2}\right]. \tag{C.14}$$

The subscript i represents ions. $\sigma_{\rm i} \equiv T_{\rm i,\perp}/T_{\rm i,\parallel}$ determines temperature anisotropy for each ion component. $v_{{\rm i},th}$ is the thermal velocity parallel to the magnetic field and defined by $v_{{\rm i},th} \equiv \left(T_{\rm i,\parallel}/m_{\rm i}\right)^{1/2}$. $n_{\rm i}$ and $V_{\rm i}$ are number density and bulk velocity, respectively.

Then, the parallel propagation mode is discussed:

$$\frac{k^2c^2}{\omega^2} = 1 + \sum_j \frac{\omega_{p,j}^2}{\omega^2}\left[\zeta_j^{(0)}\mathcal{Z}(\zeta_j^{(0)}) + (1-\sigma_j)\,\frac{\mathcal{Z}'(\zeta_j^{(1)})}{2}\right], \tag{C.15}$$

where $\zeta_j^{(n)} = \left(\omega - kV_j + n\Omega_j\right) / \left(\sqrt{2}kv_{j,th}\right)$ and $\mathcal{Z}(\zeta)$ is a plasma dispersion function [1]. The spatial and time scales are normalized by the ion inertial length

[1] The plasma dispersion function can be expressed as

$$\mathcal{Z}(\zeta) = \frac{1}{\sqrt{\pi}}\int_{-\infty}^{\infty}\frac{\exp\left(-z^2\right)}{z-\zeta}dz, \tag{C.16}$$

In order to avoid singularity by Landau and cyclotron resonance, we used the series expansion method. The formulations are summarized as follows:

$$\mathcal{Z}(\zeta) = \begin{cases} \text{If } \cos\left[\dfrac{2\pi}{h}\Re(\zeta)\right] \le 0, \\ \quad \dfrac{h}{\pi}\left\{\displaystyle\sum_{n=1}^{M}\left[e^{-n^2h^2}\frac{2\zeta}{n^2h^2-\zeta^2}\right] - \frac{1}{\zeta}\right\} + i\sqrt{\pi}e^{-\zeta^2}A_0(\zeta), \\ \\ \text{else if } \cos\left[\dfrac{2\pi}{h}\Re(\zeta)\right] > 0, \\ \quad \dfrac{h}{\pi}\left\{\displaystyle\sum_{n=1}^{M}\left[e^{-(n-1/2)^2h^2}\frac{2\zeta}{(n-1/2)^2h^2-\zeta^2}\right]\right\} + i\sqrt{\pi}e^{-\zeta^2}A_1(\zeta), \end{cases}$$

where

$$A_0(\zeta) = \begin{cases} 0 \\ \dfrac{2}{1-e^{-2\pi i\zeta/h}} \\ 2 \end{cases}, \quad A_1(\zeta) = \begin{cases} 0 & (\Im(\zeta) > \pi/h) \\ \dfrac{2}{1+e^{-2\pi i\zeta/h}} & (|\Im(\zeta)| < \pi/h) \\ 2 & (\Im(\zeta) < -\pi/h) \end{cases}, \tag{C.17}$$

and the ion cyclotron frequency.

$$k^2 = \omega^2 + \sum_j m_j^{-1} \left[\zeta_j^{(0)} \mathcal{Z}(\zeta_j^{(0)}) + (1 - \sigma_j) \frac{\mathcal{Z}'(\zeta_j^{(1)})}{2} \right], \tag{C.18}$$

where

$$\begin{aligned} \omega/\Omega_{\mathrm{i}*} \to \omega, \;\; k\lambda_{\mathrm{i}*} \to k, \;\; v_j/V_{A*} \to v_j, \\ n_j/n_* \to n_j, \;\; m_j/m_{\mathrm{i}*} \to m_j. \end{aligned} \tag{C.19}$$

A Reynolds-averaged model

Mean field equations are assumed to be the resistive MHD equation including the turbulence transport effect in the induction equation. The basic equations are normalized in Alfvén unit, and the normalized equations are shown in Eq.(4.38)–(4.49), where

$$t/T_* \to t, \;\; L_* \boldsymbol{\nabla} \to \boldsymbol{\nabla} \tag{C.20}$$

$$\rho/\rho_* \to \rho, \;\; \boldsymbol{v}/V_{A*} \to \boldsymbol{v}, \;\; \boldsymbol{b}/B_* \to \boldsymbol{b}, \tag{C.21}$$

$$\frac{p}{\rho_* V_{A*}^2} \to p, \;\; \frac{\boldsymbol{e}c}{B_* V_{A*}} \to \boldsymbol{e}, \;\; \frac{\eta c^2}{4\pi V_{A*} L_*} \to \eta. \tag{C.22}$$

The subscript $_*$ stands for the normalization constant, and

$$V_{A*} = \frac{L_*}{T_*} = \frac{B_*}{\sqrt{4\pi\rho_*}}. \tag{C.23}$$

Since the equations for $\mathcal{K}$ and $\mathcal{W}$ are derived by assuming the incompressible condition $\rho/\rho_* = 1$, they are respectively expressed as $\mathcal{K} = \mathcal{K}/V_{A*}^2$ and $\mathcal{W} = \mathcal{W}/(B_* V_{A*})$.

and $h = 0.484375$, $M = 14$ are adopt as [96].

§ C.2 Some test problems

The electromagnetic hybrid model

Figure C.1 shows plasma wave dispersions for parallel propagating electromagnetic mode; whistler ($\omega > 0$) and ion-cyclotron ($\omega < 0$) modes. Test parameters are given by the ion temperature $T_i = 10^{-4}$, the electron temperature $T_e = 0.0$, the total number of grids $N_x = 512$, the time interval $\Delta_t = 0.01\ \Omega_i^{-1}$, the total time-steps $= 8192$, and the grid interval $\Delta_x = \lambda_i/3$.

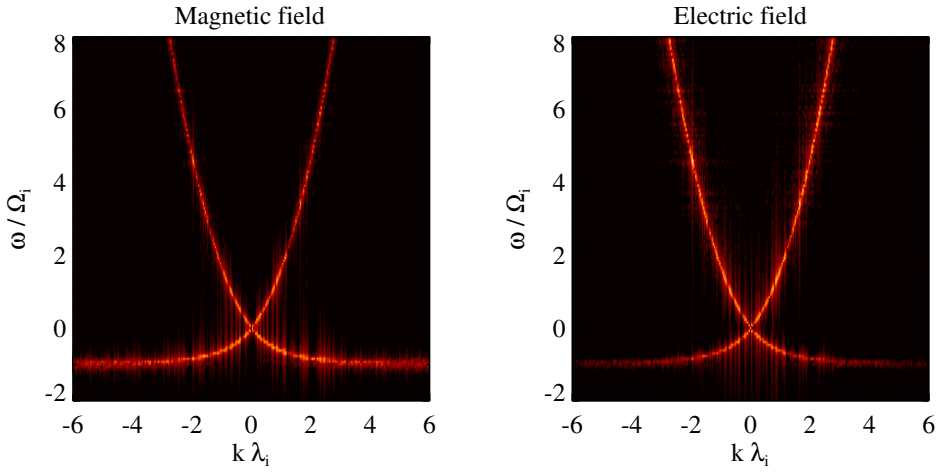

Figure C.1: Whistler and ion-cyclotron modes calculated using (left) magnetic field and (right) electric field data .

The plasma dispersion solver

Parallel propagating electromagnetic unstable modes are checked. The plasma consists of beam and main ion components, and electrons. Parameters used here are summarized in Table C.1 [28]. Figure C.2 shows the dispersions of right-handed polarized electromagnetic waves ($\omega_{\rm real}/\left|\omega_{\rm real}\right| = +1$; i.e., whistler waves). Black solid and red dashed lines respectively stand for the real and the imaginary

Table C.1: Simulation parameters for an ion/ion beam instability.

$n_{i,b}/n_e$	$T_{i,b}/T_{i,m}$	$T_e/T_{i,m}$	$T_{j,\perp}/T_{j,\parallel}$	m_i/m_e	$\beta_{i,m}$	V_A/c
0.01	10.0	1.0	1.0	1896	1.0	1.0×10^{-4}

parts of each mode. The wave mode in $k > 0$ propagates in the same direction as beam ions, while that in $k < 0$ propagates oppositely. Among the cases (A)–(D), the relative bulk velocity, v_0, between main- and beam-ion components differs. As the relative bulk velocity increases, both resonant ($k > 0$) and non-resonant ($k < 0$) instabilities can be seen as is shown by [28].

MHD part of the Reynolds-averaged model

As examples of one-dimensional test problems, a famous shock-tube problem [10] is shown for reference. The parameters are summarized in Table C.2. N_x stands for the number of grids, and the subscripts $\rho_{\rm L}$ and $\rho_{\rm R}$ respectively represent the physical quantities in $x < 0$ and $x > 0$. Free boundary conditions are assumed at $x/L_x = \pm 0.5$. The black circles and dotted lines in Figure C.3 show numerical results. Here, ε is internal energy density ($\varepsilon \equiv p/\left[\rho\left(\gamma_{\rm adi} - 1\right)\right]$). From left to right, an expansion fan, a slow compound wave, a contact discontinuity, a slow-mode shock, and a fast rarefaction wave form.

As an example of a two-dimensional test problem, the time evolution of MHD vortex are shown [69]. Boundaries are periodic in both x- and y-directions. Total number of grids are set to $N_x \times N_y = 512 \times 512$. Profiles of velocity and magnetic field are given by

$$\boldsymbol{V} = \begin{pmatrix} \sin\left(2\pi y\right) \\ -\sin\left(2\pi x\right) \\ 0 \end{pmatrix}, \quad \boldsymbol{B} = B_0 \begin{pmatrix} \sin\left(2\pi y\right) \\ \sin\left(4\pi x\right) \\ 0 \end{pmatrix}, \tag{C.24}$$

where $B_0 = (4\pi)^{-1/2}$. An adiabatic index and the plasma beta are respectively

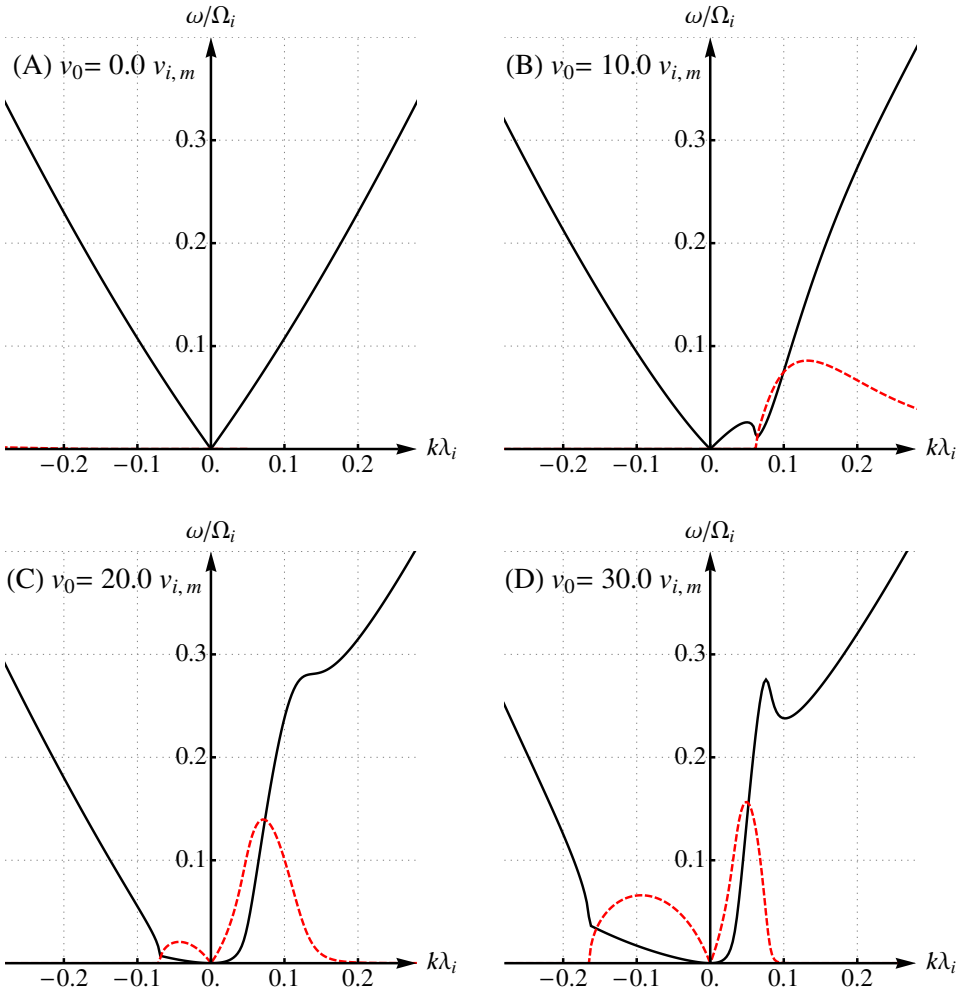

Figure C.2: Dispersion relations of right-handed polarized electromagnetic modes. Real and imaginary parts are shown by the black-solid and the red-dashed lines, respectively.

set to $\gamma_{\rm adi} = 5/3$ and $\beta_p = 2\gamma_{\rm adi}$. Additionally, the plasma pressure and density are given by $p = B_0^2\beta_p/2$ and $\rho = \gamma_{\rm adi}p$, respectively. Figure C.4 shows time evolution of the plasma density. Time is normalized by Alfvén transit time $\tau_A = L_x/V_A = 512$.

Table C.2: Simulation parameters for the shock-tube problem

N_x	$\gamma_{\rm adi}$	$\rho_{\rm L}/\rho_{\rm R}$	$p_{\rm L}/p_{\rm R}$	$\boldsymbol{V}_{\rm L}/\boldsymbol{V}_{\rm R}$	$\boldsymbol{B}_{\rm L}/\boldsymbol{B}_{\rm R}$
1024	2.0	1.0/0.125	1.0/0.1	$\boldsymbol{0}/\boldsymbol{0}$	$(0.75, 1.0/-1.0, 0.0)$

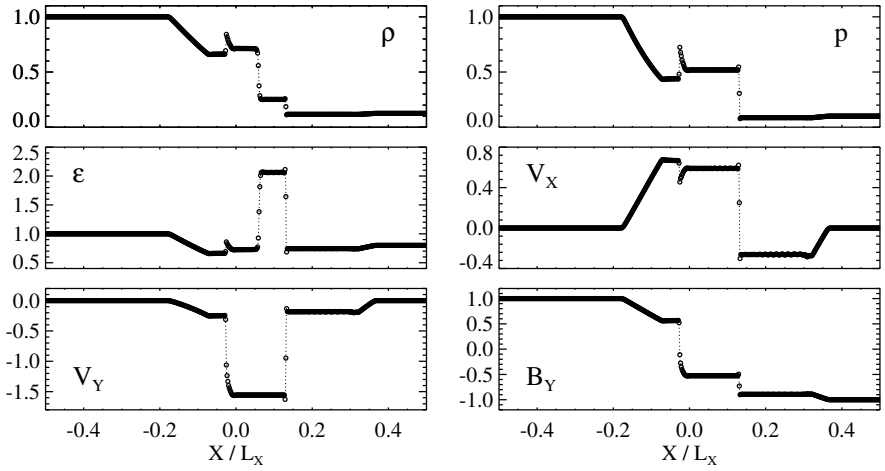

Figure C.3: Simulation results of the shock-tube problem. Both black circles and black lines stand for the numerical results.

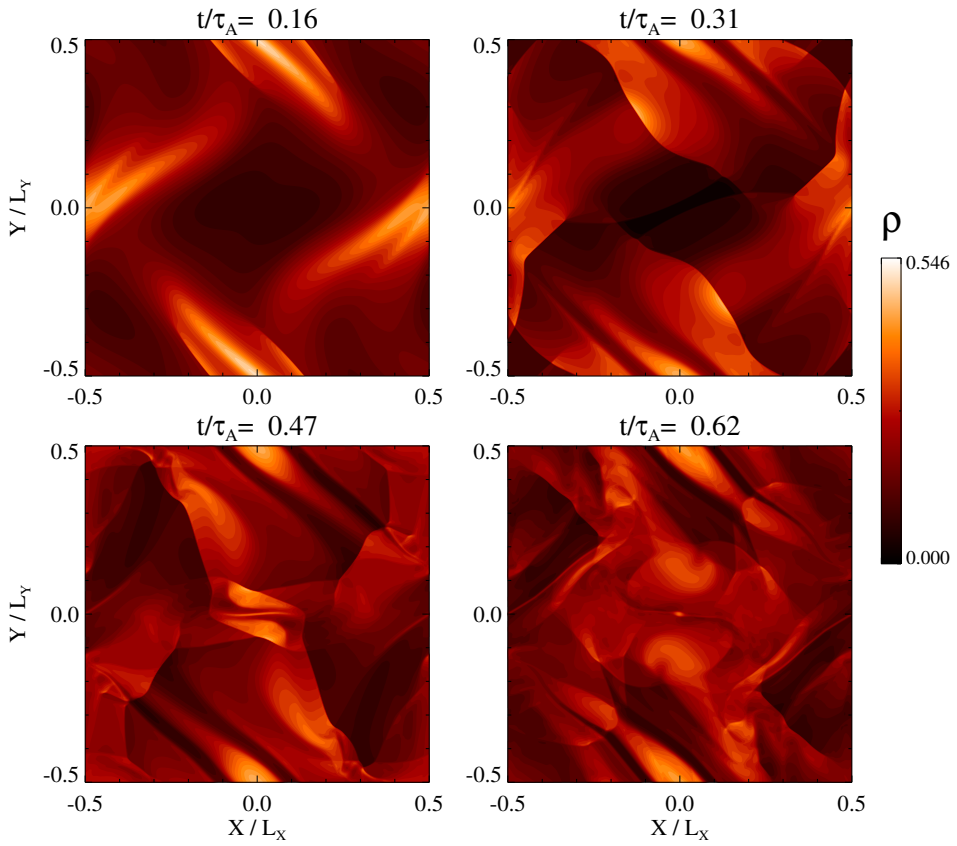

Figure C.4: Time evolution of the plasma density. These snapshots are taken at $t/\tau_A = 0.16, 0.31, 0.47$, and 0.62.

REFERENCES

[1] T. Amano, K. Higashimori, and K. Shirakawa. A robust method for handling low density regions in hybrid simulations for collisionless plasmas. *Journal of Computational Physics*, 275:197–212, October 2014.

[2] K. Arzner and M. Scholer. Kinetic structure of the post plasmoid plasma sheet during magnetotail reconnection. *J. Geophys. Res.*, 106:3827–3844, March 2001.

[3] M. Bárta, J. Büchner, M. Karlický, and J. Skála. Spontaneous Current-layer Fragmentation and Cascading Reconnection in Solar Flares. I. Model and Analysis. *The Astrophysical Journal*, 737:24, August 2011.

[4] N. Bessho and A. Bhattacharjee. Fast collisionless reconnection in electron-positron plasmas. *Physics of Plasmas*, 14(5):056503, May 2007.

[5] A. Bhattacharjee, Y.-M. Huang, H. Yang, and B. Rogers. Fast reconnection in high-Lundquist-number plasmas due to the plasmoid Instability. *Physics of Plasmas*, 16(11):112102, November 2009.

[6] W.G. Bickley. The plane jet. *Phil. Mag.*, 23:727–731, 1937.

[7] J. Birn, J. F. Drake, M. A. Shay, B. N. Rogers, R. E. Denton, M. Hesse, M. Kuznetsova, Z. W. Ma, A. Bhattacharjee, A. Otto, and P. L. Pritchett. Geospace Environmental Modeling (GEM) magnetic reconnection challenge. *J. Geophys. Res.*, 106:3715–3720, March 2001.

[8] D. Biskamp. Magnetic reconnection via current sheets. *Physics of Fluids*, 29:1520–1531, May 1986.

[9] A. Brandenburg and K. Subramanian. Astrophysical magnetic fields and non-linear dynamo theory. *Physics Reports*, 417:1–209, October 2005.

[10] M. Brio and C. C. Wu. An upwind differencing scheme for the equations of ideal magnetohydrodynamics. *Journal of Computational Physics*, 75:400–422, April 1988.

[11] J. Buechner and L. M. Zelenyi. Regular and chaotic charged particle motion in magnetotaillike field reversals. I - Basic theory of trapped motion. *J. Geophys. Res.*, 94:11821–11842, September 1989.

[12] H. Che, J. F. Drake, and M. Swisdak. A current filamentation mechanism for breaking magnetic field lines during reconnection. *Nat. Phys.*, 474:184–187, June 2011.

[13] J. Chen and P. Palmadesso. Tearing instability in an anisotropic neutral sheet. *Physics of Fluids*, 27:1198–1206, May 1984.

[14] J. Chen and P. J. Palmadesso. Chaos and nonlinear dynamics of single-particle orbits in a magnetotaillike magnetic field. *J. Geophys. Res.*, 91:1499–1508, February 1986.

[15] G. F. Chew, M. L. Goldberger, and F. E. Low. The Boltzmann Equation and the One-Fluid Hydromagnetic Equations in the Absence of Particle Collisions. *Royal Society of London Proceedings Series A*, 236:112–118, July 1956.

[16] W. Daughton, V. Roytershteyn, H. Karimabadi, L. Yin, B. J. Albright, B. Bergen, and K. J. Bowers. Role of electron physics in the development of turbulent magnetic reconnection in collisionless plasmas. *Nature Physics*, 7:539–542, July 2011.

[17] W. Daughton, V. Roytershteyn, H. Karimabadi, L. Yin, B. J. Albright, S. P. Gary, and K. J. Bowers. Secondary Island Formation in Collisional and Collisionless Kinetic Simulations of Magnetic Reconnection. In D. Vassiliadis, S. F. Fung, X. Shao, I. A. Daglis, and J. D. Huba, editors, *American Institute of Physics Conference Series*, volume 1320 of *American Institute of Physics Conference Series*, pages 144–159, January 2011.

[18] A. Dedner, F. Kemm, D. Kröner, C.-D. Munz, T. Schnitzer, and M. Wesenberg. Hyperbolic Divergence Cleaning for the MHD Equations. *Journal of Computational Physics*, 175:645–673, January 2002.

[19] J. F. Drake, M. Swisdak, C. Cattell, M. A. Shay, B. N. Rogers, and A. Zeiler. Formation of Electron Holes and Particle Energization During Magnetic Reconnection. *Science*, 299:873–877, February 2003.

[20] J. F. Drake, M. Swisdak, T. D. Phan, P. A. Cassak, M. A. Shay, S. T. Lepri, R. P. Lin, E. Quataert, and T. H. Zurbuchen. Ion heating resulting from pickup in magnetic reconnection exhausts. *J. Geophys. Res.*, 114:5111, May 2009.

[21] J. W. Dungey. Interplanetary Magnetic Field and the Auroral Zones. *Physical Review Letters*, 6:47–48, January 1961.

[22] J. P. Eastwood, T. D. Phan, S. D. Bale, and A. Tjulin. Observations of Turbulence Generated by Magnetic Reconnection. *Physical Review Letters*, 102(3):035001, January 2009.

[23] J. W. Eastwood. Consistency of fields and particle motion in the 'Speiser' model of the current sheet. *Planetary ans Space Science*, 20:1555–1568, October 1972.

[24] B. D. Fried. Mechanism for Instability of Transverse Plasma Waves. *Phys. Fluids.*, 2:337, May 1959.

[25] K. Fujimoto and R. D. Sydora. Plasmoid-Induced Turbulence in Collisionless Magnetic Reconnection. *Phys. Rev. Lett.*, 109(26):265004, December 2012.

[26] H. P. Furth, J. Killeen, and M. N. Rosenbluth. Finite-Resistivity Instabilities of a Sheet Pinch. *Physics of Fluids*, 6:459–484, April 1963.

[27] L. Gargaté, R. Bingham, R. A. Fonseca, and L. O. Silva. dHybrid: A massively parallel code for hybrid simulations of space plasmas. *Computer Physics Communications*, 176:419–425, March 2007.

[28] S. P. Gary, D. W. Foosland, C. W. Smith, M. A. Lee, and M. L. Goldstein. Electromagnetic ion beam instabilities. *Physics of Fluids*, 27:1852–1862, July 1984.

[29] S. P. Gary, J. T. Gosling, and D. W. Forslund. The electromagnetic ion beam instability upstream of the earth's bow shock. *J. Geophys. Res.*, 86:6691–6696, August 1981.

[30] S. P. Gary and D. Winske. Computer simulations of electromagnetic instabilities in the plasma sheet boundary layer. *J. Geophys. Res.*, 95:8085–8094, June 1990.

[31] R. G. Giovanelli. A Theory of Chromospheric Flares. *Nature*, 158:81–82, July 1946.

[32] P. Goldreich and S. Sridhar. Toward a theory of interstellar turbulence. 2: Strong alfvenic turbulence. *The Astrophysical Journal*, 438:763–775, January 1995.

[33] M. L. Goldstein. An instability of finite amplitude circularly polarized Alfven waves. *The Astrophysical Journal*, 219:700–704, January 1978.

[34] M. L. Goldstein, D. A. Roberts, and W. H. Matthaeus. Magnetohydrodynamic Turbulence In The Solar Wind. *Annu. Rev. Astron. Astrophys.*, 33:283–326, 1995.

[35] D. A. Gurnett, R. R. Anderson, B. T. Tsurutani, E. J. Smith, G. Paschmann, G. Haerendel, S. J. Bame, and C. T. Russell. Plasma wave turbulence at the magnetopause - Observations from ISEE 1 and 2. *J. Geophys. Res.*, 84:7043–7058, December 1979.

[36] F. Hamba. Turbulent dynamo effect and cross helicity in magnetohydrodynamic flows. *Physics of Fluids*, 4:441–450, February 1992.

[37] E. G. Harris. On a plasma sheath separating regions of oppositely directed magnetic field. *Nuovo Ciment*, 23(1):115–121, January 1962.

[38] M. Hesse, K. Schindler, J. Birn, and M. Kuznetsova. The diffusion region in collisionless magnetic reconnection. *Phys. Plasmas*, 6:1781–1795, May 1999.

[39] M. Hesse and D. Winske. Electron dissipation in collisionless magnetic reconnection. *J. Geophys. Res.*, 103:26479–26486, November 1998.

[40] K. Higashimori and M. Hoshino. The relation between ion temperature anisotropy and formation of slow shocks in collisionless magnetic reconnection. *J. Geophys. Res.*, 117:1220, January 2012.

[41] K. Higashimori, N. Yokoi, and M. Hoshino. Explosive Turbulent Magnetic Reconnection. *Phys. Rev. Lett.*, 110(25):255001, June 2013.

[42] M. Hoshino and M. L. Goldstein. Time evolution from linear to nonlinear stages in magnetohydrodynamic parametric instabilities. *Phys. Fluids B*, 1:1405–1415, July 1989.

[43] M. Hoshino, T. Mukai, I. Shinohara, Y. Saito, and S. Kokubun. Slow shock downstream structure in the magnetotail. *J. Geophys. Res.*, 105:337–348, January 2000.

[44] M. Hoshino, T. Mukai, T. Yamamoto, and S. Kokubun. Ion dynamics in magnetic reconnection: Comparison between numerical simulation and Geotail observations. *J. Geophys. Res.*, 103:4509–4530, March 1998.

[45] M. Hoshino, A. Nishida, T. Yamamoto, and S. Kokubun. Turbulent magnetic field in the distant magnetotail: Bottom-up process of plasmoid formation? *Geophys. Res. Lett.*, 21:2935–2938, December 1994.

[46] M. Hoshino, Y. Saito, T. Mukai, A. Nishida, S. Kokubun, and T. Yamamoto. Origin of hot and high speed plasmas in plasma sheet: plasma acceleration and heating due to slow shocks. *Advances in Space Research*, 20:973–982, September 1997.

[47] Y.-M. Huang and A. Bhattacharjee. Scaling laws of resistive magnetohydrodynamic reconnection in the high-Lundquist-number, plasmoid-unstable regime. *Phys. Plasmas*, 17(6):062104, June 2010.

[48] H. Ji and W. Daughton. Phase diagram for magnetic reconnection in heliophysical, astrophysical, and laboratory plasmas. *Physics of Plasmas*, 18(11):111207, November 2011.

[49] H. Ji, Y. Ren, M. Yamada, S. Dorfman, W. Daughton, and S. P. Gerhardt. New insights into dissipation in the electron layer during magnetic reconnection. *Geophys. Res. Lett.*, 35:13106, July 2008.

[50] H. Karimabadi, D. Krauss-Varban, N. Omidi, and H. X. Vu. Magnetic structure of the reconnection layer and core field generation in plasmoids. *J. Geophys. Res.*, 104:12313–12326, June 1999.

[51] G. Kowal, A. Lazarian, E. T. Vishniac, and K. Otmianowska-Mazur. Numerical Tests of Fast Reconnection in Weakly Stochastic Magnetic Fields. *The Astrophysical Journal*, 700:63–85, July 2009.

[52] R. H. Kraichnan. The structure of isotropic turbulence at very high Reynolds numbers. *Journal of Fluid Mechanics*, 5:497–543, 1959.

[53] B.E. Launder and D.B. Spalding. Lectures in Mathematical Model of Turbulence. *London, UK, Academic Press*, 1972.

[54] A. Lazarian and E. T. Vishniac. Reconnection in a Weakly Stochastic Field. *The Astrophysical Journal*, 517:700–718, June 1999.

[55] L. C. Lee, S. Wang, C. Q. Wei, and B. T. Tsurutani. Streaming sausage, kink and tearing instabilities in a current sheet with applications to the earth's magnetotail. *J. Geophys. Res.*, 93:7354–7365, July 1988.

[56] Y. Lin and D. W. Swift. A two-dimensional hybrid simulation of the magnetotail reconnection layer. *J. Geophys. Res.*, 101:19859–19870, September 1996.

[57] A. S. Lipatov. *The hybrid multiscale simulation technology: an introduction with application to astrophysical and laboratory plasmas*. 2002.

[58] Y.-H. Liu, J. F. Drake, and M. Swisdak. The structure of the magnetic reconnection exhaust boundary. *Phys. Plasmas*, 19(2):022110, February 2012.

[59] R.-F. Lottermoser, M. Scholer, and A. P. Matthews. Ion kinetic effects in magnetic reconnection: Hybrid simulations. *J. Geophys. Res.*, 103:4547–4560, March 1998.

[60] N. F. Loureiro, A. A. Schekochihin, and S. C. Cowley. Instability of current sheets and formation of plasmoid chains. *Physics of Plasmas*, 14(10):100703, October 2007.

[61] N. F. Loureiro, D. A. Uzdensky, A. A. Schekochihin, S. C. Cowley, and T. A. Yousef. Turbulent magnetic reconnection in two dimensions. *Monthly Notices of the Royal Astronomical Society*, 399:L146–L150, October 2009.

[62] A. T. Y. Lui, P. H. Yoon, and C.-L. Chang. Quasi-linear analysis of ion Weibel instability in the earth's neutral sheet. *J. Geophys. Res.*, 98:153–163, January 1993.

[63] Z. W. Ma and A. Bhattacharjee. Hall magnetohydrodynamic reconnection: The Geospace Environment Modeling challenge. *J. Geophys. Res.*, 106:3773–3782, March 2001.

[64] W. H. Matthaeus and M. L. Goldstein. Measurement of the rugged invariants of magnetohydrodynamic turbulence in the solar wind. *J. Geophys. Res.*, 87:6011–6028, August 1982.

[65] W. H. Matthaeus and S. L. Lamkin. Turbulent magnetic reconnection. *Physics of Fluids*, 29:2513–2534, August 1986.

[66] E. Moebius, M. Scholer, D. Hovestadt, G. Paschmann, and G. Gloeckler. Energetic particles in the vicinity of a possible neutral line in the plasma sheet. *J. Geophys. Res.*, 88:7742–7752, October 1983.

[67] H. K. Moffatt. Magnetic field generation in electrically conducting fluids. *Cambridge University Press*, 1978.

[68] A. Nishida, T. Yamamoto, K. Tsuruda, H. Hayakawa, A. Matsuoka, S. Kokubun, M. Nakamura, and H. Kawano. Classification of the tailward drifting magnetic structures in the distant tail. *Geophys. Res. Lett.*, 21:2947–2950, December 1994.

[69] S. A. Orszag and C.-M. Tang. Small-scale structure of two-dimensional magnetohydrodynamic turbulence. *Journal of Fluid Mechanics*, 90:129–143, January 1979.

[70] E. N. Parker. Sweet's Mechanism for Merging Magnetic Fields in Conducting Fluids. *J. Geophys. Res.*, 62:509–520, December 1957.

[71] E. N. Parker. The Solar-Flare Phenomenon and the Theory of Reconnection and Annihiliation of Magnetic Fields. *The Astrophysical Journal Supplement*, 8:177, July 1963.

[72] H. E. Petschek. Magnetic Field Annihilation. *NASA Special Publication*, 50:425, 1964.

[73] K. B. Quest. Theory and simulation of collisionless parallel shocks. *J. Geophys. Res.*, 93:9649–9680, September 1988.

[74] M. Rempel, M. Schüssler, and M. Knölker. Radiative Magnetohydrodynamic Simulation of Sunspot Structure. *The Astrophysical Journal*, 691:640–649, January 2009.

[75] F. Sahraoui, M. L. Goldstein, P. Robert, and Y. V. Khotyaintsev. Evidence of a Cascade and Dissipation of Solar-Wind Turbulence at the Electron Gyroscale. *Physical Review Letters*, 102(23):231102, June 2009.

[76] Y. Saito, T. Mukai, T. Terasawa, A. Nishida, S. Machida, M. Hirahara, K. Maezawa, S. Kokubun, and T. Yamamoto. Slow-mode shocks in the magnetotail. *J. Geophys. Res.*, 100:23567–23582, December 1995.

[77] T. Sato and T. Hayashi. Externally driven magnetic reconnection and a powerful magnetic energy converter. *Physics of Fluids*, 22:1189–1202, June 1979.

[78] T. Sato and R. J. Walker. Magnetotail dynamics excited by the streaming tearing mode. *J. Geophys. Res.*, 87:7453–7459, September 1982.

[79] M. Scholer and K. Arzner. Hybrid Simulations of Magnetotail Reconnection: Turbulence in the Post Plasmoid Plasma Sheet. In B. Warmbein, editor, *Sheffield Space Plasma Meeting: Multipoint Measurements versus Theory*, volume 492 of *ESA Special Publication*, page 93, January 2001.

[80] M. A. Shay and J. F. Drake. The role of electron dissipation on the rate of collisionless magnetic reconnection. *Geophys. Res. Lett.*, 25:3759–3762, 1998.

[81] M. A. Shay, J. F. Drake, B. N. Rogers, and R. E. Denton. The scaling of collisionless, magnetic reconnection for large systems. *Geophys. Res. Lett.*, 26:2163–2166, 1999.

[82] K. Shibata and S. Tanuma. Plasmoid-induced-reconnection and fractal reconnection. *Earth, Planets, and Space*, 53:473–482, June 2001.

[83] M. Shigeta, T. Sato, and B. Dasgupta. Streaming tearing mode. *Journal of the Physical Society of Japan*, 54:3342–3346, September 1985.

[84] I. Shinohara, H. Suzuki, M. Fujimoto, and M. Hoshino. Rapid Large-Scale Magnetic-Field Dissipation in a Collisionless Current Sheet via Coupling between Kelvin-Helmholtz and Lower-Hybrid Drift Instabilities. *Phys. Rev. Lett.*, 87(9):095001, August 2001.

[85] T. W. Speiser. Particle Trajectories in Model Current Sheets, 1, Analytical Solutions. *J. Geophys. Res.*, 70:4219–4226, September 1965.

[86] S. Sridhar and P. Goldreich. Toward a theory of interstellar turbulence. 1: Weak Alfvenic turbulence. *The Astrophysical Journal*, 432:612–621, September 1994.

[87] P. A. Sweet. The Neutral Point Theory of Solar Flares. In B. Lehnert, editor, *Electromagnetic Phenomena in Cosmical Physics*, volume 6 of *IAU Symposium*, page 123, 1958.

[88] M. Swisdak, Y.-H. Liu, and J. F. Drake. Development of a Turbulent Outflow During Electron-Positron Magnetic Reconnection. *The Astrophysical Journal*, 680:999–1008, June 2008.

[89] T. Terasawa. Hall current effect on tearing mode instability. *Geophys. Res. Lett.*, 10:475–478, June 1983.

[90] M. Ugai. Computer studies on development of the fast reconnection mechanism for different resistivity models. *Physics of Fluids B*, 4:2953–2963, September 1992.

[91] M. Ugai and T. Tsuda. Magnetic field-line reconnexion by localized enhancement of resistivity. I - Evolution in a compressible MHD fluid. *Journal of Plasma Physics*, 17:337–356, June 1977.

[92] D. A. Uzdensky and R. M. Kulsrud. Two-dimensional numerical simulation of the resistive reconnection layer. *Physics of Plasmas*, 7:4018–4030, October 2000.

[93] D. A. Uzdensky, N. F. Loureiro, and A. A. Schekochihin. Fast Magnetic Reconnection in the Plasmoid-Dominated Regime. *Physical Review Letters*, 105(23):235002, December 2010.

[94] V. M. Vasyliunas. Theoretical models of magnetic field line merging. I. *Rev. Geophys. & Spacephys.*, 13:303–336, February 1975.

[95] A. Vögler, S. Shelyag, M. Schüssler, F. Cattaneo, T. Emonet, and T. Linde. Simulations of magneto-convection in the solar photosphere. Equations, methods, and results of the MURaM code. *Astronomy & Astrophysics*, 429:335–351, January 2005.

[96] T. Watanabe. Efficient Computation of the Plasma Dispersion Function $\mathcal{Z}(\zeta)$. 核融合研究, 第 *65* 巻第 *5* 号, pages 556–580, May 1991.

[97] E. S. Weibel. Spontaneously Growing Transverse Waves in a Plasma Due to an Anisotropic Velocity Distribution. *Phys. Rev. Lett.*, 2:83–84, February 1959.

[98] D. Winske and M. M. Leroy. Diffuse ions produced by electromagnetic ion beam instabilities. *J. Geophys. Res.*, 89:2673–2688, May 1984.

[99] N. Yokoi. Modeling the turbulent cross-helicity evolution: production, dissipation, and transport rates. *Journal of Turbulence*, 12:27, January 2011.

[100] N. Yokoi. Cross helicity and related dynamo. *Geophysical and Astrophysical Fluid Dynamics*, 107:114–184, February 2013.

[101] N. Yokoi and M. Hoshino. Flow-turbulence interaction in magnetic reconnection. *Physics of Plasmas*, 18(11):111208, November 2011.

[102] N. Yokoi, R. Rubinstein, A. Yoshizawa, and F. Hamba. A turbulence model for magnetohydrodynamic plasmas. *Journal of Turbulence*, 9:37, 2008.

[103] T. Yokoyama, K. Akita, T. Morimoto, K. Inoue, and J. Newmark. Clear Evidence of Reconnection Inflow of a Solar Flare. *The Astrophysical Journal Letters*, 546:L69–L72, January 2001.

[104] A. Yoshizawa. Statistical analysis of the deviation of the Reynolds stress from its eddy-viscosity representation. *Physics of Fluids*, 27:1377–1387, June 1984.

[105] A. Yoshizawa. Self-consistent turbulent dynamo modeling of reversed field

pinches and planetary magnetic fields. *Physics of Fluids B*, 2:1589–1600, July 1990.

[106] A. Yoshizawa. Turbulent Magnetohydrodynamic Dynamo: Modeling of the Turbulent Residual-Helicity Equation. *Journal of the Physical Society of Japan*, 65:124, January 1996.

[107] A. Yoshizawa. *Hydrodynamic and Magnetohydrodynamic Turbulent Flows,* Kluwer academic publishers, ISBN: 0792352254. 1998.

[108] A. Yoshizawa and N. Yokoi. Turbulent magnetohydrodynamic dynamo for accretion disks using the cross-helicity effect. *The Astrophysical Journal*, 407:540–548, April 1993.

[109] S. Zenitani and M. Hesse. The role of the Weibel instability at the reconnection jet front in relativistic pair plasma reconnection. *Phys. Plasmas*, 15(2):022101, February 2008.

[110] S. Zenitani, I. Shinohara, and T. Nagai. Evidence for the dissipation region in magnetotail reconnection. *Geophys. Res. Lett.*, 39:11102, June 2012.

[111] G. Zimbardo, A. Greco, L. Sorriso-Valvo, S. Perri, Z. Vörös, G. Aburjania, K. Chargazia, and O. Alexandrova. Magnetic Turbulence in the Geospace Environment. *Space Science Review*, 156:89–134, October 2010.